ARRAYS OF QUANTUM-LIGHT-EMITTING DIODES WITH SITE-CONTROLLED PYRAMIDAL QUANTUM DOTS

BY

TUNG-HSUN CHUNG

A THESIS SUBMITTED TO

THE NATIONAL UNIVERSITY OF IRELAND, CORK

FOR THE DEGREE OF

DOCTOR PHILOSOPHY

EPITAXY AND PHYSICS OF NANOSTRUCTURES GROUP
TYNDALL NATIONAL INSTITUTE, DEPARTMENT OF PHYSICS
NATIONAL UNIVERSITY OF IRELAND, CORK
IRELAND

ucc

Coláiste na hOllscoile Corcaigh, Éire
University College Cork, Ireland

SEPTEMBER 2016
RESEARCH SUPERVISOR: Dr. EMANUELE PELUCCHI
HEAD OF THE DEPARTMENT: PROF. JOHN McINERNEY

Table of Content

Declaration

This dissertation is the result of work carried out in the Epitaxy and Physics of Nanostructures Group at Tyndall National Institute from April 2012 to August 2016.

Except where otherwise stated this dissertation is the result of my own work and is not substantially the same as any I have already submitted, or that I am in the process of submitting, for any degree either at University College Cork or elsewhere.

Tung-Hsun Chung,
Tyndall National Institute,
University College of Cork,
April 2017.

Acknowledgement

In pretty much five years ago, I have joined the group of Epitaxy and Physics of Nanostructures in Tyndall National Institute, supervised by Dr. Emanuele Pelucchi. At the end of my Ph.D. journey, I would like to express my sincerest gratitude to him for his unparalleled passion as a supervisor and perseverant pursuit of science as a scientist. In addition, this thesis cannot be completed without his profession in establishing the wonderful research environment.

Based on the complete review system in Tyndall, I was able to finish the thesis smoothly. To this end, I would like to thank the monitor of my thesis, Prof. Eoin O'Reilly, for the constructive advices. Meanwhile, I appreciate Prof. James Greer and Prof. Sven Höfling, as the examiner for this work, for the invaluable opinions on the revision of my thesis.

Along my Ph.D. journey, I thank Dr. Valeria Dimastrodonato for guiding my how to start a research in every aspect. For the epitaxy, Dr. Aganieszka Gocalinska and Dr. Kevin Thomas have offered a plenty help. For the optical characterization and device fabrication, a fruitful experience has been obtained as working to Dr. Gediminas Juska and our super Ph.D. student, Mr. Stefano Moroni. As for the device modeling, Dr. Andrea Pescaglini has supported me firmly. Special appreciation is addressed to all other group members, Enrica Mura and Dr. Marina Manganaro for the experience sharing.

A great part of my study was placed in device fabrication. It is going to be time-consuming and painstaking if without discussion with related experts. For this reason, I would like to thank Dr. James O'Callaghan, Mr. Dan O'Connell, Dr. Hua Yang, Mr. Marc Rensing, Mr. Minqi Yang, and Mr. Krimo Khalfi for the powerful help.

What I have obtained from studying Ireland is not only the well training in research but also the experience of life in multi-culture environment. Thanks to all the people I have known during these years.

Moreover, I, for sure, would like to appreciate my parents the most for their unyielding support without leaving pressure on me along my Ph.D. journey. Without their trust, I cannot even start to dream of what I have earned now. This thesis is dedicated to you.

The financial support for my study in these years was provided by Science Foundation Ireland under the grant, 10/IN.1/I3000.

Publications

Journal papers:

1. T. H. Chung, G. Juska, S. T. Moroni, A. Pescaglini, A. Gocalinska, and E. Pelucchi, *Engineering of selective carrier injection in patterned arrays of single-quantum-dot entangled photon light-emitting diodes*, Nat. Photon., 10 (2016) 782.
2. G. Juska, V. Dimastrodonato, L. O. Mereni, T. H. Chung, A. Gocalinska, E. Pelucchi, B. Van Hattem, M. Ediger, and P. Corfdir, *Complex optical signatures from quantum dot nanostructures and behavior in inverted pyramidal recesses*, Phys. Rev. B, 89 (2014) 205430.
3. G. Juska, E. Murray V. Dimastrodonato, T. H. Chung, S. T. Moroni, A. Gocalinska, and E. Pelucchi, *Conditions for entangled photon emission from (111)B site-controlled pyramidal quantum dots*, J. Appl. Phys., 117 (2015) 134302.
4. S. T. Moroni, V. Dimastrodonato, T.H. Chung, G. Juska, A. Gocalinska, D. D. Vvedensky, and E Pelucchi, *Indium segregation during III–V quantum wire and quantum dot formation on patterned Substrates*, Journal of Applied Physics 117 (2015) 164313.
5. T. H. Chung, G. Juska, S. T. Moroni, A. Pescaglini, A. Gocalinska, and E. Pelucchi, *Single photon emission from arrays of electrically injected single dot emitters*, to be submitted.
6. S. T. Moroni, T.H. Chung, G. Juska, A. Gocalinska, and E Pelucchi, *Site-controlled stacked pyramidal quantum dots and their properties*, to be submitted.

Conference papers:

Oral presentations as main author

1. T-H Chung, G. Juska, S. T. Moroni, A. Gocalinska, and E. Pelucchi, *Towards electrically-driven non-classical light emitter with site-controlled pyramidal quantum dots*, QD Day 2015, Cambridge, UK, Jan. 12th, 2015.
2. T-H Chung, G. Juska, S. T. Moroni, A. Gocalinska, A. Pescaglini, E. Pelucchi, *On-demand electrically-driven semiconductor quantum light sources*, Photonics Ireland 2015, Cork, Ireland, Sep. 2nd, 2015.
3. T-H Chung, G. Juska, S. T. Moroni, A. Gocalinska, A. Pescaglini, E. Pelucchi, *Array of entangled-light-emitting diodes with site-controlled pyramidal quantum dots*, Compound Semiconductor Week 2016, Toyama, Japan, Jun. 26th, 2016.

Oral presentations as co-author

1. G. Juska, V. Dimastrodonato, L. O. Mereni, T-H Chung, A. Gocalinska and E. Pelucchi, "*Polarization entangled photon emission from site controlled pyramidal quantum dots*" IOP One Day QD meeting, Nottingham University (UK), 10th of January 2013.

2. Gediminas Juska, Valeria Dimastrodonato, Tung-Hsun Chung, Agnieszka Gocalinska, Emanuele Pelucchi, "*Polarization-Entangled Photons from Site Controlled Pyramidal Quantum Dots*", CLEO 2013, Conference on Lasers and Electro-Optics 2013, San Jose Convention Center, 9-14 June 2013, San Jose, CA, USA.

3. V. Dimastrodonato, G. Juska, T. H. Chung, P. A. Zestanakis, D. D. Vvedensky, and E. Pelucchi. "*Growth transients of pyramidal quantum dots for quantum optics applications*", 8th International Conference on Quantum Dots, 11-15 May 2014, Pisa, Italy.

4. G. Juska, V. Dimastrodonato, L. O. Mereni, T. H. Chung, A. Gocalinska, and E. Pelucchi, B. Van Hattem, P. Corfdir, M. Ediger, and R. T. Phillips, "*Unexpected simultaneous formation of two types of site-controlled quantum dots in pyramidal recesses*", 8th International Conference on Quantum Dots, 11-15 May 2014, Pisa, Italy.

5. G. Juska, V. Dimastrodonato, T. H. Chung, A. Gocalinska, E. Pelucchi, "*Entangled-photon emission from site-controlled quantum dots grown by MOVPE*", 17th International Conference on Metalorganic Vapor Phase Epitaxy, Lausanne, Switzerland, 13th – 18th July 2014.

6. V. Dimastrodonato, G. Juska ,T. H. Chung , P. A. Zestanakis, D. D. Vvedensky, and E.Pelucchi (presenting author), "*Modeling patterned substrate growth by MOVPE: from equilibrium to transient dynamics*", 10th International Workshop on Epitaxial Semiconductors on Patterned Substrates and Novel Index Surfaces, Traunkirchen, Austria, July 20 - 23, 2014.

7. G. Juska, T-H. Chung, A. Gocalinska, S. Moroni, E. Pelucchi, "*Towards Tunable, Electrically Driven Source of Non-Classical Light Based on Site-Controlled Pyramidal Quantum Dots*" Compound Semiconductor Week 2015, June 29-July 2nd 2015, Santa Barbara, California, USA.

8. G. Juska, T. H. Chung, A. Gocalinska, S. Moroni, E. Pelucchi, "*Light-Emitting Diodes of Non-Classical Light Based on Site-Controlled Pyramidal Quantum Dots*", CLEO Europe -EQEC 2015, Munich, ICM Congress Centre, Germany, 21 - 25 June 2015

9. Gediminas Juska, Tung-Hsun Chung, Stefano T. Moroni, Agnieszka Gocalinska, Emanuele Pelucchi, "*A Site-Controlled Quantum Dot Light-Emitting Diode of*

Polarization-Entangled Photons, Violating Bell's Inequality", CLEO (Conference on Lasers and Electro-Optics) 2016, 5-10 June, 2017, San Jose, California, USA.

10. Stefano T. Moroni, Valeria Dimastrodonato , Tung-Hsun Chung , Gediminas Juska , Agnieszka Gocalinska , Dimitri Vvedensky and Emanuele Pelucchi, "*Modelling InGaAs Metalorganic Vapour-Phase Epitaxy: V-Grooved Quantum Wires and Pyramidal Quantum Dots Formation*" 18th International Conference on Metal Organic Vapor Phase Epitaxy, July 10-15, 2016, Sheraton San Diego Hotel & Marina San Diego, California, USA.

Invited presentations as co-author

1. E. Pelucchi, G. Juska, V. Dimastrodonato, T. H. Chung, A. Gocalinska, "Site-controlled QDs: a route for dense arrays of integrated entangled photon emitters", IEEE Summer Topicals 2013, Quantum Communications & Photonics, 8 - 10 July 2013, Hilton Waikoloa, Big Island of Hawaii, USA.
2. E. Pelucchi, G. Juska, V. Dimastrodonato, T. H. Chung, and A. Gocalinska, "Engineering entangled photon emission from site-controlled quantum dots", Photon14, Imperial College London, 01-04 September 2014, London, UK.
3. E. Pelucchi, G. Juska, T. H. Chung, E. Murray, A. Gocalinska "Entangling photons from site-controlled quantum dots: accomplishments and open challenges", 24th IEEE International Semiconductor Laser Conference (ISLC 2014), 7 - 10 September 2014, Meliá Palas Atenea, Palma de Mallorca, Spain.
4. E. Pelucchi, G. Juska, E. Murray, V. Dimastrodonato, T. H. Chung , A. Gocalinska, "A short "how to" for entangled photon emission from Pyramidal quantum dots", 2nd International Workshop on Engineering of Quantum Emitter Properties, EQL2014, Innsbruck University, Innsbruck, Austria, 4-5 December 2014.
5. E. Pelucchi, G. Juska, V. Dimastrodonato, T. H. Chung, S. T. Moroni, A. Pescaglini, E. Mura and A. Gocalinska, "Site-controlled and self-assembled QDs: how to do it differently…(not to say better)", SemiconNano 2015 Lakeshore Hotel, Hsinchu, Taiwan, 2015/9/6~9/11.
6. S. T. Moroni (presenting author), T. H. Chung, G. Juska, A. Pescaglini, A. Gocalinska and E. Pelucchi (invited talk), "Exploring new potentials with pyramidal quantum dots: electrical control and coupling of quantum dots", 3rd International Workshop on "Engineering of Quantum Emitter Properties, Johannes Kepler University Linz, 17-18 December 2015
7. G. Juska, V. Dimastrodonato, T. H. Chung, A. Gocalinska and E. Pelucchi, "Pyramidal quantum dots: site-controlled entangled photon sources", 1st International Workshop on Engineering of Quantum Dot Emission Properties (EQD 2013), Linz, 9-10 December 2013, Austria

Invited presentations as co-author

1. E. Pelucchi, G. Juska, E. Murray, V. Dimastrodonato, T. H. Chung, S.T. Moroni, A. Pescaglini, E. Mura and A. Gocalinska "Site-controlled and self-assembled quantum dots", Lancaster University, Physics, Friday 01 May 2015, UK.
2. E. Pelucchi, G. Juska, E. Murray, V. Dimastrodonato, T. H. Chung, S.T. Moroni, A. Pescaglini, E. Mura and A. Gocalinska "New devices and capabilities with site-controlled and self-assembled QDs", Eindhoven University of Technology, Department of Applied Physics, 07/05/2015, Netherlands.
3. E. Pelucchi, T. H. Chung, G. Juska, V. Dimastrodonato, S. T. Moroni, A. Pescaglini, E. Mura and A. Gocalinska "Site- and not-site controlled QDs at the EPN group, novelty and directions", Research Center of Applied Science, Academia Sinica, Taipei, Taiwan

Poster presentations as main author

1. T-H Chung, V. Dimastrodonato, G. Juska, A. Gocalinska, and E. Pelucchi, *Improving back-etching techniques for pyramidal quantum dots*, Photonics Ireland 2013, Belfast, UK, Sep. 4th, 2013.

2. T-H Chung, V. Dimastrodonato, G. Juska, A. Gocalinska, and E. Pelucchi, *Pyramidal quantum dots: open problems and routes to entangled photon devices*, 18th International Winterschool on New Developments in Solid State Physics, Mauterndorf, Austria, Feb. 23rd, 2014.

3. T-H Chung, G. Juska, S. T. Moroni, A. Gocalinska, A. Pescaglini, E. Pelucchi, *Electrically-pumped/tuned Site-controlled Pyramidal Quantum Dots*, 16th European Workshop on Metalorganic Vapour Phase Epitaxy (EWMOVPE XVI), Lund Sweden, Jun. 7th, 2015.

4. T-H Chung, G. Juska, S. T. Moroni, A. Gocalinska, A. Pescaglini, E. Pelucchi, *Site-controlled quantum dot light-emitting diode*, SemiconNano 2015, Hsinchu, Taiwan, Sep. 6th, 2015.

5. T-H Chung, G. Juska, S. T. Moroni, A. Gocalinska, A. Pescaglini, E. Pelucchi, *Bell inequalities violation with Site-controlled Pyramidal Quantum Dot LEDs Prepared by MOVPE*, 18th International Conference on Metal Organic Vapor Phase Epitaxy, San Diego, USA, Jul. 10th, 2016.

Poster presentations as co-author

1. S. T. Moroni, V. Dimastrodonato, T-H. Chung, G.Juska, A. Gocalinska, D. D. Vvedensky, and E. Pelucchi, "*Modeling InGaas growth during III-V quantum wire and*

quantum dot formation on patterned substrates", EWMOVPE 2015, June 7-10 2015,Lund, Sweden.

2. G. Juska, V. Dimastrodonato, T-H Chung, A. Gocalinska, and E. Pelucchi, "*Entangled photon emission from pyramidal site-controlled quantum dots*", 8th International Conference on Quantum Dots, 11-15 May 2014, Pisa, Italy.
3. G. Juska, V. Dimastrodonato, T-H Chung, A. Gocalinska and E. Pelucchi, "*Polarization-entangled photon sources based on pyramidal site-controlled quantum dots*", Photonics Ireland 2013, Belfast, 4-6 September 2013, Ireland
4. G. Juska, T-H Chung, S. Moroni, A. Gocalinska, and E. Pelucchi, "*Engineering properties of zero-dimensional nanostructures – pyramidal quantum dots*", Photonics Ireland 2015 Cork, 2-4 September 2015.
5. Stefano T. Moroni, Valeria Dimastrodonato, Tung-Hsun Chung, Gediminas Juska, Dimitri Vvedensky and Emanuele Pelucchi, "*Modelling InGaAs MOVPE: v-grooved quantum wires and pyramidal quantum dots*" Photonics Ireland 2015 Cork, 2-4 September 2015.
6. Stefano Moroni, Valeria Dimastrodonato, Tung-Hsun Chung, Gediminas Juska, Agnieszka Gocalinska, Dimitri Vvedensky, and Emanuele Pelucchi, "*Modeling InGaAs MOVPE in v-grooves and pyramidal recesses* "Compound Semiconductor Week 2016, June 26-30, 2016, Toyama International Conference Center, Toyama, Japan.

To my parents and you.

Abstract

Quantum information technology is an interdisciplinary subject, merging quantum mechanics and information science. In this field, the building blocks are quantum bits (qubits), which are superposition quantum states of simple two-level systems. Among all the platforms for the preparation of qubits, the polarization directions of single-photons are attractive as information carriers for practical realizations, due to reduced photon decoherence as well as the fact that they can be manipulated by convenient optical components. Moreover, the request for entangled sources from quantum communication and quantum computation can be satisfied by polarization-entangled photon emitters.

In combination of their atomic-like energy structure and mature development in foundries/labs, epitaxial semiconductor quantum dots (QDs) have been exploited to deliver quantum light sources, such as indistinguishable single-photons and polarization-entangled photon pairs, by both optical and electrical injection (with triggering on demand). However, conventional self-assembled QDs nucleate randomly and possess finite values of fine-structure splitting (FSS) in the excitonic states, mainly due to low crystal symmetry, which adds hurdles to entanglement reconstruction and significantly limits their scalability and potential for further integration.

In this thesis, pyramidal QDs (PQDs) were grown by metalorganic vapor phase epitaxy (MOVPE), starting from site- controlled pyramidal recesses photolithography-defined on GaAs (111)B substrates. Their inherent properties enable them to be controlled spatially and provide them with high crystal symmetry, i.e., close-to zero FSS, suggesting an alternative for the solution of the abovementioned difficulties encountered by self-assembled QDs. However, the non-planar feature of PQDs makes it challenging to embed them into light-emitting diodes (LEDs). Here, we developed and designed a fabrication process which successfully overcame the configuration-induced processing complexity for the preparation of on demand single-photon and entangled-photon sources by electrical injection.

Indeed, the main achievement in this thesis is the fabrication of quantum LEDs with site-controlled PQDs which are able to generate single-photons and polarization-entangled photon pairs triggered on demand. In single-photon emission, the value of $g^{(2)}(0)$ could be reduced to 0.078 ± 0.066 when combined with a time-gating technique under pulse exciation. On the other hand, the fidelities to the expected maximally polarization-entangled state were 0.85 ± 0.04 under continuous excitation and 0.823 ± 0.019 under pulse excitation by assistance of time-gating, with 75 % of the intensity maintained in a 1.5 ns window. The prepared entangled source was also importantly proved to violate Bell's inequalities.

Moreover we worked around finding solutions to some challenging issues concerning PQDs. The system in this study was an $In_{0.25}Ga_{0.75}As$ QD sandwiched by GaAs barriers. One issue in our MOVPE-grown PQDs is a dominant negatively-charged environment. We explored a number of methods as detailed in the text which proved effective in suppressing at specific conditions the probability of capturing excess electrons, strongly improving the polarization-entangled photon pair emission via the biexciton-exciton decay process, and improving our sources.

Also, a previous growth model on the AlGaAs/GaAs system developed in our group was expanded to the current system to understand the mechanism of indium segregation on both InGaAs V-grooved quantum wires and PQDs. The simulation successfully suggested consistent growth temperature-dependent emission energy evolution with the reported experimental results, in which an unexpected QD redshifting paired by a lateral quantum wires blueshifting with increasing growth temperature was observed. In addition, a new faceting at the pyramidal recess base during MOVPE growth was observed and reported for the first time.

Altogether our results justify the PQD system as a promising platform to generate quantum light sources meeting a number of important requirements: e.g. spatial control, high fidelity, trigger on demand, and electrical injection.

Chapter 1:

Introduction

1.1 General framework

In photon statistics, light sources can be classified into three categories: Poissonian light (such as a laser), super-Poissonian light (e.g., thermal light sources), and sub-Poissonian light. Only the first two groups of light can be described by classical electromagnetic theory, classified as *classical light sources*, while sub-Poissonian light is known as *quantum light* [1,2]. Briefly, quantum light sources include single-photons, where the generated photons come out one at a time at "defined" intervals, and entangled photons, produced in pairs and showing quantum correlations (we are here neglecting higher order entanglements). It is well known that quantum mechanics predicts some counterintuitive phenomena seen only in such light sources, which are exemplified hereafter.

If one directs two light beams into a 50:50 beamsplitter orthogonally, depicted as Fig. 1.1.1, the anticipated intensities from detector 1 and 2 are equivalent within the classical picture. However, once the incident lights are two single-photons and *indistinguishable* between one another, it turns out both photons will exit and be detected by one of the two detectors. This behavior is the so-called photon coalescence, resulting from the fact that photons are bosons [3]. It also creates measurement-induced entanglement.

In quantum entanglement, the description for the quantum states of the interacting particles (or quasi-particles), photons in this case, cannot be treated independently [4]. Given this, it indicates that if one particle is measured, the outcome for the other is "fully" determined *simultaneously*, some suggesting that this implies not only a nonlocal "communication" between particles but even superluminal events. Such bizarre phenomenon triggered a longstanding debate, going back to N. Bohr and A. Einstein, over the completeness of quantum mechanics in the early 20th century [5,6]. The dispute mainly circled for many years around the existence of "local hidden variables" with the generation of the entangled particles. Importantly, in 1964, J. S. Bell gave a thought experiment to

settle this argument, in which the famous Bell's inequality was derived, which showed that quantum mechanics cannot be described by a classical hidden variables local theory [7]. The violation of Bell's inequality was first experimentally demonstrated by J. F. Clauser et al. [8,9], which somehow means the Einstein's so-called "spooky action at a distance" does indeed exist. However, the derivation of a fully loophole-free Bell test (i.e. a test of Bell's inequalities not subject to "special conditions" allowing somehow classical violations) is still matter of research and debate [10,121-123].

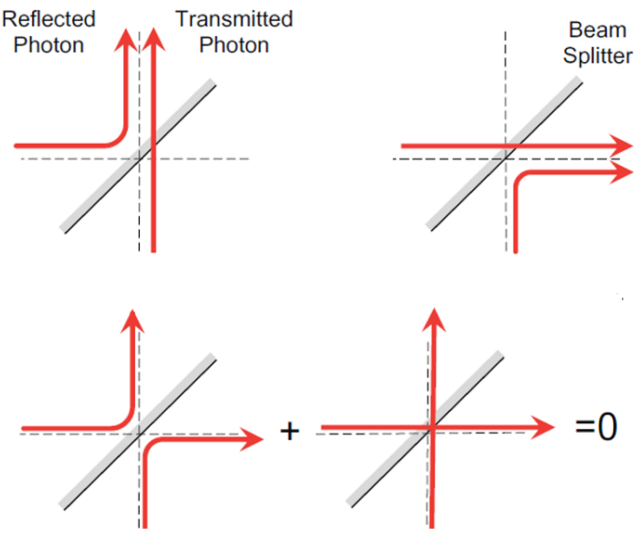

Fig. 1.1: Schematic of photon coalescence [3]. When two indistinguishable single-photons are directed into a 50:50 beam splitter, the outcome of two photons will be detected in pair on the top or right path (a). No signal will be detected if two single-photons following the paths in the (b) due to the destructive interference.

1.2 Applications in quantum information processing

Since photons are naturally "immune" to decoherence, i.e. are expected to have little dissipation over long distance propagation, quantum light sources are promising for photonic quantum information processing [2,11,12], such as quantum computation [13-16] or quantum communication [17-20], and other fields, such as quantum imaging [117].

In quantum information technology, the building blocks are quantum bits (qubits), which present a superposition state of "0" and "1" (at the same time), see Eq. 1.1, instead of only either "0" or "1" at a time like classical bits,

$$|\boldsymbol{\psi}\rangle = \boldsymbol{\alpha}|\mathbf{0}\rangle + \boldsymbol{\beta}|\mathbf{1}\rangle,, \tag{1.1}$$

where coefficients α and β are such that $\boldsymbol{\alpha^2 + \beta^2 = 1}$. Starting from quantum light sources, such a simple two-level system can be achieved, for example, by exploiting the polarization direction of single-photons, in which "0" stands for the horizontal direction $|\boldsymbol{H}\rangle$ while "1" can be labeled as vertical polarization $|\boldsymbol{V}\rangle$.

Since photons are relatively easy to manipulate, combining with some handy components, such as beam-splitters or phase-shifters, as well as single-photon sources and single-photon detectors, E. Knill et al., have proposed a scheme to realize universal quantum computation with basically only linear optics (LOQC) [14]. Given the superposition nature of qubits, quantum computation has a powerful computation capability. For instance, Shor's algorithm can drastically reduce the time required to factorize an integer, turning the classical exponentially growing time-consumption/computational complexity to a polynomial one with growing integer size [21]. Another computational demand, data-searching, was addressed by Grover's pioneering theorem [22]. Both of these two examples indicate the power of quantum computation in an era of big-data.

What Shor's theorem brought is not only a strong potential computing power but also a potential risk to RSA cryptosystems, which are mostly used to distribute private cryptographic keys, for example between clients and banks during on-line trading. To prevent this "catastrophe" before the post-quantum-computer era, ultimately secure quantum key distribution within quantum cryptography has been studied. Among those, studies include the BB84 protocol [17], based on single-photon sources, and the E91 protocol [18], relying on entangled photon sources. However, in long-haul communication, especially at the global scale, the transmission of quantum light sources suffers from losses in the passive network and decoherence process due to environment, which deteriorate with channel length exponentially. In classical communication, this will be resolved, between

two signal terminals by amplifying the optical signal, thereby compensating the losses. However, this is forbidden with fundamental quantum particles, see e.g. the no-cloning theorem in quantum communication [23]. This has brought by the idea, for example, of quantum repeaters [24,25], whose basic implementation is shown in Fig. 1.2.1 (a). In the scheme, quantum nodes are not implemented as in the classical case, but, they are designed to "teleport" quantum states between two nodes instead of simply "amplifying". The notion of "teleporting" is so-called as in quantum "teleportation" [26,27,28], see Fig. 1.2.1 (b). In which, EPR (named after A. Einstein, B. Podolsky, and N. Rosen) pairs, i.e. pairs of entangled photons, will be sent to the sender, Alice, photon 1, and to the receiver, Bob, photon 2. Alice will do a Bell-state measurement (BSM) between a quantum state $|\phi\rangle$ and photon 1, then the outcome will be sent to Bob via a classical channel, either fiber or free space. Finally the quantum state can be teleported after Bob is conducting the appropriate BSM or manipulation between the received information and photon 2. Along the timeline, once Alice has done the BSM the initial quantum state is "destroyed" but it is reconstructed at Bob's side. It is worth noting that what quantum teleportation can "transmit" is merely the quantum state information, no "bulk matter" science fiction here.

A quantum network [29] can be built if the required quantum light sources satisfy certain criteria as discussed in the next section.

Fig. 1.2: Schemes of (a) Quantum repeater and (b) Quantum teleportation [27]. Detail description is in the text.

1.3 Some criteria for good quantum light sources

According to the literature [14,17,18,24,26], there are several key parameters to qualify quantum light sources, listed in the following [2,12,30,37]. The first three criteria

(now discussed in their simple "ideal" aspects) are more close to the fundamental demands for a "practical" quantum information processor, while the rest are about the quality of the quantum light source.

***Trigger on demand*:**

Considering the requirement of discrete operation for all quantum applications (even if some work is ongoing with continuous variable quantum computation), the quantum light sources must be operated, in other words, under pulse excitation, with a single "quantum" event generated per pulse.

***Location control*:**

This is essential for the integration of quantum light emitters into scalable and "integrated" quantum circuits. Without site-control capability, the complexity for achieving integration would grow to improbable levels.

Electrical injection:

This function would enable to replace bulky experimental setup with optical pumping scheme in integrated circuits. This supports the control over individual quantum light sources and opens up the possibility of scalability.

Purity:

For a single-photon source, $g^{(2)}(0)$, obtained at zero delay in a second-order auto-correlation spectrum, is a statistical value ranging from 0 to 1, and reveals how many multiphoton or single-photon events are detected over a time interval; see Chapter 5 for details. As the value is closer to zero, a "purer" single-photon source is achieved. This value is a crucial measure for LOQC [14]. On the other hand, a conventional figure applied to judge the "purity" of an entangled-photon source is the fidelity to a specific quantum state (other figures of merit exist such as Concurrence, Tangle, or Peres etc [31-34]), and these will be thoroughly discussed in Chapter 6 taking polarization entanglement as an example.

Indistinguishability:

The degree of indistinguishability, C, also ranging from 0 to 1, is used to quantify how identical two single-photons are. This can be obtained after a measurement in a Hong-Ou-Mandel (HOM) interferometer [35]. To have a maxima value C, two single-photons, either generated consecutively from the same emitter [36] or obtained from two separate sources [38], must have same energies and (in general) transform-limited linewidths [39]. Close to unity C is generally required in most quantum information protocols and especially needed in quantum repeater protocols, which distribute entanglement between quantum nodes within a quantum channel.

Photon extraction efficiency:

In this case, only the efficiencies of the emitter itself are considered, i.e. the loss in the optical components along the light collecting paths and the efficiencies of the detectors are not taken into account. It is related to the photon out-coupling to the first item in the optical paths, such as a lens or fiber, and the repetition rate within the quantum emitter. The former one could be possibly determined by the design of cavities (or reflecting mirrors), and the later one could be mainly controlled by the carrier lifetimes and shapes of the excitation pulses. This parameter directly indicates the performance of the operation speed and information-carrying capacity of a quantum light source.

Based on this list which should not be considered as fully exhaustive, one can have a brief guide to assess various quantum light sources, which will be presented in the next section.

1.4 Conventional quantum light sources

In this section, three common platforms for preparing quantum light sources are introduced, which are spontaneous parametric downconversion process in nonlinear crystal, the nitrogen vacancy in diamond, and semiconductor QDs.

1.4.1 Spontaneous parametric downconversion process

A conventional platform to prepare entangled photon pairs is through spontaneous parametric downconversion (SPDC) process, schematically depicted in Fig. 1.4.1.1 in one of its possible, alternative implementations [40,41]. A violet laser with frequency, υ_{pump}, is exploited to pump a non-linear $\chi^{(2)}$ crystal, such as β-phased barium borate (BBO), and, due to birefringence, two split beams are generated and named as signal and idler, with frequencies, υ_{signal} and υ_{idler}. In SPDC processes, the laws of energy and momentum conservation are obeyed:

$$\boldsymbol{h\upsilon_{pump} = h\upsilon_{signal} + h\upsilon_{idler}}, \tag{1.2}$$

$$\boldsymbol{h\vec{k}_{pump} = h\vec{k}_{signal} + h\vec{k}_{idler}}, \tag{1.3}$$

where $\boldsymbol{\vec{k}_i}$ indicates the wavevector of each photon beam. Also by proper cutting of the BBO crystal, two light cones can be observed whose polarization directions are orthogonal to each other (Type II correlation). Along the intersection lines of the two cones, polarization-entangled photon pairs can be spatially filtered out, and photons with indistinguishability in energy are insured by energy conservation, as well as photons in pairs separated in two cones are guaranteed by momentum conservation.

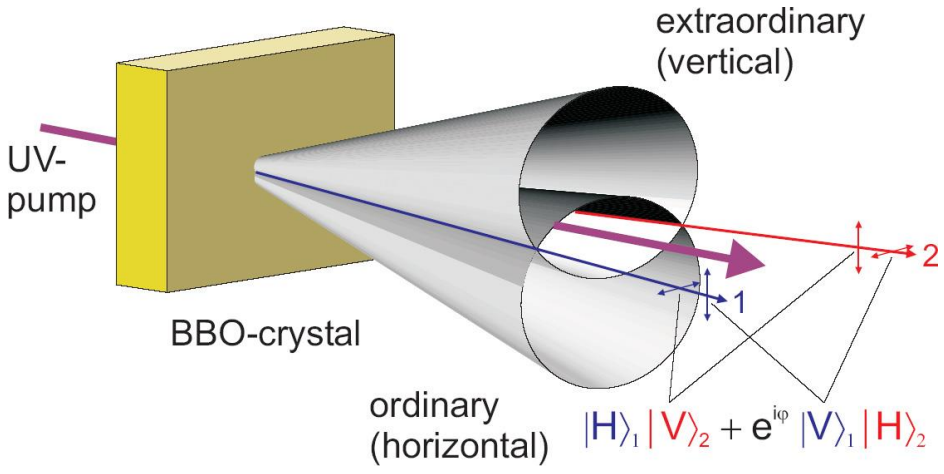

Fig. 1.3: Polarization-entangle photons generated by SPDC process [118].

Since the experimental setup required is relatively accessible and the system can be operated at room temperature, entangled photon pairs generated through SPDC processes have been utilized broadly to achieve, e.g., violation of Bell's inequality [40-43], quantum cryptography [44,45], long-haul quantum teleportation [27,28], multi-photon entanglement [46-48], heralded single-photon sources [49,50]. However, the experimental setup as such does not allow full integration for on-chip application nor the possibility of electrical injection (even if research is ongoing for equivalents in semiconductor waveguides.). Moreover, the pair number of entangled photons follows a Poissonian distribution not fulfilling the "trigger on demand" requirement. This is also the main challenge for any proposed quantum protocols since the multiphoton event will deteriorate the overall "quantumness" of the process.

1.4.2 Nitrogen vacancies in diamonds

Single-photon sources can also be obtained by single nitrogen-vacancy (NV) centers in diamonds [51-54]. An atomic structure of an NV center is shown in Fig. 1.4.2.1 [53], which is composed of a substitutional nitrogen atom and a nearby carbon vacancy. To form such NV centers, researchers started from type Ib synthetic diamond [51,52] or grown samples by chemical vapor deposition (CVD) [53-55], for example. The NV centers develop intrinsically or can be created by electron or neutron irradiation [56,57] (for carbon vacancies) and by successively introducing nitrogen atoms via high temperature (~900^{o}C) annealing. In the fluorescence spectrum of a single NV center, fluorescent decay, from excited state to ground state, would result in a sharp zero phonon line (ZPL) at 637 nm and a vibrationally-broadened emission peak (~ 620 to 740 nm) [51]. Strong antibunching behavior, an iconic feature of single-photon sources, has been observed from ZPLs [51-54].

Given its working principle, single-photons prepared by NV centers have high indistinguishability when emitted in the ZPL, which is promising for "measurement-based" entanglement [58]. Also, an electrically-pumped device has been demonstrated on a CVD-grown sample under room temperature operation [53]. In addition, spin-photon entanglement [59] and multipartite entanglement [60] have been realized based on this

system. However, the spatial control over "single" NV centers in diamond-based devices is still a challenging task even starting from site-controlled nanowire diamond [61].

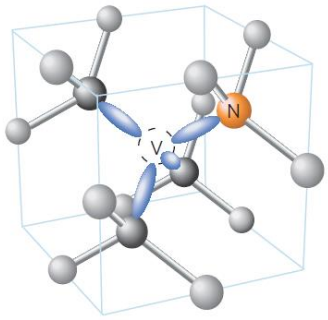

Fig. 1.4: Atomic structure of a NV center in diamond [53].

1.4.3 Epitaxial semiconductor QDs

The demand for a simple two-level transition can also be fulfilled by semiconductor QDs, due to their δ-function-like distribution of density of states, which also earned themselves the name of "artificial atoms" [62,63]. After optically pumping a single QD, luminescence from excitonic structures can be observed, typically three are dominating, which are the biexciton (XX -two electron and holes), the neutral exciton (X -one electron and one hole), and negatively/positively charged exciton (negative/positive trion, X^-/X^+, -i.e. an exciton paired to another charged particle in the dot), see Fig. 1.4.3.1. Thanks to this property, single-photon emission can be realized via all these excitonic transitions (as well as others) [64,65,66], and polarization-entangled photon pairs can be obtainable through the "ideal" XX-X-ground decay cascade once two electron-hole pairs are injected in the dot [67,68] (ideal here means that no fine-structure splitting existed in the intermediate X state, i.e. the X states are degenerate in polarization, fine-structure splitting is discussed more in the following sections). Moreover, the atomic-like level distribution largely suppresses the probability of detecting multiphoton events, as only dot repopulation events would cause that, allowing researchers to trigger quantum light sources on demand.

To form an epitaxial semiconductor QD, the dimensions of the grown materials must be smaller than or of-the-order-of the carriers' de Broglie wavelengths [63,64]. Indeed for carrier confinement, it is necessary to encapsulate material with a smaller bandgap into

another material with a larger one. To this end, three of the most conventional techniques to prepare QD planar samples are: Stranski-Krastanov-mode QDs [69,64-68], QDs by droplet epitaxy [70-73], and strain-free QDs [74,75], depicted in Fig. 1.4.3.2 (a) to (c), respectively.

In Fig. 1.4.3.2 (a), taking an InAs layer as an example, the SK-mode [69] growth on GaAs starts with layer-by-layer growth, then the growth mode turns into island-shape once the layer thickness goes beyond a critical thickness which varies e.g. with different indium content accordingly, inducing strain relaxation. As in the schematic, not only three-dimensional confined QDs are found but also a two-dimensional wetting layer is formed. Since this type of QDs can be straightforwardly prepared by MBE and MOVPE and the optical properties can be very good, it has been broadly applied to generate quantum light sources in the last two decades [64-68].

Droplet epitaxy for QDs is here exemplified with a GaAs/AlGaAs system [70], see Fig. 1.4.3.2 (b). After layer growth of AlGaAs on GaAs, metallic gallium is deposited without input of arsenic at low temperature, forming self-assembled gallium droplets. Subsequently, crystallization starts by atomic exchange between gallium and arsenic from the surface gradually to deep inside when the arsenic flow is re-introduced into the growth chamber. Finally GaAs QDs with good qualities can be achieved by proper annealing. This method can also be applied to the InAs/GaAs QD system with indium droplets [71]. Unlike SK-mode QDs, this method leaves no formation of a wetting layer leaving only QDs. Quantum light sources were demonstrated by this technique [72,73].

The degree of lattice mismatch between AlGaAs and GaAs is far smaller than the case of In(Ga)As. Based on this idea, AlGaAs/GaAs can be chosen for preparing (in a different way) strain-free QDs, as shown in Fig. 1.4.3.2 (c). The first step is to have a conventional SK-mode InAs QD array, then capping InAs QDs with a thin GaAs layer of ~ 10 nm thickness. GaAs nanoholes can be formed after selective etching between InAs and GaAs materials by introducing $AsBr_3$ flow [76]. Finally, the GaAs QDs are realized by growth of a GaAs QD layer on an AlGaAs barrier, and then capped with another AlGaAs barrier layer, and GaAs capping layers in sequence. Single-photon sources and entangled photon pairs have been reported based on this quantum dot system respectively [77,78].

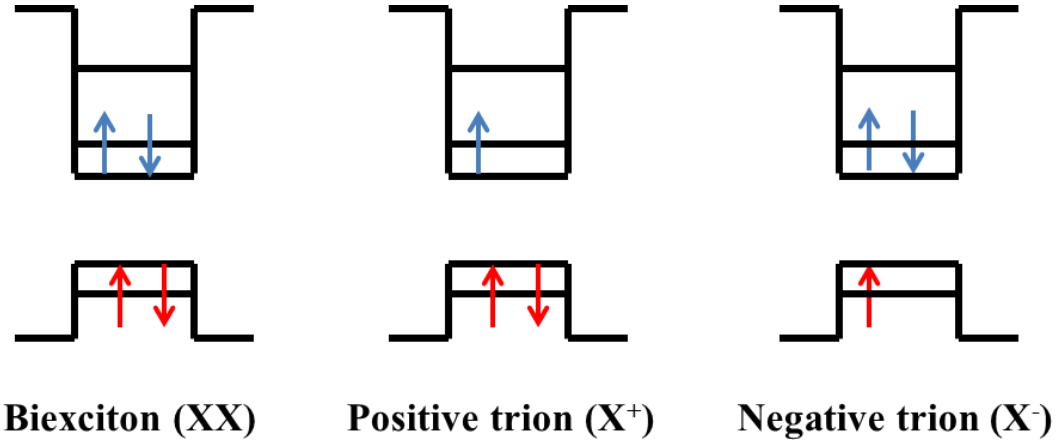

Fig. 1.5: Various excitonic transitions within a single QD.

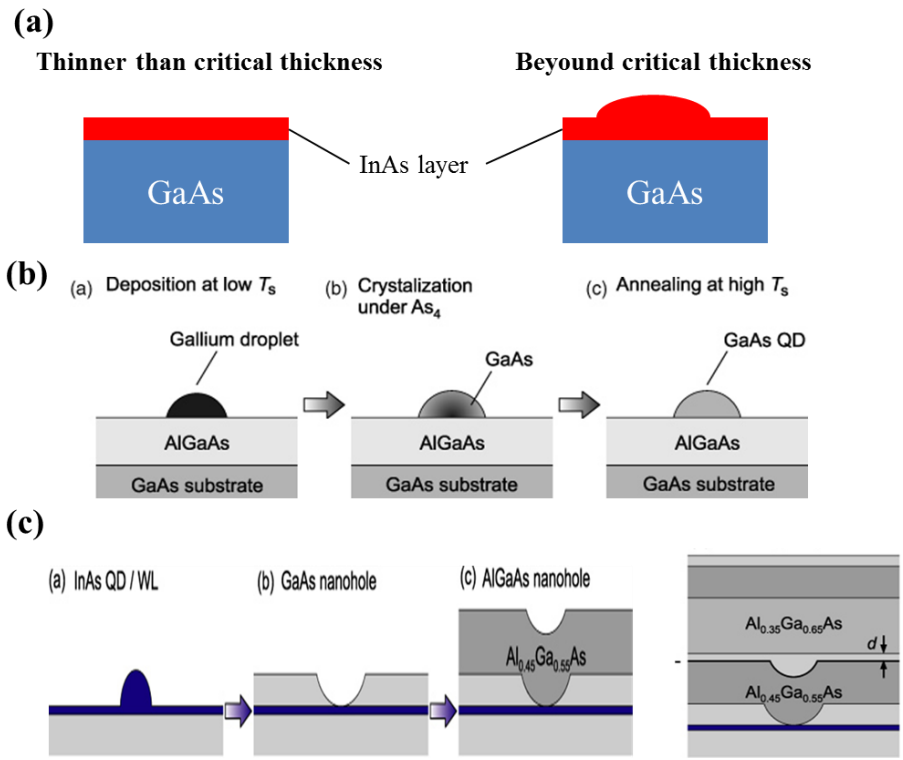

Fig. 1.6: Schematics of (a) SK-mode, (b) droplet epitaxy, and (c) strain-free QDs [63].

1.5 Challenges ahead with epitaxial semiconductor QDs

In the previous section, all the growth modes discussed show randomly-appearing nucleation sites [79], as shown in Fig. 1.5.0.1 (a). This severely limits further large scale integration into quantum processing systems with QDs. Also, the crystallographic orientation of the conventional substrate for these system is (100), which often results in an elongation of the QD shape along (110) leading to lower crystal symmetry, C_{2v} [80-82]. As a consequence the degeneracy of intermediate excitonic state isn't preserved anymore resulting in non-trivial FSS as shown in Fig. 1.5.0.1 (b). This impedes reconstruction by optical means, for example, of photon entanglement in the XX-X-ground cascade (more discussion on this in the following chapters).

To address these two issues, site-controlled QD systems and techniques to tune the FSS are discussed next.

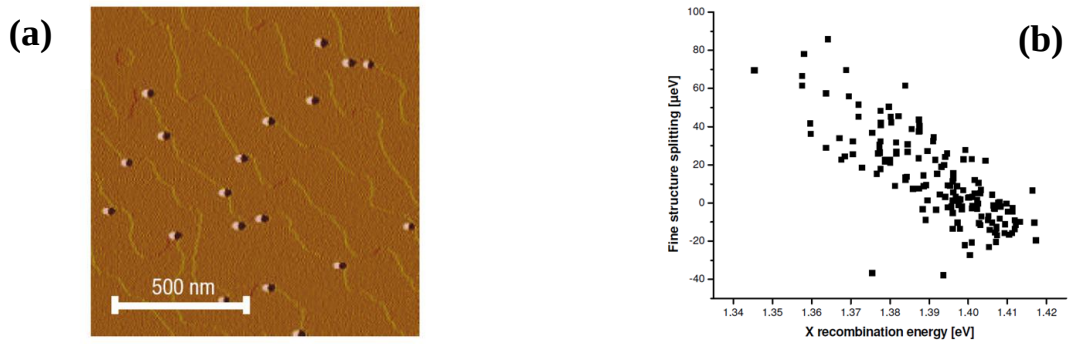

Fig. 1.2: Schemes of (a) Quantum repeater and (b) Quantum teleportation [27]. Detail description is in the text.

1.5.1 Site-controlled QD systems

Random nucleation sites are mainly due to non-uniform surface energies/sites on the growth surface resulting from fluctuations at the atomic scale. One strategy to avoid random nucleation is to create nanoholes or nano mesas prior to growths and to regulate the formation of QDs at the so obtained sites. Hence this idea involves two steps: substrate-pre-patterning and regrowth, while both of them increase the difficulties in control over defect densities as well as contamination incorporation, i.e., concern over poor optical output. Regarding the progress on this topic, the reader is referred to a recent review [63].

From the literature, techniques applied to pre-pattern the substrates are *ex-situ* atomic force microscope (AFM) lithography [83-85], electron-beam lithography (EBL) [86 87], nano-imprint lithography [88], laser interference lithography [89], *in-situ* scanning tunneling microscope lithography [90], amongst others. From those, some impressive results were reported in preparing quantum light sources. In 2012, C. Schneider et al., have realized single-photon emissions from micropillar LEDs with site-controlled QDs by the combination of EBL plus reaction-ion etching (RIE) and regrowth in molecular beam epitaxy (MBE) [87]. Later in the same year, K. D. Jöns et al. demonstrated nearly background-free single-photon emission and indistinguishable photon by optical pumping based on EBL, wet-etching and, most unique, the introduction of one seeded layer, which was used to improve optical properties [86].

Another site-controlled method is based on pre-patterning SiO_2 on top of InP, where apertures are left for selective growth during chemical beam epitaxy (CBE) [91]. Once the SiO_2 apertures are small enough, then the self-assembled QDs can be formed at the tips of the square pyramids after growth. State-of-the art performance was demonstrated by the generation of an optically-driven single-photon source [98], while no reports followed the prediction of entangled photon pairs in Ref. [91].

Instead of nano-patterning the substrates, the nucleation sites of QDs can also be controlled by the introduction of a buried oxide stressor layer [92]. This idea was composed of a two-step growth in metalorganic vapor phase epitaxy (MOVPE). The first step of growth involved a bottom section made of distributed Bragg-reflector (DBR) and Al(Ga)As stressor layers. Before the second step, circular mesas were defined by conventional photolithography and oxide apertures were formed by selective oxidation laterally in a furnace. At the second step, an InGaAs QD layer with layer thickness near critical thickness was chosen and capped with a GaAs layer. The site-controlled mechanism is: within the oxide apertures, tensile strain was induced due to volume reduction of the oxidized layer, then the preferred nucleation sites for QDs were formed, resulting from a local free energy-lowering. By means of this method, electrically driven single-photon emission was demonstrated with $g^{(2)}(0) = 0.05$ under continuous wave excitation [93].

Apart from the self-assembled QD systems introduced in Chapter 1.4.3, some endeavors have been shifted to other configurations to achieve site-controlled requirement. As an example, based on vapor-liquid-solid growth in MOVPE [94,95], nanowire QDs can be formed by metallic nanoparticles as catalysts and by introduction of a different precursor, see in Fig. 1.5.1.1. Since the position of the catalyst nanoparticles can be controlled, this method allows delivering site-controlled QDs. Optically-pumped single-photon sources and polarization-entangled photon pairs have been fabricated in sequence [96,97]. However, a challenge within this system is electrical injection, mainly due to the difficulty in doping issue as well as the non-planar configuration.

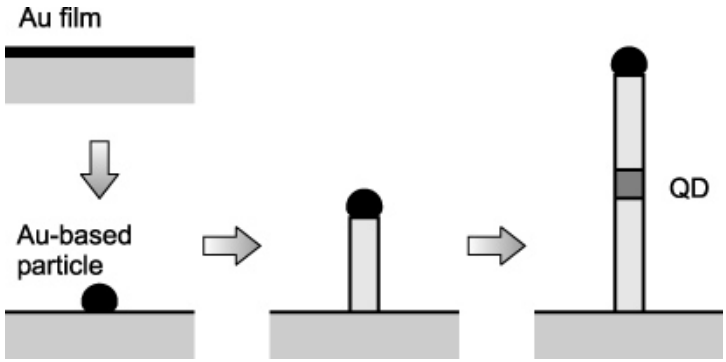

Fig. 1.8: Formation process of nanowire QDs [63]. (a) A layer of gold is deposited on a substrate, then (b) Au-based nanoclusters form after annealing. By means of Au-based nanoclusters as catalysts, (c) Nanowires are grown during metalorganic vapor phase epitaxy. (d) Formation of QD can be achieved by switching the grown materials (e.g., from GaAs to InAs).

1.5.2 Tuning of FSS

The general strategies applied to tune the FSS (i.e. the lack of degeneracy of the two X states when a QD is not fully symmetric, a pre-requisite for efficient entangled photon generation) within QDs can be briefly separated into two categories: improve the crystal symmetry and re-distribute the wavefunctions of electrons and holes by external physical quantities. The first group can be achieved by shifting the substrate orientation from (001) to (111)A [73] prior to growth, or by controlling the growth parameters during epitaxy [107,108], or by post-growth rapid thermal annealing [99,100]. In terms of FSS-tuning by

external fields, successful trials have been reported using magnetic field [68,101,102], in-plane electric field [103], vertical electric field [78], and, relevantly, strain induced by a piezoelectric field [104-106]. It is worth to mention all these tuning methods will induce wavelength shifting (as well as suppression of light intensity to some extent). Also the choice must consider the requirement of control over emitters *individually* and of possible electrical injection for future integration into a system.

1.6 Pyramidal QDs

Considering all the difficulties encountered in the above-mentioned QD systems, the alternative represented by pyramidal QDs (PQDs), with higher crystal symmetry and inherent site-control capability, as well as challenging (but possible) with electrical excitation, is a promising platform for preparing quantum light sources.

The main ingredients of forming arrays of PQDs are pre-patterned (111)B substrates [109] and growth rate anisotropies in metalorganic vapor phase epitaxy [110,111], with the detailed fabrication process discussed in Chapter 2.

In Fig. 1.6.1, the milestones achieved, based on PQDs, in the last two decades are listed in chronological order. In 1995, Y. Sugiyama et al. have demonstrated the first PQD array with pseudomorphic InGaAs/GaAs system with observation of photoluminescence and cathodoluminescence [112]. Three years later, after further reduction of the thickness of the well material, GaAs in this case, the level-to-level transitions from single apex-down PQD was detected in EPFL [113], which opened up the possibilities of utilizing the PQD system as a platform to prepare quantum light sources. From the same group, the first *optically-pumped* single-photon emitters with site-control ability have been demonstrated on the InGaAs/GaAs PQD system [114]. Speaking of entangled photon pairs, our group has successfully fabricated arrays of optically-pumped polarization-entangled photon emitters with the InGaAs:N/GaAs confinement system with a yield up to 15 % [115]. This was for the very first time among all semiconductor QD systems, the positions of the entangled photon emitters could be controlled.

However, considering the further integration into quantum circuits, quantum light sources with electrically-driven capabilities are an important plus. Nevertheless only few reports [116], so far, have been focused on electrical-pumping of the PQD system, possibly for two reasons: complicated fabrication process due to the non-planar configuration; plausible recognition of the in general poorer light properties compared to optically-driven ones.

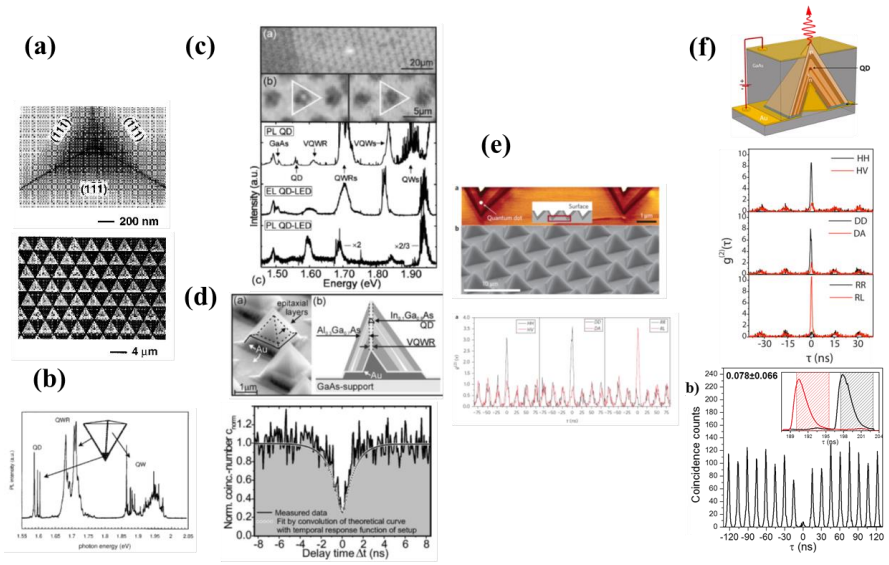

Fig. 1.9: Development of PQDs. (a) Selective growth within pyramidal recesses was first demonstrated in 1995 [112]. (b) First emission from a single GaAs PQD was reported in 1998 [113]. (c) In 2004, electroluminescence was detected for the first time [114], and in the same year (d) First optically-driven single-photon source was realized [116]. (e) In 2013, our group has achieved the first polarization-entangled photon pairs [115]. (f) In this thesis, we have realized the first ever single-photon diodes and, moreover, polarization-entangled diodes triggered on demand [120]

1.7 Thesis plan

In this thesis, the principle endeavor has been placed in the fabrication of light-emitting diodes with site-controlled PQDs, with the detailed fabrication process described in Chapter 2. Applying the growth model developed previously in our group, a theoretical study of the growth mechanism of InGaAs within pyramidal recesses can be found in Chapter 3. Investigations to reduce the probability of having negative trions during the

biexciton-exciton-ground decay cascades are discussed in Chapter 4. The realization of electrically-pumped single-photon sources and polarization-entangled photon pairs is presented in Chapter 5 and 6, respectively. Finally a brief summary of this thesis and future directions of this research are listed in Chapter 7.

Bibliography:

[1]: M. Fox, Quantum Optics: An Introduction, Oxford: Oxford University Press, 2006.

[2]: A. J. Shields, Nat. Photon., 1 (2007) 215.

[3]: B. Lounis and M. Orrit, Rep. Prog. Phys., 68 (2005) 1129.

[4]: R. Horodecki, P. Horodecki, M. Horodecki, and K. Horodecki, Rev. Mod. Phys., 81 (2009) 865.

[5]: A. Einstein, B. Podolsky, and N. Rosen, Phys. Rev., 47 (1935) 777.

[6]: N. Bohr, Phys. Rev., 48 (1935) 696.

[7]: J. S. Bell, Phys. 1 (1964) 195.

[8]: J. F. Clauser and M. A. Horne, Phys. Rev. D, 10 (1974) 526.

[9]: J. F. Clauser and A. Shimony Rep. Prog. Phys., 41 (1978) 1881.

[10]: N. Brunner, D. Cavalcanti, S. Pironio, V. Scarani, and S. Wehner, Rev. Mod. Phys., 86 (2014) 419.

[11]: J. L. O'Brien, A. Furusawa, and J. Vučković, Nat. Photon., 3 (2009) 687.

[12]: Y. Yamamoto, Quantum Inf. Process, 5 (2006) 299.

[13]: T. D. Ladd, F. Jelezko, R. Laflamme, Y. Nakamura, C. Monroe, and J. L. O'Brien, Nature, 464 (2010) 45.

[14]: E. Knill, R. Laflamme, and G. J. Milburn, Nature, 409 (2001) 46.

[15]: P. Kok, W. J. Munro, K. Nemoto, T. C. Ralph, J. P. Dowling, and G. J. Milburn, Rev. Mod. Phys., 79 (2007) 135.

[16]: D. Bouwmeester, A. K. Ekert, and A. T. Zeilinger, The Physics of Quantum Information (Springer, 2000).

[17]: C. H. Bennett, and G. Brassard, in Proceedings of IEEE International Conference on Computers, Systems, and Signal Processing, Bangalore, India, 175 IEEE, New York (1984)

[18]: A. K. Ekert, Phys. Rev. Lett. 67 (1991) 661.

[19]: C. H. Bennett, G. Brassard, and N. D. Mermin, Phys. Rev. Lett. 68 (1992) 557.

[20]: N. Gisin and R. Thew, Nat. Photon., 1 (2007) 165.

[21]: P. W. Shor, arXiv:quant-ph/9508027.

[22]: L. K. Grover, A fast quantum mechanical algorithm for database search, Proceedings, 28th Annual ACM symposium on the Theory of Computing, 1996.

[23]: W. K. Wootters and W. H. Zurek, Nature, 299 (1982) 802.

[24]: H.-J. Briegel, W. Dür, J. I. Cirac, and P. Zoller, Phys. Rev. Lett. 81 (1998) 5932.

[25]: N. Sangouard, C. Simon, H. de Riedmatten, and N. Gisin, Rev. Mod. Phys., 83 (2011) 33.

[26]: C. H. Bennett, G. Brassard, C. Crépeau, R. Jozsa, A. Peres, and W. K. Wootters, Phys. Rev. Lett. 70 (1993) 1895.

[27]: D. Bouwnmeester, J-W Pan, K. Mattle, M. Eibl, H. Weinfurter, and A. Zeilinger, Nature, 390 (1997) 575.

[28]: X-S Ma, T. Herbs, T. Scheidl, D. Wang, S. Kropatschek, W. Naylor, B. Wittmann, A. Mech, J. Kofler, E. Anisimova, V. Makarov, T. Jennewein, R. Ursin, and A. Zeilinger, Nature, 489 (2012) 269.

[29]: H. J. Kimble, Nature, 453 (2008) 1023.

[30]: M. Varnava, D. E. Browne, T. Rudolph, Phys. Rev. Lett., 100 (2008) 060502.

[31]: D. F. V. James, P. G. Kwiat, W. J. Munro, and A. G. White, Phys. Rev. A, 64 (2001) 052312.

[32]: V. Coffman, J. Kundu, and W. K. Wootters, Phys. Rev. A, 61 (2000) 052306.

[33]: A. Peres, Phys. Rev. Lett., 77 (1996) 1413.

[34]: A. J. Hudson, Ph.D. thesis, University of Cambridge, 2008, P. 101.

[35]: C. K. Hong, Z. Y. Ou, and L. Mandel, Phys. Rev. Lett., 59 (1987) 2044.

[36]: C. Santori, D. Fattal, J. Vuč ković, G. S. Solomon, and Y. Yamamoto

[37]: OSB

[38]: A. J. Bennett, R. B. Patel, C. A. Nicoll , D. A. Ritchie, and A. J. Shields, Nat. Phys., 5 (2009) 715.

[39]: A. V. Kuhlmann, J. H. Prechtel, J. Houel, A. Ludwig, D. Reuter, A. D. Wieck, and R. J. Warburton, Nat. Comm., 6 (2015) 8204.

[40]: Z. Y. Ou and L. Mandel, Phys. Rev. Lett., 61 (1988) 50.

[41]: P. G. Kwiat, K. Mattle, H. Weinfurter, and A. Zeilinger, Phys. Rev. Lett., 75 (1995) 4337.

[42]: A. C. Dada, J. Leach, G. S. Buller, M. J. Padgett, and E. Andersson, Nat. Phys., 7 (2011) 677.

[43]: M. Giusina, A. Mech, S. Ramelow, B. Wittmann, J. Kofler, Jörn Beyer, A. Lita, T. Gerrits, S. W. Nam, R. Ursin, and A. Zeilinger, Nature, 497 (2013) 227.

[44]: D. S. Naik, C. G. Peterson, A. G. White, A. J. Berglund, and P. G. Kwiat, Phys. Rev. Lett., 84 (2000) 4733.

[45]: A. V. Sergienko, M. Atatüre, Z. Walton, G. Jaeger, B. E. A. Saleh, and M. C. Teich, Phys. Rev. A, 60 (1999) R2622.

[46]: C-Y Lu, X-Q Zhou, O. Gühne, W-B Gao, J. Zhang, Z-S Yuan, A. Goebel, T. Yang, and J-W Pan, Nat. Phys., 3 (2007) 91.

[47]: W. Wieczorek, R. Krischek,N. Kiesel, P. Michelberger, Géza Tóth, and H. Weinfurter, Phys. Rev. Lett., 103 (2009) 020504.

[48]: X-C Yao, T-X Wang, P. Xu, H. Lu, G-S Pan, X-H Bao, C-Z Peng, C-Y Lu, Y-A Chen, J-W Pan, Nat. Photon., 6 (2012) 225.

[49]: S. Barz, G. Cronenberg, A. Zeilinger, and P. Walther, Nat. Photon., 4 (2010) 553.

[50]: C. Wagerknecht, C-M Li, A. Reingruber, X-H Bao, A. Goebel, Y-A Chen, Q. Zhang, K. Chen, J-W Pan, Nat. Photon., 4 (2010) 549.

[51]: C. Kurtsiefer, S. Mayer, P. Zarda, and H. Weinfurter, Phys. Rev. Lett., 85 (2000) 290.

[52]: R. Brouri, A. Beveratos, J-P Poizat, and P. Grangier, Opt. Lett., 25 (2000) 1294

[53]: N. Mizuochi, T. Makino, H. Kato, D. Takeuchi, M. Ogura, H. Okushi, M. Nothaft, P. Neumann, A. Gali, F. Jelezko, J. Wrachtrup, and S. Yamasaki, Nat. Photon., 6 (2012) 299.

[54]: C. Schreyvogel, V. Polyakov, R. Wunderlich, J. Meijer, and C. E. Nebel, Sci. Rep., 5 (2010) 12160

[55]: M. Füner, C. Wild, and P. Koidl, Appl. Phys. Lett., 72 (1998) 1149.

[56]: G. Davies and M. F. Hamer, Proc. R. Soc. London A 348 (1976) 285.

[57]: H. Hanzawa, N. Umemura, Y. Nisida, H. Kanda, M. Okada, and M. Kobayashi, PRB 54 (1996) 3793.

[58]: H. Bernien, Lilian Childress, L. Robledo, M. Markham, D. Twitchen, and R. Hanson, Phys. Rev. Lett., 108 (2012) 043604

[59]: E. Togan, Y. Chu, A. S. Trifonov, L. Jiang, J. Maze, L. Childress, M. V. G. Dutt, A. S. Sorensen, P. R. Hemmer, A. S. Zibrov, and M. D. Lukin, Nature, 466 (2010) 730.

[60]: P.Neumann, N. Mizuochi, F. Rempp, P. Hemmer, H. Watanabe, S. Yamasaki, V. Jacques, T. Gaebel, F. Jelezko, and J. Wrachtrup, Science, 320 (2008) 1326.

[61]:T. M. Babinec , B. J. M. Hausmann, M. Khan , Y. Zhang , J. R. Maze, P. R. Hemmer, and M. Lonc˘ar, Nat. Nano., 5 (2010) 195.

[62]: D. Bimberg, M. Grundmann, N. N. Ledentsov, Quantum Dot Heterostructures, John Wiley & Sons, 1999.

[63]: S. Kiravittaya, A. Rastelli, and O. G. Schmidt, Rep. Prog. Phys., 72 (2009) 046502.

[64]: P. Michler, A. Kiraz, C. Becher, W. V. Schoenfeld, P M. Petroff, L. Zhang, E. Hu, A. Imamoglu, Science, 290 (2000) 2282.

[65]: Z. L. Yuan, B. E. Kardynal, R. M. Stevenson, A. J. Shields, C. J. Lobo, K. Cooper, N. S. Beattie, D. A. Richie, and M. Pepper, Science, 295 (2002) 102.

[66]: R. M. Thompson, R. M. Stevenson, A. J. Shields, I. Farrer, C. J. Lobo, D. A. Ritchie, M. L. Leadbeater, and M. Pepper, Phys. Rev. B, 64 (2001) 201302(R)

[67]: O. Benson, C. Santori, M. Pelton, and Y. Yamamoto, Phys. Rev. Lett., 84 (2000) 2513.

[68]: R. J. Young, R. M. Stevenson, P. Atkinson, K. Cooper, D. A. Richie, and A. J. Shields, New J. Phys., 8 (2006) 29.

[69]: J. Venables, *Introduction to Surface and Thin Film Processes*, Cambridge, 2000.

[70]: T. Kuroda, M. Abbarchi, T. Mano, K. Watanabe, M. Yamagiwa, K. Kuroda, Kazuaki Sakoda[1], G. Kido, N. Koguchi, C. Mastrandrea, L. Cavigli, M. Gurioli, Y. Ogawa, and F. Minami, Appl. Phys. Exp., 1 (2008) 042001.

[71]: J. S. Kim and N. Koguchi, Appl. Phys. Lett., 85 (2004) 5893.

[72]: E. Stock, T. Warming, I. Ostapenko, S. Rodt, A. Schliwa, J. A. Töfflinger, A. Lochmann, A. I. Toropov, S. A. Moshchenko, D. V. Dmitriev, V. A. Haisler, and Dieter Bimberg, Appl. Phys. Lett., 96 (2010) 093112.

[73]: T. Kuroda, T. Mano, N. Ha, H. Nakajima, H. Kumano, B. Urbaszek, M. Jo, M. Abbarchi, Y. Sakuma, K. Sakoda, I. Suemune, X. Marie, and T. Amand, Phys. Rev. B, 88 (2013) 041306(R).

[74]: A. Rastelli, S. Stufler, A. Schliwa, R. Songmuang, C. Manzano, G. Costantini, K. Kern, A. Zrenner, D. Bimberg, and O. G. Schmidt, Phys. Rev. Lett., 96 (2004) 166101.

[75]: S. Kiravitta, R. Songmuang, N, Y, Jin-Phillipp, S. Panyakeow, and O. G. Schmidt, J. Cryst. Growth, 251 (2003) 258.

[76]: H Schuler, T Kaneko, M Lipinski, and K Eberl, Semicond. Sci. Technol., 15 (2000) 169.

[77]:M. Benyoucef, A. Rastelli, O. G. Schmidt, S. M. Ulrich, and P. Michler, Nanoscale Res. Lett., 1 (2006)172.

[78]: M. Ghali, K. Ohtani, Y. Ohno, and H. Ohno, Nat. Comm., 3 (2012) 661.

[79]: A. J. Hudson, Ph.D. thesis, University of Cambridge, 2008, P. 10.

[80]: R. Seguin, A. Schiliwa, S. Rodt, K. Pötschke, U. W. Pohl, and D. Bimberg, Phys. Rev. Lett., 95 (2005) 257402.

[81]: R. Singh and G. Bester, Phys. Rev. Lett., 104 (2010) 196803.

[82]: K. Jacobi, Prog. Surf. Sci., 71 (2003) 185.

[83]: H. Z. Song, T. Usuki, T. Ohshima, Y. Sakuma, Y. Kawabe, Y. Okada, K. Takemoto, T. Miyazawa, S. Hirose, Y. Nakata, M. Takatsu, and N. Yokoyama, Nanoscale Res. Lett., 1 (2006) 160.

[84]: J. Martin-Sánchez, G. Muñoz-Matutano, J. Herranz, J. Canet-Ferrer, B. Alén, Y. González, P. Alonso- González, D. Fuster, L. González, J. Martinez-Pastor, and F. Brinoes, ACS Nano, 3 (2009) 1513.

[85]: J. Herranz, L. González, L. Wewior, B. Alén, D. Fuster, and Y. González, Cryst. Growth Des., 15 (2015) 666.

[86]: K. D. Jöns, P. Atkinson, M. Müller, M. Heldmainer, S. M. Ulrich, O. G. Schmidt, and P. Michler, Nano Lett., 13 (2013) 126.

[87]: C. Schneider, T. Heindel, A. Huggenberger, T. A. Niederstrasser, S. Reitzenstein, A. Forchel, S. Höfling, Appl. Phys. Lett., 100 (2012) 091108.

[88]: J. Tommila, A. Tukianen, J. Viheriälä, A. Schramm, T. Hakkarainen, A. Aho, P. Stenberg, M. Dumitrescu, and M. Guina, J. Cryst. Growth, 323 (2011) 183.

[89]: P. Alonso-González, L. González, Y. González, D. Fuster, I. Fernádez-Martinez, J. Martin-Sánchez, and L. Abelmann, Nanotechnology, 18 (2007) 355302.

[90]: S. Kohmoto, H. Nakamura, T. Ishikawa, and K. Asakawa, Appl. Phys. Lett., 75 (1999) 3488.

[91]: D. Dalacu, M. E. Reimer, S. Frédérick, D. Kim, J. Lapointe, P. J. Poole, R. L. Williams, W. R. McKinnon, M. Korkusinski, P. Hawrylak, Laser Photon. Rev., 4 (2010) 283

[92]: A. Strittmatter, A. Holzbecher, A. Schliwa, J-H Schulze, D. Quandt, T. D. Germann, A. Dreismann, O. Hitzemann, E. Stock, I. A. Ostapenko, S. Rodt, W. Unrau, U. W. Pohl, A. Hoffmann, D. Bimberg, and V. Haisler, Phys. Status Solidi A, 209 (2012) 2411.

[93]: W. Unrau, D. Quandt, J-H Schulze, T. Heindel, T. D. Germann, O. Hitzemann, A. Strittmatter, S. Reitzenstein, U. W. Pohl, and D. Bimberg, Appl. Phys. Lett., 101 (2012) 211119.

[94]: K. Hiruma, H. Murakoshi. M. Yazawa, and T. Katsuyama, J. Cryst. Growth, 163 (1996) 226.

[95]: M. S. Gudiksen, L. J. Lauhon, J. Wang, D. C. Smith, and C. M. Lieber, Nature, 415 (2002) 617.

[96]: M. E. Reimer, G. Bulgarini, R. Akopian, M. Hocevar, M. B. Bavinck, M. A. Verheijen, E. P. A. M. Bakkers, L. P. Kouwenhoven, and V. Zwiller, Nat. Comm., 3 (2012) 737.

[97]: M. A. Versteegh, M. E. Reimer, K. D. Jöns, P. J. Poole, A. Gulinatti, A. Giudice, and V. Zwiller, Nat. Comm., 5 (2014) 5298.

[98]: S. Fredeick, D. Dalacu, D. Poitras, G. C. Aers, P. J. Poole, J. Lefebvre, D. Chithrani, and R. L. Williams, Microelectronics J., 36 (2005) 197.

[99]: R. J. Young, R. M. Stevenson, A. J. Shields, P. Atkinson, K. Cooper, D. A. Ritchie, K. M. Groom, A. I. Tartakovskii, and M. S. Skolnick, Phys. Rev. B, 72 (2005) 113305.

[100]: A. I. Tartakovskii, M. N. Makhonin, I. R. Sellers, J. Cahill, A. D. Andreev, D. M. Whittaker, J-P. R. Wells, A. M. Fox, D. J. Mowbray, M. S. Skolnick, K. M. Groom, M. J. Steer, H. Y. Liu, and M. Hopkinson, Phys. Rev. B, 70 (2004) 193303.

[101]: R. M. Stevenson, R. J. Young, P. Atkinson, K. Cooper, D. A. Ritchie, and A. J. Shields, Nature, 439 (2006) 179.

[102]: R. M. Stevenson, R. J. Young, P. See, D. G. Gevaux, K. Cooper, P. Atkinson, I. Farrer, D. A. Ritchie, and A. J. Shields, Phys. Rev. B, 73 (2006) 033306.

[103]: B. D. Gerardot, S. Seidl, P. A. Dalgarno, R. J. Warburton, D. Granados, J. M. Garcia, K. Kowalik, O. Krebs, K. Karrai, A. Badolato, and P. M. Petroff, Appl. Phys. Lett., 90 (2007) 041101.

[104]: R. Trotta, J. Martín-Sánchez, J. S. Wildmann, G. Piredda, M. Reindl, C. Schimpf, E. Zallo, S. Stroj, J.Edlinger, and A. Rastelli, Nat. Comm., 7 (2016) 10375.

[105]: R. Trotta, E. Zallo, C. Ortix, P. Atkinson, J. D. Plumhof, J. van den Brink, A. Rastelli, and O. G. Schmidt, Phys. Rev. Lett., 109 (2012) 147401.

[106]: R. Trotta, J. Martín-Sánchez, I. Daruka, C. Ortix, and A. Rastelli, Phys. Rev. Lett., 114 (2015) 150502.

[107]: R. J. Young, R. M. Stevenson, A. J. Shields, P. Atkinson, K. Cooper, D. A. Ritchie, K. M. Groom, A. I. Tartakovskii, and M. S. Skolnick, Phys. Rev. B, 72 (2005) 113305.

[108]: G. Juska, E. Murray V. Dimastrodonato, T-H Chung, S. T. Moroni, A. Gocalinska, and E. Pelucchi, J. Appl. Phys., 117 (2015) 134302.

[109]: Y. Tarui, Y. Komiya, and Y. Harada, J. Electrochem., Soc., 118 (1971) 118.

[110]:E. Pelucchi, V. Dimastrodonato, A. Rudra, K. Leifer, E. Kapon, L. Bethke, P. Zestanakis, and D. D. Vvedensky, Phys. Rev. B, 83 (2011) 205409.

[111]:V. Dimastrodonato, E. Pelucchi, and D. D. Vvedensky, Phys. Rev. Lett., 108 (2012) 256102.

[112]: Y. Sugiyama, Y. Sakuma, S. Muto, and N. Yokoyama, Appl. Phys. Lett., 67 (1995) 256.

[113]: A. Hartmann, Y. Ducommun, L. Loubies, K. Leifer, and E. Kapon, Appl. Phys. Lett., 73 (1998) 2322.

[114]: M. H. Baier, E. Pelucchi, E. Kapon, S. Varoutsis, M. Gallart, I. Rober-Phillip, and I. Abram, Appl. Phys. Lett., 84 (2004) 648.

[115]: G. Juska, V. Dimastrodonato, L. O. Mereni, A. Gocalinska, and E. Pelucchi, Nat. Photon., 7 (2013) 527.

[116]: M. H. Baier, C. Constantin, E. Pelucchi, and E. Kapon, Appl. Phys. Lett., 84 (2004) 1967.

[117]: L. A. Lugiato, A. Gatti, and E. Brambilla, J. Opt. B: Quantum Semiclass. Opt., 4 (20002) S176.

[118]: C. Erven, M.S. thesis, University of Waterloo, 2007, P. 22.

[119]: M. H. Baier, C. Constantin, E. Pelucchi, E. Kapon, Appl. Phys. Lett., 98 (2011) 021106.

[120]: T. H. Chung, G. Juska, S. T. Moroni, A. Pescaglini, A. Gocalinska, and E. Pelucchi, Nat. Photon., 10 (2016) 782.

[121]: M. Giustina, M. A. M. Versteegh, S. Wengerowsky, J. Handsteiner, A. Hochrainer, K. Phelan, F. Steinlechner, J. Kofler, J-Å Larsson, C. Abellán, W. Amaya, V. Pruneri, M. W. Mitchell, J. Beyer, T. Gerrits, A. E. Lita, L. K. Shalm, S. W. Nam, T. Scheidl, R. Ursin, B. Wittmann, and A. Zeilinger, Phys. Rev. Lett., 115 (2015) 250401.

[122]: Lynden K. Shalm et al., Phys. Rev. Lett., 115 (2015) 250402.

[123]: B. Hensen, H. Bernien, A. E. Dréau, A. Reiserer, N. Kalb, M. S. Blok, J. Ruitenberg, R. F. L. Verneulen, R. N. Schouten, C. Abellán, W. Amaya, V. Pruneri, M. W. Mirchell, M. Markham, D. J. Twitchen, D. Elkouss, S. Wehner, T. H. Taminiau, and R. Hanson, Nature, 526 (2015) 682.

Chapter 2:

Device fabrication process

2.1 Pre-patterned substrates

First and foremost, we detail the steps of the substrate pre-patterning, which can be realized by conventional photolithography and wet chemical etching. The flow chart is shown in Fig. 2.1. For most samples discussed in the following chapters, the pitch lengths of the pyramidal recesses and side lengths were designed as 7.5 μm (7.5 μm being the pitch, the rest of the geometrical features adjusting accordingly), while deviations will be specified if changed for specific studies.

As first step, a-layer of SiO_2 is sputtered on a semi-insulating (SI) GaAs (111)B substrate. Then, to perform photolithography, hexamethyldisilazane (HMDS) and S1805 positive photoresist (PR) (Dow Electronic Materials) are spun in sequence on top of the SiO_2-coated GaAs. The first organosilicon compound is an adhesive promoter for the following PR. The step of UV exposure is carried out by a Karl Süss MA6 mask aligner. MF 319 (Dow Electronic Materials) is applied as developer for the exposed PR. Exposure and developing times are around 4 s and 25 s, respectively. To prevent the residual PR from contaminating the to-be-exposed GaAs surface, the procedure includes a 2-minute treatment in an oxygen plasma chamber, after the developing stage. Subsequently, the hexagonally-arranged array of triangles is transferred to the SiO_2 layer by etching in buffered hydrofluoric acid (BHF) for 10 s. Then the PR-stripping can be achieved through bathing in warmed acetone and isopropanol (IPA). Three (111)A facets of pyramidal recesses will emerge after etching in 5% Br-methanol. The required etching duration will vary according to the defined sizes of the pitch/recesses [1]. In the case of the 7.5 μm pitch, the etching time is ~8 s. After further cleaning of the PR residue in acetone and IPA, SiO_2 removal is performed by BHF etching for 5 minutes. Finally, the pre-patterned substrates will be cleaned by oxygen plasma, and the last step is the “removal” of the native oxide from GaAs surface by means of etching in 48 % HF until the surface reaches a hydrophobic character, , which is around 3 minutes for GaAs in general. Here we use the conventional

terminology as typically applied in cleanrooms for hydrophobicity, indicating only low water adhesion, as can be checked by tilting the substrate without any precise contact angle measurement; it should be said that the topic of hydrophobicity in III-V materials is surprisingly little explained, see for example Ref. 14. A representative final image captured by scanning electron microscopy (SEM) of a pre-patterned substrate is shown in Fig. 2.1 (h).

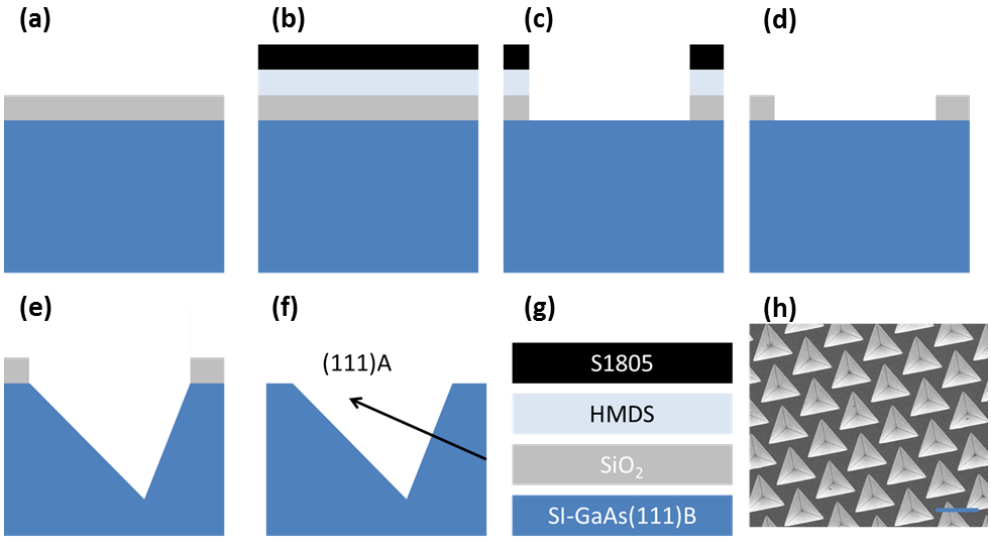

Fig. 2.1: Procedure for pre-patterning substrates. (a) SiO_2 evaporation, (b) Spin-coating of HMDS and S1805 in sequence, (c) General photolithography, (d) Removal of photoresist, (e) Etching in Br:methanol, (f) Elimination of SiO_2 by HF, (g) Color indication for used materials, and (h) Top-viewed representative SEM pattern with scale of 7.5 µm.

2.2 Growth inside pyramidal recesses by metalorganic vapor phase epitaxy (MOVPE)

2.2.1 MOVPE system

All the samples discussed within this thesis were grown in a low-pressure (20 mbar) metalorganic vapour phase epitaxy (MOVPE) system (Aixtron 200, single two inch sample holder) with nitrogen as carrier gas. It is worth mentioning that the purity of nitrogen is improved by a process of double purification, which was experimentally verified to deliver very-narrow emission linewidths from single AlGaAs/GaAs quantum wells (< 400 µeV) [2]

and sharp excitonic emissions from single pyramidal quantum dots (< 18 μeV, below the resolution limit of our set-up) [3]. Precursors used for the III-V element sources, gallium, aluminum, indium, and nitrogen are trimethylgallium (TMGa), TMAl, TMIn, and dimethylhydrazine (DMHy). In addition, disilane (Si_2H_6) and tetrabromomethane (CBr_4) are applied during the growth for the n-doped and p-doped layers, respectively.

2.2.2 Growth mechanisms

The growth of semiconductor materials inside our pre-defined pyramidal recesses (which we will discuss extensively in Chapter 3), obviously non-planar surfaces, requires considering not only the adatom migration mechanism but also the facet-dependent precursor decomposition rates, as demonstrated by extensive works in our group [4-8]. The two phenomena are indeed competing with each other during the growth. Decomposition induced growth rate anisotropy (GRA, i.e. different growth rates on the facets) tends to increase the lateral growth, while adatom diffusion tends to increase the growth rate at the centre of the recesses, depleting sidewalls growth, a process called "capillarity" in the early literature (we will discuss more extensively this point in Chapter 3) . Once the two effects reach balance, then a self-limited growth is achieved, allowing a consistent base width during the following epitaxial growth. This process is fundamentally independent from the exact recess shape and dimensions and provides the grower with a good control of the QD configuration.

Indeed, as discussed, after the substrates are pre-patterned, there will be 3 Ga-terminated (111)A sidewalls, one As-terminated (111)B bottom facet and the (111)B-unpatterned surface between the pyramidal recesses, as seen in Fig. 2.2 (a). As observed experimentally, the III-V layers would "happily" grow on the (111)A facets but significantly less on (111)B-unpatterned surface. This produces strong deposition on the lateral facets, and very little on the (111)B surfaces inducing the so-called GRA, shown in Fig. 2.2 (b), were little growth is assumed also at the (111)B base.[4–8].

Once the precursors are decomposed, the diffusion of adatoms dominates the outcome of material growths. Following surface dynamics, the adatoms would tend to diffuse to the bottoms of the pyramidal recesses, strongly contributing to their growth, and,

possibly, leading to the planarization of the recesses (the idea of "capillarity" is indeed that, i.e. this process reduces the overall surface energy). Following this process, the growth rate at the bottom (111)B can be higher than that of the sidewalls, as depicted in Fig. 2.2 (c). This is, for example, observed in the growth by molecular beam epitaxy (MBE), when the substrate surface contains pre-defined nanopits [12,13].

A word of caution: as we will briefly discuss in Chapter 3, the nature of this effect in pyramidal recess is still under debate in the literature (surface energy?, adatom sticking coefficient?), since recent reports on growth simulations deliver a good fit to the experimental findings even without taking capillarity explicitly into account [6]; we will not further discuss this here, and we address the interested reader to Ref. [6,7] for more details.

The self-limiting growth profile (SLP), described in Fig. 2.2 (d), is the result of both the two effects mentioned. From reference 7 and 8, the growth time, or grown layer thickness, required to reach the SLP is primarily dominated by parameters such as growth temperature and alloy content. For most of the discussed samples in this thesis, the growth temperature of the QD layer is at 730^{o}C (nominal) with base layer material GaAs, which needs ~90 nm to reach the SLP. In addition, it is worth to mention that the SLP is unique to MOVPE reactors, as in MBE systems the lack of DRA in the growth mechanism also involves a lack of high deposition rate on the side walls, finally making impossible the mechanism for SLP (there will always be a higher growth rate at the (111)B base, which will constantly enlarge during the growth process). This means that site-controlled Pyramidal QDs can only be obtained by MOVPE.

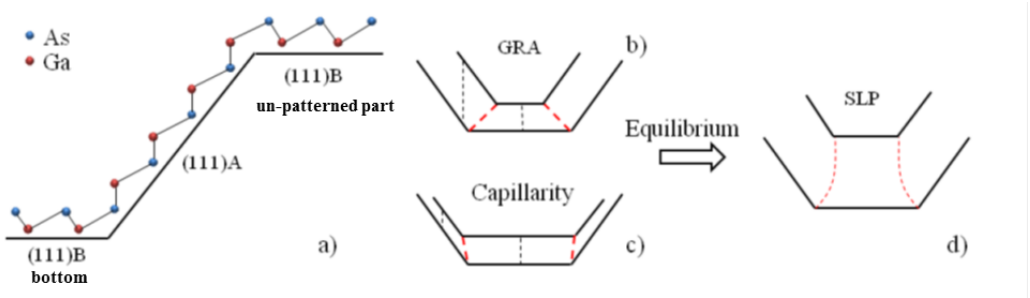

Fig. 2.2: (a) Atomic arrangements of GaAs(111)A and GaAs(111)B, and schemes of (b) Growth rate anisotropy, (c) capillarity effect, and (d) Self-limiting growth profile [20].

2.2.3 Formation of multi-nanostructures inside pyramidal recesses

In Fig. 2.3, the three-dimensional configuration of the structure complexity within pyramidal recesses is described. The sketch is based on the structure of a single InGaAs QD layer, sandwiched by GaAs layers and cladded by AlGaAs layers. Considering both geometry and alloy segregation [7,9], the site-controlled InGaAs QD is formed automatically at the center of pyramidal recess in conjunction with three InGaAs lateral quantum wires (LQWRs) and three InGaAs lateral quantum wells (LQWs). In addition, three AlGaAs vertical quantum wires (VQWRs) and three vertical quantum wells (VQWs) for the same fundamental epitaxial mechanisms (fast diffusion adatoms give segregation: In diffuses more than Ga, which in turn diffuses more than Al), but with thicker layer thickness, as the AlGaAs cladding layers are thicker than InGaAs layer. It should also be said that recently, newly reported corner QDs (CQDs) were observed, generated during the QD layer growth as independent nanostructures from the QD, and located somewhere at the top of the corners of the pyramidal recesses, as reported in Ref. [10] and discussed in Chapter 3.

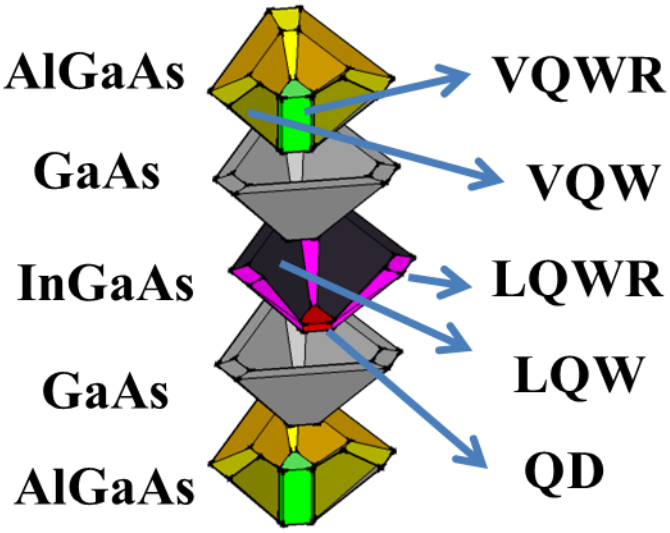

Fig. 2.3: Representative three-dimensional configuration of the grown structures within a pyramidal recess. The VQWRs and VQWs are formed due to strong Ga segregation, while the LQWRs and are because of In segregation. On the other hand, due to the heterogeneous material stacking, the LQDWs and the QD are taken shaped.

Even though there are so many nanostructures emitting in a pyramidal structure other than just the QDs of interest, in general (there are exceptions) the emissions from site-controlled QDs can still be isolated in the luminescence spectra due to the different emitting energies. A representative photoluminescence spectrum is displayed in Fig. 2.4. In general, QDs have the lowest emitting energy, compared to the other quantum structures, which is also favorable for carrier injection.

As mentioned, there are exceptions. For example if a proper control of growth parameters, such as QD layer thickness or growth temperature, is not put in place, a crossing of the QD's and LQWRs' emissions may happen, as we reported in Ref 10. Indeed, if the growth temperature does not fall in the right range, there is a risk that the emission from the QDs is overshadowed by the LQWs' broad emission [10].

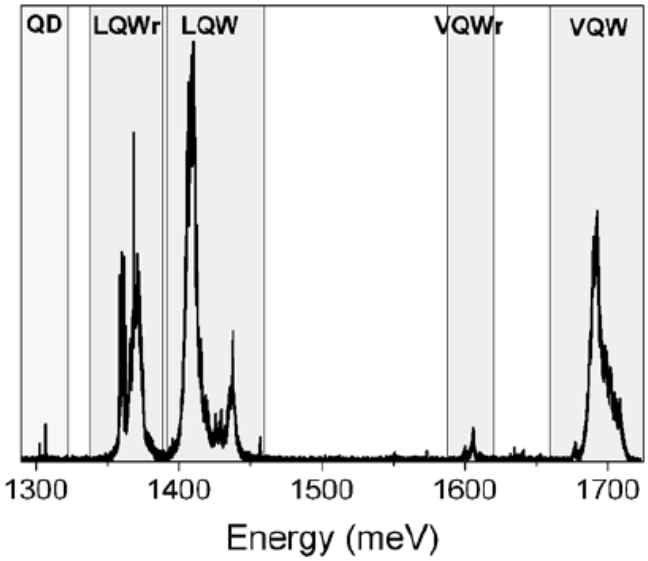

Fig. 2.4: A representative photoluminescence spectrum from structures within a single apex-up pyramid, containing a $In_{0.25}Ga_{0.75}As$ QD layer with GaAs barriers and $Al_{0.55}Ga_{0.45}As$ cladding layers. All nanostructures emit at different wavelengths [36].

2.2.4 Epitaxial structures

The typical pyramidal growth process would be: after substrate deoxidation, a (thin) layer of GaAs is grown first as a buffer layer, aimed at smoothing the surface for subsequent growth. Then, typically, there are two AlGaAs layers with high aluminum

contents grown as etch-stop layers. This is achieved by exploiting the selectivity of NH4OH solution for AlGaAs with high aluminum concentration (not etched) and GaAs (etched) [18], which are designed for the post-growth "backetching" process, details in Chapter 2.3.2. The aluminum content of the first etch-stop layer generally ramps from 0.45 to 0.8, while the second one is fixed at 0.8. For contact processing purposes, in the light-emitting diodes, an AlAs layer was added and grown after the GaAs , as we will describe in the following chapter. Subsequently, the InGaAs(N) QD layer is sandwiched by GaAs (inner) barriers and AlGaAs outer cladding layers. In conventional optically-driven devices, the aluminum contents of the AlGaAs cladding layers are always ~0.55. However, Al composition was varied for current confinement in the electrically-pumped diodes, whose design is detailed in later sections. Without special mention, the indium contents in InGaAs QD layers were fixed at 0.25; in general the tuning of the emission energies was achieved by means of changing the nominal QD thicknesses only. The application of nitrogen within the QD layer acted as a surfactant, which we utilized to improve the uniformity among the grown QDs in terms of emission energy [11].

2.3 Post-growth processes

2.3.1 Necessity of surface etching

During the growth in the pyramidal recesses, the epitaxial growth would happen not only along the desired {111}A direction, but there would be also irregularly-grown facets at the interface of (111)A and top (111)B surfaces, as well as the erratic features on the planar (111)B surface. The process to remove these undesired byproducts is called "surface etching" in the literature [15], allowing to prevent the QD emission from being coincidently shadowed by the luminescence of the irregularly grown nanostructures.

Surface etching (deemed necessary in the literature) is a self-aligned etching procedure, whose (approximate) scheme is shown in Fig. 2.5. It starts with spin-coating of photoresist on the grown sample, baking at ~90 oC and ~115 oC in sequence. Then an oxygen plasma process is used to fully eliminate the photoresist from the planar surface and to reduce its thickness in the recesses. Subsequently, in ideal conditions, the unprotected irregular growth can be etched away by an isotropic etchant as diluted sulfuric acid, for example. In

the end, the photoresist is removed, for example, by an acetone bath, and finally isopropyl alcohol is utilized to finish up the sample cleaning.

The evaluation, nevertheless, of the photoresist-etching time by oxygen plasma is not very accurate. This can be determined in principle by a reflectivity measurement, which is very accurate on planar substrates, but severely limited in performance when a non-planar structure is considered. Indeed, the calibration setting of the systems used is based on planar surfaces, but this leads to misinterpretations of the real thickness of the photoresist in the holes, for example.

Overall, we found surface etching as a source of irreproducibility on the final structures. Moreover, from the literature, there is no discussion about the optical characterization of back-etched PQDs (i.e. samples were the substrate is removed and the pyramids stand apex-up, the usual configuration we use for maximum photon collection efficiency) with or without surface etching. One can find only a comparison of "as grown" PQDs (inverted pyramids) between with or without surface etching [15].

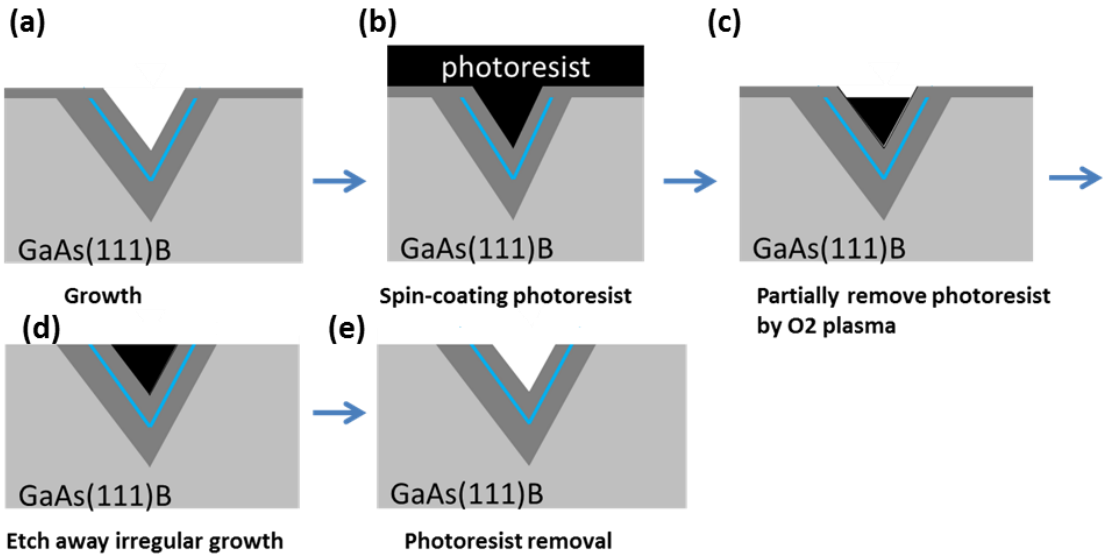

Fig. 2.5: Flow chart of surface etching. (a) Epitaxy within pyramidal recesses, (b) Spin-coating photoresist (S1805), (c) Partial removal of photoresist by O_2 plasma, (d) Etch in sulfuric acid solution, and (e) Removal of photoresist residual.

To test the necessity of using the highly unreliable surface etching for the case of apex-up PQDs, samples were back-etched by the conventional process described later on, neglecting surface etching. A representative spectrum resulting after this process is displayed in Fig. 2.6. Inspecting the spectrum in Fig.2.6 the peaks of exciton (X), biexciton (XX), and negatively-charged exciton (X^-) can be clearly observed, and no shadow effect from the irregular growth could be observed in this sample, nor in any subsequent ones in the apex-up configuration and process. For this reason we abandoned surface etching in our samples after obtaining this characterization data.

A possible interpretation of this output is that the recombination of carriers after excitation is turned into non-radiative process due to trapping effect at the interface of the semiconductor and the gold layer which is deposited for backetching on the sample surface. As described later on, gold is deposited for structural integrity in the subsequent bonding as well as in the role of a mirror to reflect the emission of the QDs. Nevertheless, this is only a hypothesis, and more relevant evidence would still be required for confirmation.

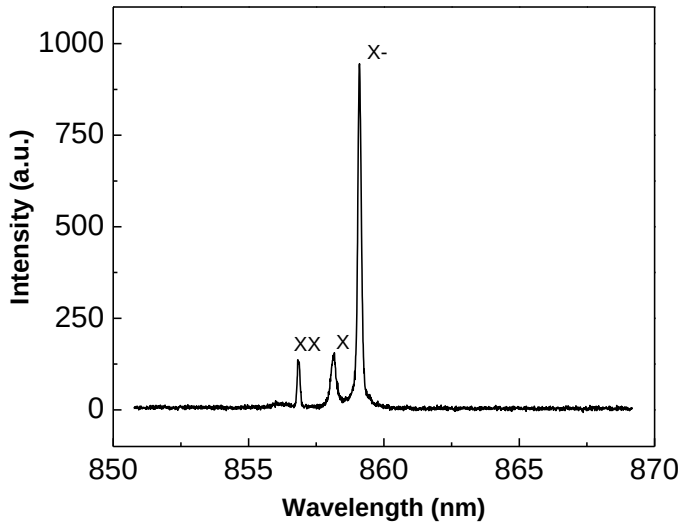

Fig. 2.6: Representative photoluminescence spectrum measured at T = 8 K of apex-up PQD without surface etching.

2.3.2 Back-etching

As-grown PQDs are inverted pyramids, as discussed. The light extraction rate performance is known to be very poor in this geometry [15], considering the total internal

reflection induced by the refractive path of the emitted luminescence. The comparison in light extraction paths between inverted and apex-up PQDs is shown in Fig. 2.7 (a) and (b), respectively. So, a more efficient way is to bond the upside-down sample onto another supportive material [15], for example a GaAs(100) substrate in our case, then eliminate the original SI-GaAs(111)B substrate keeping the pyramids intact, allowing the apex-up PQDs to be revealed (see Fig. 2.9 for example, and subsequent sessions). Postponing the discussion of the substrate removal to later on, it is clear that the bonding technique must be robust enough to prevent backetched samples from cracking during the subsequent (device) processes and to remain stable after the cooling cycles, since the operation temperature of optical characterization is typically at ~8 K. We will describe in the following sub-sections how we improved on the state of the art on this issue.

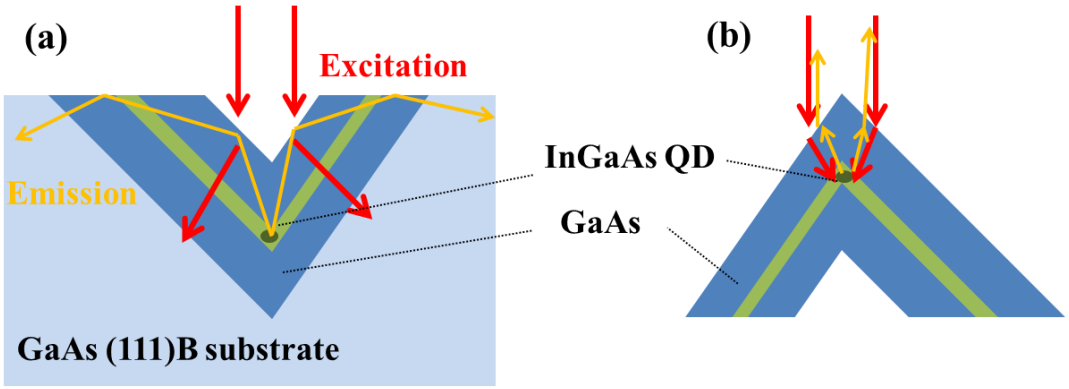

Fig. 2.7: Light-emitting paths of (a) inverted and (b) apex-up PQDs.

2.3.2.1 Evolution of bonding techniques

As we will discuss in 2.3.2.2 one step of the backetching process as we developed, involves mechanical thinning. The mechanical thinning was added during my PhD, and indeed it improves the results of the thinning process, both, simply, in regards of time consumption and also in better overall surface roughness. We will discuss this in more details later.

However, there is an awkward problem arising if the mechanical thinning is utilized. That is a stronger “lateral” force, compared to the case of simple wet etching in chemical solution (the traditional way of doing it). During the mechanical thinning we observed an

increase in the possibility of separating the thinned membrane with PQDs and the host GaAs substrate, especially when the sample is thinned down thinner than 20 μm. A representative "sample-broken" image is shown in the inset of Fig. 2.8 (a). The reason for this issue is the bonding strength between the original substrate and host one is not "uniformly" strong enough to stick together during the subsequent process of backetching.

The bonding method, leading to the result shown in Fig. 2.8 (a), was a conventional Au-to-Au thermocompression process [16]. It starts from coating Ti/Au layer on the epitaxial side of sample, which is after surface etching if performed, then the sample is turned upside down on a Ti/Au-coated host GaAs substrate, finally both are bonded together thermocompresively.

Another possible solution is to enlarge the bonding strength in an Au-to-SnAu reflow process. In this case, the Ti/Au-coated sample is bonded on a SnAu-coated ceramic substrate instead of a Ti/Au-coated GaAs substrate. The result by this process is displayed in Fig. 2.8 (b). The ensemble of the sample still remains intact even though it is thinned down to only 12 μm left. Thus the time required for the final step of chemical etching could be reduced significantly without the scarification of a large piece of sample.

This bonding method works for either the ordinary optical characterization or electrical-driven applications. However, one of our future directions is to bond the sample on Au-coated piezoelectric materials, allowing us to tune the FSS and exciton wavelength by external strain [17]. To meet the requirement, the SnAu foil could be utilized to behave like a "glue" through the reflow process. From Fig. 2.8 (c), the result of a test, in which the SnAu foil was inserted between the Ti/Au-coated sample and Ti/Au-coated host GaAs substrate, indicates a robust bonding strength could be achieved as well.

The decision of choosing either SnAu-coated ceramic substrates or usage of SnAu foil only depends on the further application, and the bonding strength would not make significant difference. The bonding steps are summarized in Fig. 2.8. As a result, most samples discussed in the thesis were bonded by assistance of a SnAu foil due to its flexibility.

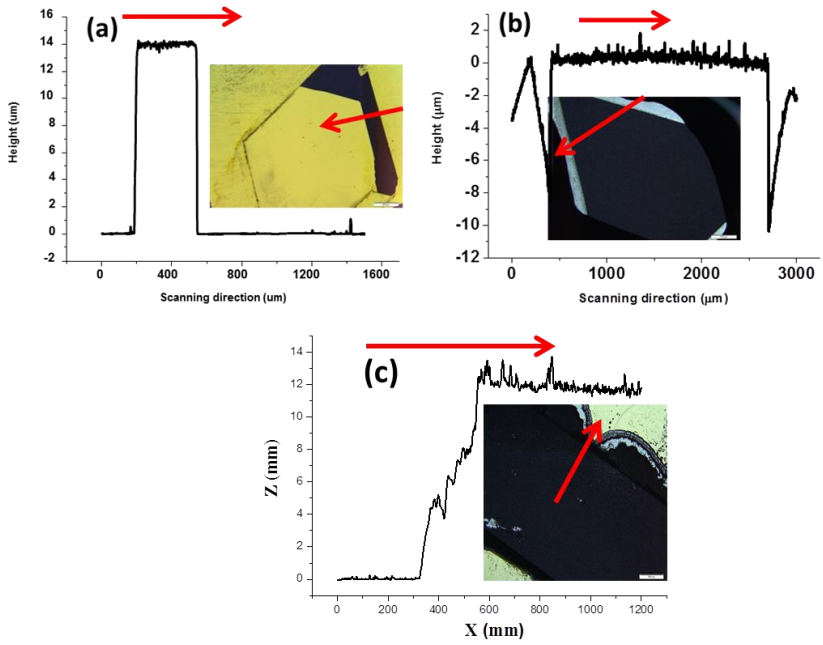

Fig. 2.8: Representative profilometer scanning profiles of samples after mechanical thinning with (a) Au-to-Au thermocompressive bonding, (b) Au-to-SnAu reflow process, and (c) SnAu foil. The inserted images are showing the scanning path with the assistance of *the red arrows.*

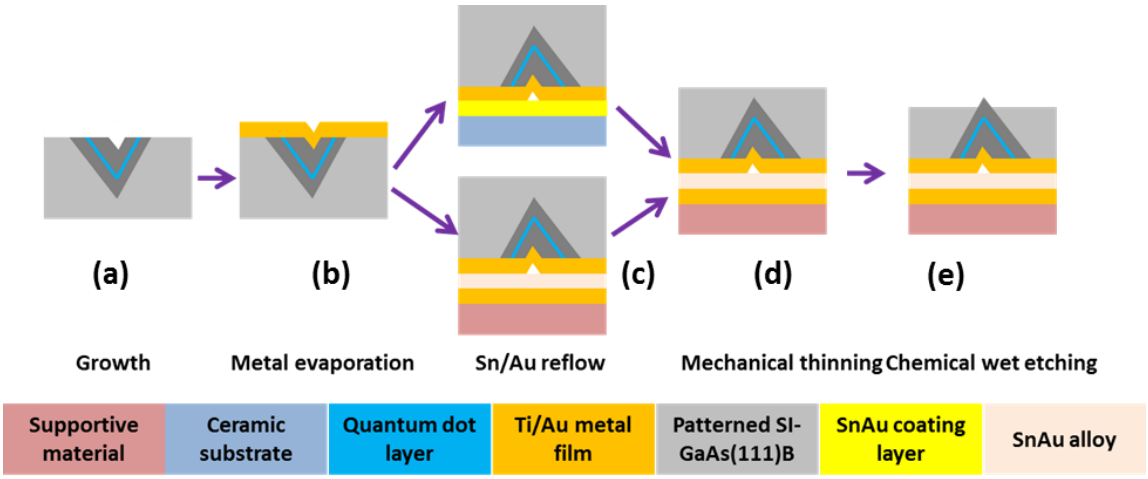

Fig. 2.9: Scheme of bonding steps and indication of materials used. (a) Growth within pyramidal recesses, (b) Metal evaporation, (c) Bonding on either (top) an SnAu-coated ceramic substrate or (bottom) an Au-coated supportive material with SnAu alloy on top, (d) Mechanical thinning, and (e) Wet chemical etching.

2.3.2.2 Substrate removal

Conventionally, the initial process developed in the group was to etch down the SI-GaAs substrate from 350 μm to 100 μm by NH_4OH solution with pH of 8.7 [18], then continue the thinning by NH_4OH solution with pH of 8 (slower etching) until a few PQDs are observed. Finally, a more selective (i.e. etching the high concentration AlGaAs layers inserted in the growth and not the GaAs or low aluminum concentrations) citric acid solution (e.g. citric acid powder: H_2O: H_2O_2 = 50 g: 50 ml: 16 ml) is used to open a large area with apex-up PQDs [19]. Etching times were typically 115 minutes in NH_4OH solution and 90 minutes in citric acid solution, respectively. The result as seen in the optical microscope and the profile can be observed in Fig. 2.10 (a) and (d), respectively. A strong inhomogeneous etching pattern is obvious, even up to 40 μm in height across the region where the PQDs appear. This drastically reduces the area with intact PQDs, and sample uniformity. From Fig. 2.10 (b) and (e), one can see, for example, that the situation of inhomogeneous etching could be slightly mitigated, up to 20 μm in height (which is still not good enough for our purposes) by starting the etching in citric acid solution for ~ 33 hours, then terminating the process after 33 minutes in NH_4OH solution with pH of 8.7.

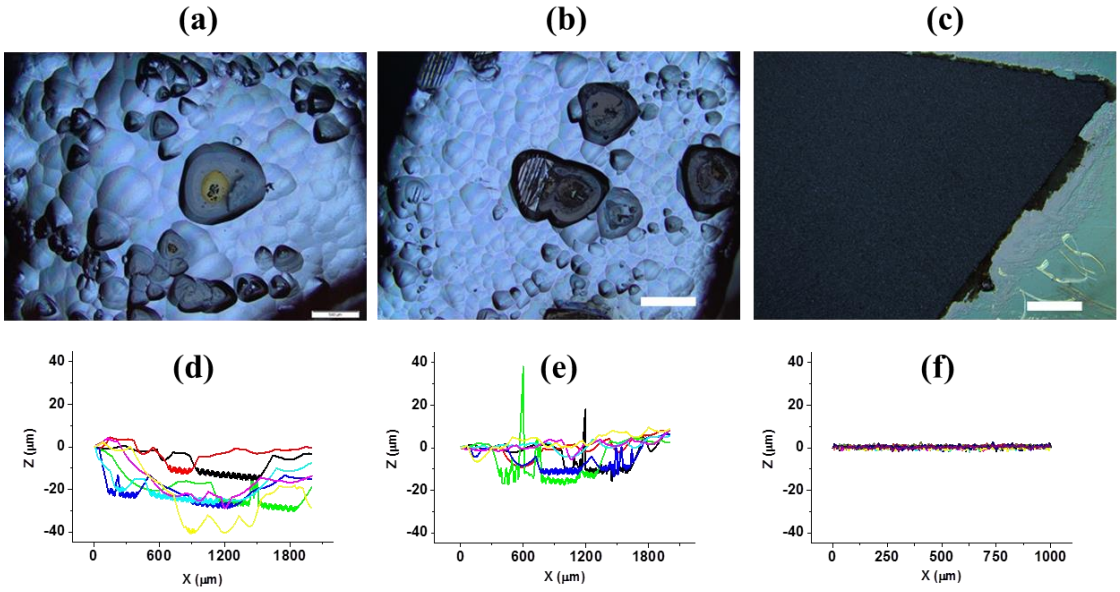

Fig. 2.10: Representative optical microscope images of samples after (a) NH4OH first, then citric acid solution, (b) Citric acid first, then NH4OH solution, and (c) Mechanical thinning. Profiles (d) ~ (f) are corresponding to images (a) ~ (c).

Other than wet chemical etching, the alternative is to thin down the original substrate by mechanical thinning, which is a physical way to avoid the possible anisotropic etching rates among various crystalline facets. The test of mechanical thinning was carried out by a Logitech PM5 lapping and polishing system, combined with aluminum oxide powder, 9 μm in diameter. After thinning for 4.5 minutes, the thickness of the sample is only 30 μm left: optical image and profile are shown in Fig. 2.10 (c) and (f), separately. The peak-to-peak overall roughness was around 1 μm, which is very promising. After the optimization of the thinning parameters, such as the size of the aluminum powder and lapping speed, the samples discussed in the thesis were mainly thinned down to approximately 25 μm left with thinning rate of about 20 μm/min by 1 μm powder. Finally, the back-etching process **was** terminated by NH_4OH wet chemical etching.

2.4 Fabrication light-emitting-diodes with site-controlled PQDs

To realize an electrically-triggered quantum light sources, a light-emitting diodes with site-controlled PQDs is required. Based on our three-dimensional configuration, a device fabrication process was developed, whose flow chart is listed in Fig. 2.11. After the pre-patterning of a semi-insulating GaAs (111)B substrates, a p-i-n structure is grown by MOVPE. As it will be clear subsequently, to prevent electrical shorts, first a layer of Si_3N_4 is deposited onto the as-grown sample. Then we conduct a 3-time tilted-evaporation, rotating by 120^o in-plane each time, of Ti/Au, which acts as a mask metal, so to leave a small aperture of Si_3N_4 at the center of the recess, as in Fig. 2.11 (c). This is then opened by CF_4 plasma etching. Subsequently, a direct Ti/Au layer is evaporated as n-contact (and bonding) metal.

To prepare for back-etching, the sample is bonded onto another Ti/Au-coated GaAs substrate with the assistance of a SnAu ribbon via a reflow soldering process. Apex-up pyramids appear after a subsequent conventional mechanical thinning and chemical etching (NH_4OH:H_2O_2) procedure, as previously described. The contact metal for the diode p-side is, generally, a thin semi-transparent Ti/Au layer (1 nm/ 10 nm), to maintain a good light extraction efficiency. Finally, a wire connection is made simply by using a Kapton coated wire connected to a silver paint bump, which has been dropped onto a large gold

evaporated pad, itself in contact with the thin gold layer covering the pyramids, as shown in Fig. 2.11 (i). The SEM image shown in Fig. 2.12 was captured after step of Fig. 2.11 (d) with green filled circles indicating the position of QD therein which provides a straightforward information on the opening of the Si_3N_4 aperture.

Last, we mention here briefly that non-idealities in the growth process need to be seriously taken into consideration. As shown in Fig. 2.12, the crystallographic orientations of some facets, developing at the shoulders of the pyramidal recess, are not along the usual (111)A direction, as pointed out by the red circles. This is a problem for device performance, representing a possible "short" path for charges, which would obstruct QD emission. The implications of such structure formation will be discussed in the next chapter, and the effects caused by the reduced thicknesses of the laterally growing facets will also be addressed in Chapter 5, especially in respect to the design of the epitaxial structures for electrically-driven devices.

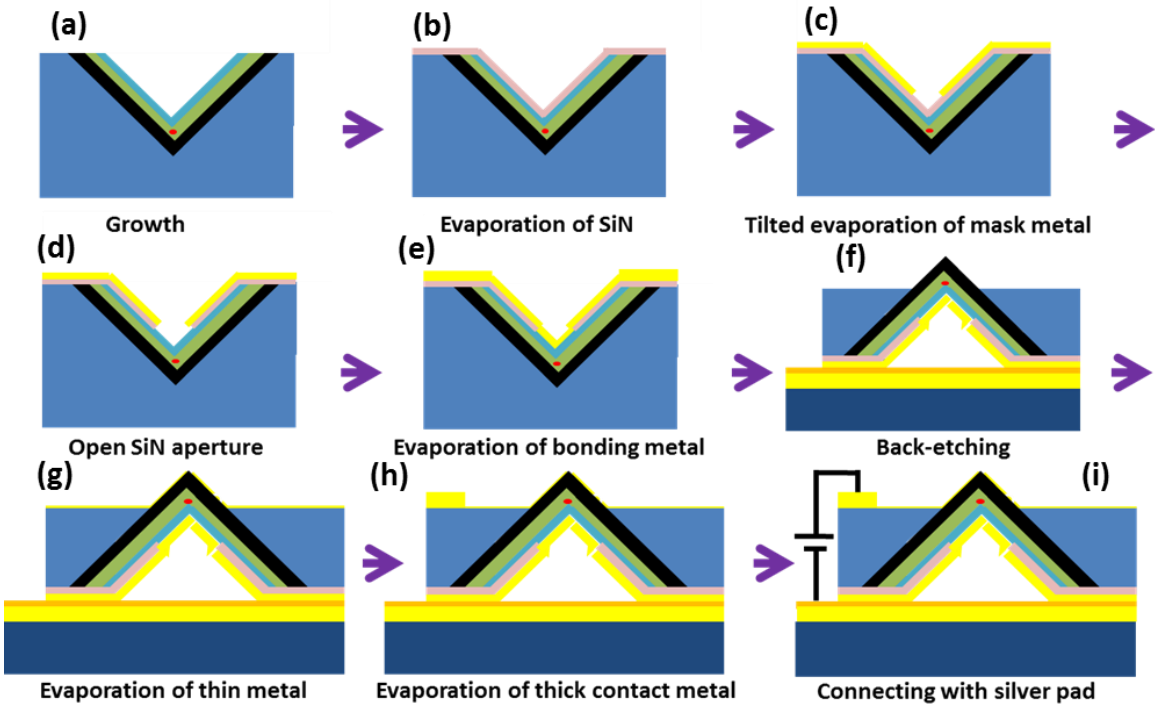

Fig. 2.11: Fabrication process of a light-emitting diode with PQD.

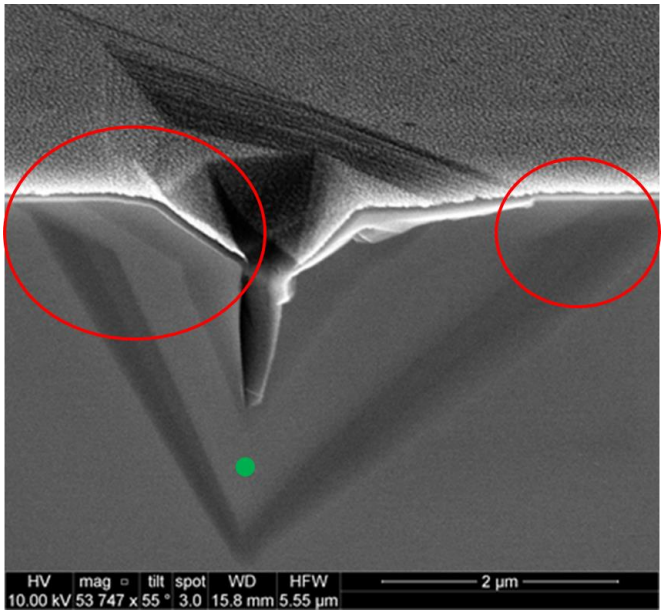

Fig. 2.12 SEM image after opening a Si_3N_4 aperture; unwanted facets (red circles) and position of QD (green filled circle).

Bibliography

[1]: E. Kapon, E. Pelucchi, S. Watanabe, A. Malko, M. H. Baier, K. Leifer, B. Dwir, F. Michelini, M. A. Dupertuis, Physica E (Amsterdam, Neth.), 25 (2004) 288

[2]: V. Dimastrodonato, L. O. Mereni, R. J. Young, and E. Pelucchi, J. Cryst. Growth, 312 (2010) 3057

[3]: L. O. Mereni, V. Dimastrodonato, R. J. Young, and E. Pelucchi, , Appl. Phys. Lett. 94 (2009) 223121.

[4]: E. Pelucchi, V. Dimastrodonato, A. Rudra, K. Leifer, E. Kapon, L. Bethke, P. Zestanakis, and D. D. Vvedensky, Phys. Rev. B 83 (2011) 205409.

[5]: E Pelucchi, S Watanabe, K Leifer, Q Zhu, B Dwir, P De Los Rios and E Kapon, Nano lett., 7 (2007) 1282.

[6]: Stefano T. Moroni, Valeria Dimastrodonato, Tung-Hsun Chung, Gediminas Juska, Agnieszka Gocalinska, Dimitri D. Vvedensky, and Emanuele Pelucchi, J. Appl. Phys., 117 (2015) 164313

[7]: V. Dimastrodonato, E. Pelucchi, and D. D. Vvedensky, Phys. Rev. Lett., 108 (2012) 256102

[8]: V. Dimastrodonato, E. Pelucchi, P. A. Zestanakis, and D. D. Vvedensky, Phys. Rev. B, 87 (2013) 205422

[9]: Q. Zhu , E. Pelucchi , S. Dalessi , K. Leifer , M.-A. Dupertuis , and E. Kapon, Nano Lett., 6 (2006) 1036

[10]: G. Juska, V. Dimastrodonato, L. O. Mereni, T. H. Chung, A. Gocalinska, and E. Pelucchi, B. Van Hattem, M. Ediger, and P. Corfdir, Phys. Rev. B 89 (2014) 205430.

[11]: G. Juska, V. Dimastrodonato, L. O. Mereni, A. Gocalinska, and E. Pelucchi, Nat. Photon. 7 (2013) 527.

[12]: S. Y. Lin, C. C. Tseng, T. H. Chung, W. H. Liao, S. H. Chen, J. I. Chyi, Nanotech., 21 (2010) 295304

[13]: M Bollani, S Bietti, C Frigeri, D Chrastina, K Reyes, P Smereka, J M Millunchick, G M Vanacore, M Burghammer, A Tagliaferri and S Sanguinetti, Nanotechnology, 25 (2014) 205301

[14]: A. Gocalinska, K. Gradkowski, V. Dimastrodonato, L. O. Mereni, G. Juska, G. Huyet, and E. Pelucchi, J. Appl. Phys. 110 (2011) 034319

[15]: A Hartmann, Y Ducommun, K Leifer and E Kapon J. Phys.: Condens. Matter 11 (1999) 5901

[16]: V. Dimastrodonato, Ph.D. thesis, University College Cork, 2011, P. 72.

[17]: R. Trotta, E. Zallo, C. Ortix, P. Atkinson, J. D. Plumhof, J. van den Brink, A. Rastelli, and O. G. Schmidt, Phys. Rev. Lett. 109 (2012) 147401

[18]: Y. Uenishi, H. Tanaka, H. Ukita, IEEE Trans. Electron Devices, 41 (1994) 1775

[19]: J. H. Kim, D. H. Lim, G. M. Yang, J. Vac. Sci. Technol. B, 16 (1998) 558
[20]: V. Dimastrodonato, Ph.D. thesis, University College Cork, 2011, P. 61.

[21]: G. Juska, Ph.D. thesis, University College Cork, 2013, P. 36.

Chapter 3:

Growth model

Introduction

Growth rate anisotropy (GRA) on different crystallographic facets, self-ordering, geometric and compositional configurations along the growth direction are all signatures of epitaxial growth on patterned substrates by metalorganic phase vapor epitaxy (MOVPE). From recent works which appeared in the literature [1-7], the source of GRA is essentially due to decomposition rate anisotropies (DRA) on the different crystallographic facets of the incident fluxes of precursors. As the precursors decompose differently on different crystallographic facets, this translates in an anisotropy of adatom deposition rate, resulting, after diffusion, in what is finally a different growth rate on different facets.

It is worth mentioning quickly that in the early days of patterned substrate MOVPE growth, GRA were mainly attributed to adatom sticking coefficients (e.g., adatoms would stick very differently to (111)A or (100) surfaces). This nevertheless encounters many contradictions with experimental observations. For example: diffusion lengths, expected at a scale of several hundreds of nanometers up to a maximum of a few microns, but which would require the postulation of tens of micrometers adatom (Al, Ga) diffusion lengths to justify the observed phenomenology in V-groove and pyramidal systems [3]. Moreover, speaking of self-ordering formation and alloy segregation, it should be pointed out that early explanations were often given relying on equilibrium thermodynamic ideas such as capillarity and entropy of mixing, i.e. fundamentally non-kinetic processes in the authors' description (even if a deeper analysis of entropy of mixing can indeed show it to be simply equivalent to Fick's law, i.e. a kinetic process) [8,9]. These may have a major role during equilibration processes, but end up not being essential during the epitaxy governing V-grooves and pyramidal systems, which are essentially non-equilibrium, dynamical processes. To capture this, in these years, our group has developed a model, based on a series of reaction-diffusion equations assigned to the various facets, considering the interplay between DRA of group III precursors, their diffusion kinetics, and the subsequent

adatom diffusion as well as incorporation kinetics, to simulate the (Al)GaAs layer growths on either GaAs V-grooves or pyramidal recesses [3-7].

Also in view of the realization of polarization-entangled photons in Ref. [10], the extension of our growth model to the InGaAs system is certainly necessary, being the source of entangled photons from an $In_{0.25}Ga_{0.75}As$ quantum dot (QD) layer. The simulation results will help providing insights into growth dynamics and how it is influenced by growth parameters, such as growth temperature, and, possibly, help in achieving the desired emission properties from our site-controlled QDs. The model and its developments might also aid in giving insights into the control of the fine-structure splitting (FSS) of the intermediate states within the biexciton-exciton-ground decay cascade [11].

In this chapter, the focus will be place on the growth model for InGaAs layer we developed, which covers both V-groove and pyramidal recesses. We also discuss some new findings about the geometry of pyramidal QDs [7].

3.1 Epitaxial structures for the comparison with growth model

To validate the results of the simulation discussed in the following, firstly, we prepared four different samples with only one control variable, growth temperature, for the investigation of the optical properties. These are sample #3A1, #3A2, #3A3, and # 3A4, corresponding to 730, 700, 670, and 640 ^{0}C growth temperature, respectively. A nominal 0.5-nm-thick $In_{0.25}Ga_{0.75}As$ layer was sandwiched by GaAs layers. The thicknesses were 100 nm for the lower cladding and 70 nm for the upper layer. The photoluminescence spectra, measured at 8 K by non-resonant excitation shown in Fig. 3.1 clearly indicate a red-shift trend of the QDs' emissions with increasing growth temperature, along with a less expected blue-shifting peaks corresponding to three lateral quantum wires (LQWRs). Within the range of growth temperatures, approximate 30 meV and 40 meV of energy shifts in the reverse directions are observed for the LQWRs and the QDs, respectively, as we also reported in Ref. [12].

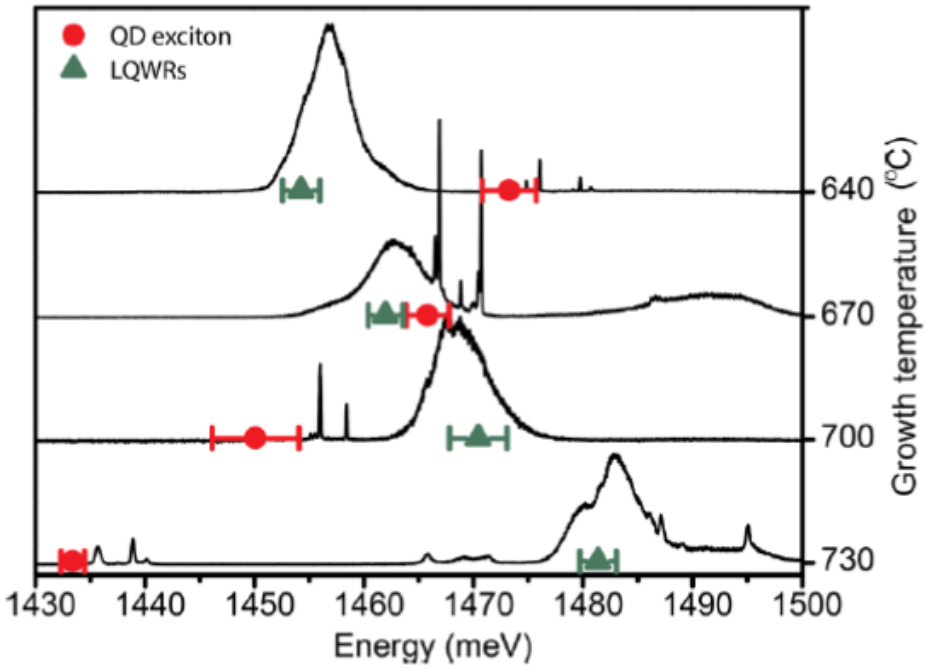

Fig. 3.1: Photoluminescence spectra of four In0.25Ga0.75As pyramidal QD samples with increasing growth temperatures from bottom to top (sample #3A1 to #3A4). The error bars are the statistic results obtained from large number of pyramidal QDs (red circles for QD emissions, and green triangles for LQWRs).

3.2 Theoretical model

The growth process by MOVPE, in a simplified picture, is taken into account separately into three main steps in the growth model, developed in our group with an important contribution from S. Moroni and in collaboration with Prof. Vvedenski from Imperial College London. Precursors, trimethylgallium/aluminum/indium (TMGa/Al/In) for group-III sources and arsine for group-V atomic sources, reach the surface of substrate by diffusion through a boundary layer. Then they diffuse on the semiconductor surface until a portion of them decomposes into atomic constituents of the growth materials (at step edges, for example) while the rest desorb from the surface. Finally, the adatoms diffuse on the surface until incorporation into the growth front. Since the V/III flux ratio applied in all the studied samples were high, ~ 600, the kinetics corresponding to group-V species are neglected and only the kinetics associated to group-III species are considered in our simulation.

For each of the group-III species composing the alloy, the evolution of the free-atom density n_i on each facet (i) can be determined through a reaction-diffusion equation

$$\frac{\partial n_i}{\partial t} = D_i \nabla^2 n_i + F_i - \frac{n_i}{\tau_i}, \tag{3.1}$$

similarly to what was done in previous publications [1-7], where D_i is the adatom diffusion coefficient, F_i is the effective single atom deposition rate, and τ_i is the average adatom lifetime prior to incorporation. Among them, the diffusion coefficient and adatom lifetime are considered in Arrhenius forms: $D_i = D_0 e^{-\beta E_{D,i}}$ and $\tau_i^{-1} = \nu_0 e^{-\beta E_{\tau,i}}$, in which $\beta = 1/k_B T$, k_B is Boltzmann's constant, T is absolute temperature, and $E_{D,i}$ and $E_{\tau,i}$ are energy barriers for diffusion and incorporation processes, respectively. This form emerges directly from reaction-rate theory [21], but the Arrhenius parameters (prefactors and barriers) are treated as adjustable. We used $D_0 = a^2 \nu$, where a is the lattice constant of the surface and $\nu = 10^{15}$ Hz, while $\nu_0 = 4.59$ Hz [6]. The solution of (3.1) across all facets in the structures requires continuity conditions at each facet boundary for the adatom densities $n_i(x)$ and the corresponding diffusion currents, $\mathbf{J}_i(x) = -D_i \nabla n_i(x)$.

In Fig. 3.2 (a) and (b), the schemes, also used in previous publications and applied to our model for V-grooves and pyramidal recesses, are displayed, respectively. Considering the translational invariance of V-grooves along their axes, there are no substantial evolutions expected both in morphology and in composition. Hence, seen in Fig. 3.2 (a), the kinetics within V-grooves are modeled two dimensionally. The symbol $\perp$ indicates the component perpendicular to each assigned facet, while φ and α represent angles for (111)A and (311)A related to (100), respectively. For the model of the growth in pyramidal recesses, a truncated conical template with the circular symmetry about the (111)B direction is applied for simplicity in obtaining analytic solution of (3.1), where θ is the angles between (111)A and basal (111)B.

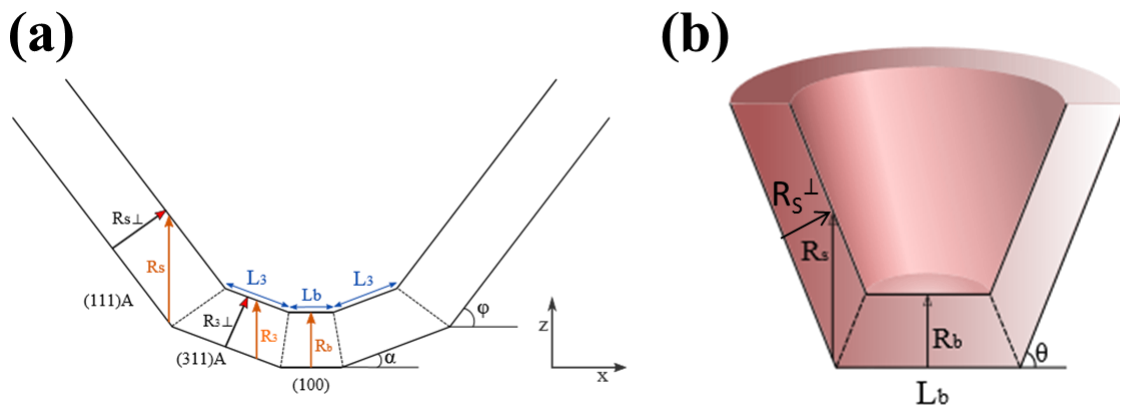

Fig. 3.2: Schemes of models used to our simulations for (a) V-groove and (b) pyramidal recess. The labels b, s, 3 denote the basal facet, the lateral facet, and (311)A facets, respectively.

After the solution to (3.1) is obtained, the growth rate $\boldsymbol{R_i(x)}$ on each facet is calculated as

$$\boldsymbol{R_i(x) = \frac{dz_i}{dt} = \frac{\Omega_0}{\tau_i} n_i(x)}, \tag{3.2}$$

where $\boldsymbol{\Omega_0}$ is the atomic volume. To study the evolution of facet dimensions during growth, the following equations must be coupled to (3.1) for obtaining the lengths of the facets:

$$\boldsymbol{\frac{dL_b}{dt} = 2\left(R_b - \frac{R_3^{\perp}}{\cos\alpha}\right)\cot\alpha}, \tag{3.3}$$

$$\boldsymbol{\frac{dL_3}{dt} = \frac{\frac{R_3^{\perp}}{\cos\alpha} - R_b}{\sin\alpha} + \frac{\cos\varphi}{\sin(\varphi-\alpha)}\left(\frac{R_3^{\perp}}{\cos\alpha} - \frac{R_s^{\perp}}{\cos\varphi}\right)}, \tag{3.4}$$

for V-grooves, or

$$\boldsymbol{\frac{dL_b}{dt} = 2\left(R_b - \frac{R_s^{\perp}}{\cos\theta}\right)\cot\theta}, \tag{3.5}$$

for pyramidal recesses, where $\mathbf{L_i}$ represents the length of the facet. An incremental stationary solution-based method is employed to solve the system by choosing a time-step longer than the adatom concentration relaxation time and considering a starting surface profile. Based on the abovementioned assumptions, we solved (3.1) in the stationary regime (∂ni/∂t = 0), then Ri is calculated, allowing us to study the dimension variation of each facet

at each step. Repeating this procedure allows us to calculate the time-dependent surface profiles but also the alloy contents of deposited layers for each facet. Once the GRA and diffusion current are balanced, which requires the growth time over a certain duration, the self-limiting profile growth will be accomplished, resulting in a constant basal width and a common vertical growth rates.

3.3 Determination of kinetic parameters

Before applying our model to simulate the configurations of either QDs or LQWRs, noticing that the latter nanostructures share the same crystallographic facets as V-grooves, the free kinetic parameters of indium and gallium must be determined. The parameter set for gallium can be obtained from previous work in (Al)GaAs V-grooves [6]. The task to determine the kinetic parameters, i.e., the energy barriers for the diffusion and incorporation processes and effective adatom diffusion fluxes, for Indium, on the other hand, was addressed by iterative fitting existing experimental data as from Ref. [13], until the agreement was reached for both the morphological and compositional evolution of the InGaAs layer. Indeed the fact itself that such fitting was possible and successful, is an indication of the overall validity of the model applied to the InGaAs systems.

From Ref. [13], the transmission electron microscopy (TEM) image, reported in Fig. 3.3, of a layer of nominal $In_{0.12}Ga_{0.88}As$ provided the dimensions and orientations of facets constituting the initial profile. Based on these, we modeled the transient evolution of a 45-nm-thick $In_{0.12}Ga_{0.88}As$ grown at 530 ^{0}C, whose results are sketched in Fig. 3.3. The chosen growth temperature in the simulation was derived under the assumption that we share a similar temperature difference between thermocouple reading and real one with the Lausanne group reactor discussed in Ref [13], being the two reactors involved are identical.

In our simulations, the parameters in Table 3.1 are used. The indium segregation level (i.e. the excess In segregating at the centre of the V-groove wire, as visible in Fig. 3.3 and reported in the cited manuscripts) deriving from our simulations is about 20%, with a nominal relative indium deposition flux of 12 %. This is in very good agreement with the experimental data, 20±2 %, at the bottom of the groove, which was measured by electron energy-loss spectroscopy [7,13]. In the discussed manuscript 12±2 % of indium

concentration on the sidewalls of V-groove was observed. The significant difference in concentration with the case of the V-groove bottom part should be ascribed to a larger diffusion length of indium adatoms compared to the values for gallium.

Indeed, from Table 3.1, one can observe that, compared to gallium, indium is a more mobile species, which is a prerequisite for reproducing the strong indium segregation at the bottom of V-grooves. This is not unexpected in many ways: from the relevant literature, *ab initio* calculations of diffusion of gallium and indium on GaAs (001) surface suggest there is difference in the cation-As bond strength between InAs and GaAs, mostly appearing as differences in ionic radii [14,15]. As a consequence, the potential landscape for indium is less corrugated than for gallium adatoms.

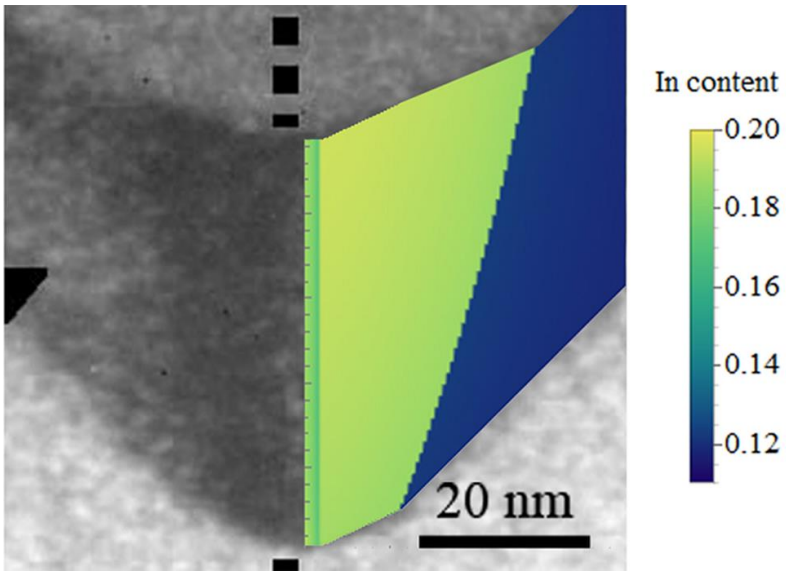

Fig. 3.3: TEM image of a layer of In0.12Ga0.88As with nominal thickness of 40 nm and simulation results of indium concentration distribution with color scale bar at the right-hand side.

Another consequence on the various facets of long indium diffusion lengths is the reduction of relevance of the effects of DRA for the different facets. Simulation results are indeed rather insensitive to changes in the ratios of indium effective deposition fluxes. For instance, increasing the ratio of indium effective deposition rate (*r* in Table 3.1) from 0.5 to 2 only results in 1 % of indium concentration change, and less than 1 nm in the change of facets dimensions.

Facet	Indium				Gallium			
	E_D (eV)	E_τ (eV)	λ (nm)	r	E_D (eV)	E_τ (eV)	λ (nm)	r
(100)	1.25	0.100	100.7	1.00	1.80	0.114	2.07	1.00
(311)A	1.15	0.103	212.5	1.01	1.40	0.128	41.58	1.01
(111)A	1.12	0.167	420.1	1.01	1.35	0.159	74.79	1.10

Table 3.1: Two sets of parameters used in simulations for indium and gallium, respectively, where the diffusion lengths $\boldsymbol{\lambda}$ are calculated ($\boldsymbol{\lambda = \sqrt{\tau D}}$) and r indicates the ratio of the adatom deposition rate on each facet over (100) facet.

3.4 Applying the model to growth inside pyramidal recess

To apply the model to the growth of LQWRs and pyramidal QD within a pyramidal recess, we had to make some assumptions. First, the two systems studied here are to be considered independent since the region simulated along the LQWRs is remote enough from the basal facet (LQWRs are microns long). Indeed, this is feasible also because the dimensions of the pyramidal edge, which are larger in length (2~3 μm) than the base facet (30~60 nm). Although there are several layers grown before the deposition of InGaAs QD layer, we only consider in the simulation the last GaAs barrier layer and neglected the effects coming from the other underlying layers based on the assumption that 100-nm-thick GaAs has reached a self-limiting profile [5]. Possible discrepancies shown later between the simulation results and the experimental findings should not be attributed to this assumptions, but to other experimental variables as will be shown.

Following the modeling process as described in Ref. [6], we calculated LQWRs obtained with a growth of a 2-nm-thick $In_{0.25}Ga_{0.75}As$ layer upon the GaAs self-limiting profile for four different growth temperatures. We used the parameters set in Table 3.1. The value of "2 nm" for our simulation is four times larger than the nominal thickness described in the epitaxial structures. It is worth stressing again the fact that, in our growth regime, the vertical growth rate at the basal facet is also always higher than the one perpendicular to the sidewalls, because of the involved geometry, and both are higher than nominal ones. Two

nanometers should be considered a typical expected value for the corresponding nominal 0.5 nm [16].

Modeling results are shown in Fig. 3.4 (a) displayed as average values along the 2 nm vertical dimension. During the 2 nm "deposition", no significant change is observed both in composition and lateral dimension during the simulation. Inspecting the simulation data in Fig 3.4, a trend of increasing indium concentration at the bottom of the LQWRs with reduced growth temperature is clear, i.e. a stronger indium segregation is seen. In terms of the energy gap, the change of growth temperature from 640 ^{0}C to 730 ^{0}C leads to an increment of 11.7 meV at 8 K, if quantum-confinement effects are neglected. This tendency is consistent with the experimental data, shown in Fig. 3.1, although the experimental value is indeed larger (~ 30 meV).

It should also be said that to make an accurate prediction of the emission energy-dependence (for the nanostructures grown) as a function of the growth temperature, we would need to take into account the quantum confinement effects associated with the various lateral dimensions. In the case of LQWRs, the total lateral dimensions ($\boldsymbol{L_b^* = L_b + 2L_3}$) range from 108 to 175 nm depending on the growth temperature and shown in Fig. 3.4 (a). The scales are far larger than the Bohr radius of the exciton, estimated as approximate 20 ~ 30 nm, which implies that only the vertical dimensions should be relevant for including quantum confinement effect.

To confirm the role of temperature-dependent segregation for the observed red-shift, we have conducted an iterative procedure to obtain a second set of kinetic parameters for indium and gallium, as listed in Table 3.2. This set of parameters result in a more pronounced shift of the emission energies with changing temperatures without deviating too much from the parameters in Table 3.1. Based on the parameters in Table 3.2, the simulation results are summarized in Fig. 3.4, with an energy gap decrease of 21.1 meV. Even though this result is not derived directly from the fitting of experimental data, it still suggests the temperature-dependent indium segregation as a relevant possible explanation for the observed redshift. A further discussion of the discrepancies between the experimental data and simulation results will be also presented in following sections.

Basing on the process followed in the modeling of LQWRs, we then needed to extend the model to the growth of InGaAs QDs, with a three-dimensional truncated conical configuration as depicted in Fig. 3.2 (b). This could allow us to evaluate with the effects of temperature-dependent segregation and base dimensions in relation to the blueshift observed in the discussed photoluminescence spectra, as seen in Fig. 3.1. In Ref. [12], this phenomenon is attributed tentatively to a change in self-limited profiles, and not to indium segregation. The kinetic parameters on (111)A facet were chosen the same as in the model of the LQWRs. However, there are no detailed experimental data available for the case of (111)B basal facet to fit the growth of $In_{0.25}Ga_{0.75}As$ on GaAs. Then, according to the suggestion from previous studies about pyramidal QD optical properties [16], we chose the parameters that resulted in a 4% indium segregation, as listed in Table 3.3 at a given growth temperature at 700 ^{0}C. Based on this assumption, the simulation results of indium relative concentration and base dimensions ($\boldsymbol{L_b}$) on the base facet as a function of growth temperature are shown in Fig. 3.5 (a) and (b), corresponding to the parameter set in Table 3.3 and Table 3.2, respectively. From the simulation data, there is no significant increase in the indium relative concentration on the basal facet as the growth temperature is increased, which is rather different from the observations in the system of LQWRs. However, the simulated lateral dimensions of the QD are comparable to the Bohr radius of the exciton in this case, resulting in a non-trivial quantum-confinement influence on the emission energies. According to the observed trend in Fig. 3.5, the decrease in growth temperature causes reduced lateral dimensions of the QD, leading to a blueshift in the spectra, which is consistent with the experimental data [12].

In spite of the consistent qualitative tendency achieved, we stress out that more theoretical work is required to obtain the complete picture of this effect inside pyramidal recesses, especially considering the particular geometry of the QD.

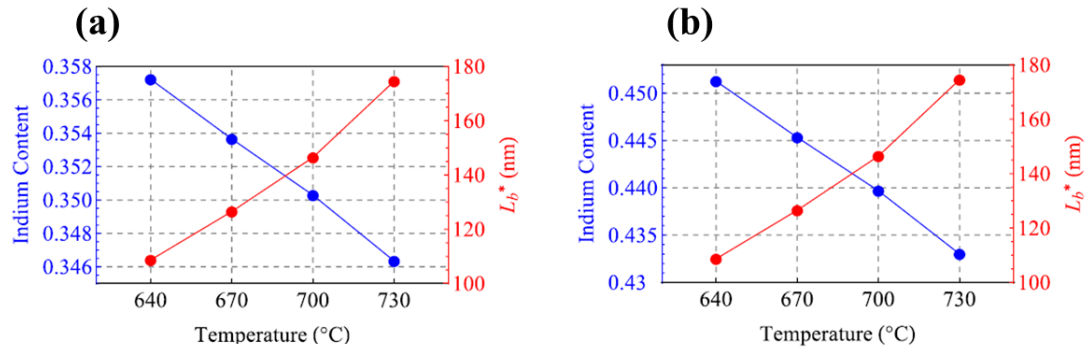

Fig. 3.4: The simulated results of lateral dimensions ($\mathbf{L_b^* = L_b + 2L_3}$) and indium contents of corresponding growth temperatures by using parameter set of (a) Table 3.1 and (b) Table 3.2, respectively.

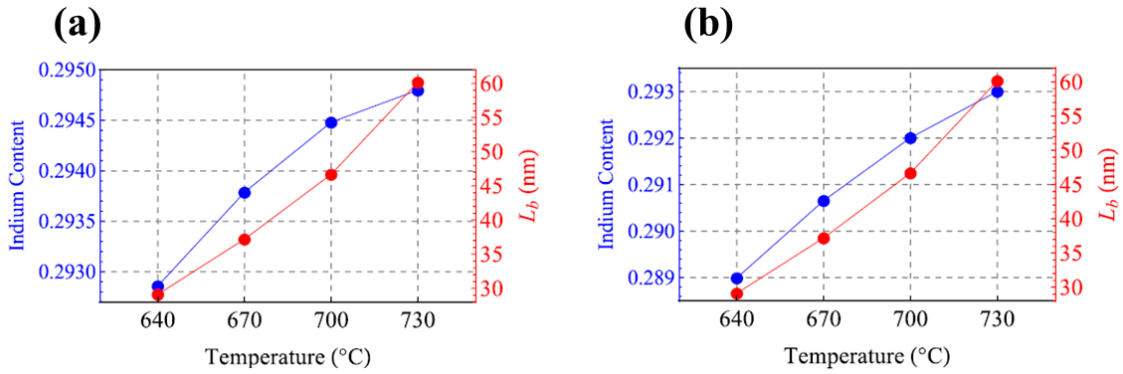

Fig. 3.5: Temperature dependence of the length of the base facet and of In relative content on it resulting from the simulations of the QD growth on the bottom of a pyramidal recess; (a) shows the results when the set of parameters number 1 is employed, while (b) is the result of the simulations run using the set of parameters number 2.

Facet	Indium			Ga		
	E_D (eV)	E_τ (eV)	r	E_D (eV)	E_τ (eV)	r
(100)	1.27	0.090	1.00	1.85	0.122	1.00
(311)A	1.22	0.095	1.01	1.55	0.141	1.01
(111)A	1.20	0.187	1.01	1.25	0.159	1.10

Table 3.2: Modeling parameters for indium and gallium on each facet, where ED and Eτ are energy barriers for diffusion and incorporation respectively. Value r shows the ratio of deposition rate of each facet over (100) facet.

Optimized for set	Indium				Ga			
	E_D (eV)	E_τ (eV)	ν_0 (s^{-1})	r	E_D (eV)	E_τ (eV)	ν_0 (s^{-1})	r
1	1.45	0.059	5.81	1.01	1.52	0.031	4.13	1.10
2	1.50	0.066	5.71	1.01	1.55	0.020	4.00	1.10

Table 3.3: Kinetic parameters on (111)B facet optimized for parameter set 1 (Table 3.1) and 2 (Table 3.2)

3.5 Real morphology inside pyramidal recesses

From the simulation results discussed in the previous sections, there are still some discrepancies in the *quantitative* analysis between experimental observations and simulation predictions. In this section, we would like to gain some insights on these aspects by means of cross-sectional atomic force microscopy (CS-AFM) and scanning electron microscopy (SEM). To conduct this work, we prepared some other samples, #3B1 and #3B2, whose structures are the same as the previously discussed growth-temperature-dependent samples, but terminated just before the growth of the $In_{0.25}Ga_{0.75}As$ QD layers. This structure was designed to study the recess morphology right before the growth of the QD layers. In addition, sample #3B1 was capped with a 30 nm $Al_{0.55}Ga_{0.45}As$ layer acting

as a marker. This is to provide a better height contrast, coming from the different degrees of oxidation, in the CS-AFM images. Growth temperatures were 730 ^{0}C and 640 ^{0}C for sample #3B1 and #3B2, respectively. To obtain the cross-sectional microscopy images, we cleaved the samples along the (110) direction. Morphological information of both LQWRs and QDs can be revealed by choosing the points of cleavage, as discussed more clearly in the subsequent text.

The CS-AFM image of sample #3B1, cleaved for the study of LQWRs, is displayed in Fig. 3.6 and shows an evolution in crystallographic orientation following the growth of different layers. Indeed, the final GaAs layer evolves in a steep *vicinal* facet instead of staying a pure (111)A facet. Even though there is still no conclusive explanation for this phenomenon, a similar evolution of angles between sidewall and base facet is also observed in (Al)GaAs/GaAs V-grooves [6]. From Fig. 3.6, the angles between vicinal facet (111)A and base facet (111)B is ~77^0, and, according to basic trigonometry, the calculated angle between the lateral (111)A facet and the LQWR (100) base facet is ~33^0. This is different from the case of V-groove, whose angle is ~45^0. This evolution to steeper angles, could be one of reason leading to discrepancy between experiment and theory (the latter developed in the ideal condition of a pure (111)A). The kinetic parameters for such vicinal facet could need to be optimized to revise the simplified profile assumed in the initial model.

Even though the resolution for SEM is less accurate compared to AFM (up to two orders of magnitude in our case), its flexibility allows us to, relevantly, confirm to which position of a pyramidal recess the cleaved line is passing. This was by means of capturing top-viewed images, leaving markers first and then snapshotting the tilted-view ones.

From the top-viewed images of sample #3B2, seen in Fig. 3.7 (a), one can observe that each of three lateral facets of a pyramid is composed of two vicinal facets, leading to a somehow hexagonal inward-shaped top outline. However, this inward shape is not fixed, but growth-temperature-dependent. This can be observed in Fig. 3.8, in which, (a) ~ (d) are corresponding to sample #3A1, #3A2, #3A3, and #3A4, respectively. It is clear that the outward-shaped outline will gradually evolve to an inward-shaped one, from a high growth temperature (730 0C, (a)) to a lower one (640 0C, (d)). From another top-viewed SEM

image, shown in Fig. 3.7 (c), we can observe that the color of the regions corresponding to the edges and bottom of the pyramid recess is darker compared to the rest of area, indicating they are located at a deeper position. Notably, the center of the recess is found to be the deepest region with a quasi-circular outline, whose diameter is smaller than the lateral broadening of the wires. This finding suggests that the bottom faceting of a pyramid recess is not simply connected to the three conjoint LQWRs but shows a more complicated facet evolution connecting the base to the LQWRs. This can be proved by inspecting the tilted-view SEM images in Fig. 3.7 (a), in which line A and B pass through the center of the pyramidal recess and the LQWRs, respectively.

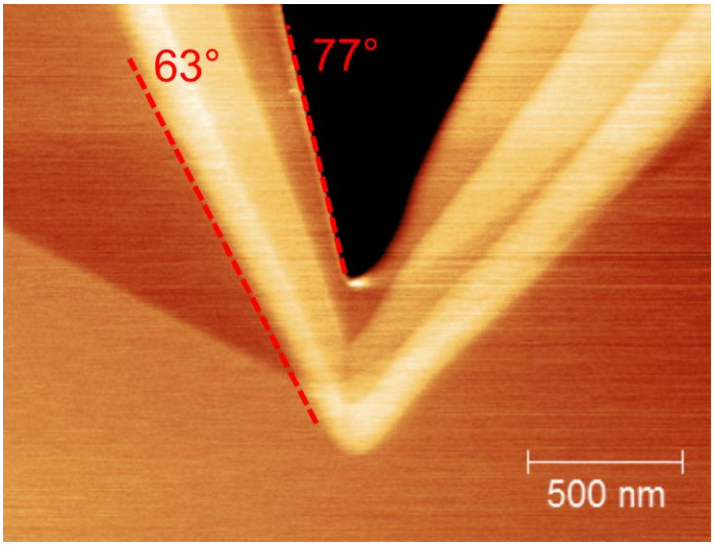

Fig. 3.6: CS-AFM image of sample #3B1, where the point of cleavage was chosen off center of pyramidal recess.

Combing the observation from the SEM images and the assumption of sharing some similarity for the edge faceting to the case of V-grooves, a qualitative graphical three-dimensional model of the pyramidal recess can be built and shown in Fig. 3.7 (b). The modeling results also include an evolution of complicated faceting, compared to the previously-assumed configuration, in the bottom of recess, which are compatible with the cross-sectional morphology observed experimentally. Interestingly, Monte Carlo growth simulation, recently reported in Ref. 17, suggested a similar behavior faceting on the bottom of recess, grown at low temperature and in small-pitch pyramidal recesses, which is consistent with our experimental findings.

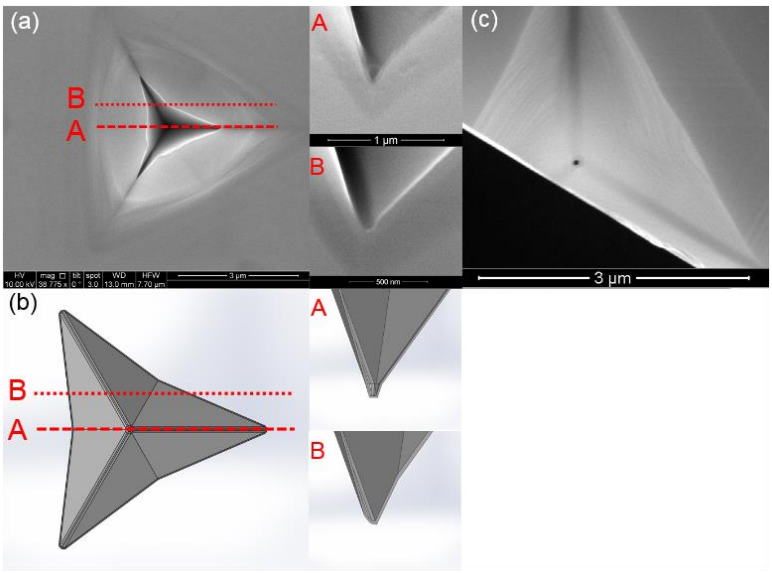

Fig. 3.7: Top-viewed images of sample #3B2 of (a) a full pyramidal recess and of a cleaved one, where the two tilted-view SEM images in the right-hand side of (a) reveal the cross-sectional morphologies of cleavage through the center, cutting through line A (upper image), and through one of the LQWRs, cutting through line B (lower image). (b) Data from the reconstructed three-dimensional graphical model in top view and tilted views with cutting corresponding to line A and B.

One could wonder why ours is the first report of such complex base faceting, and why no previous report addressed this. The answer could be that special care must be taken in searching for the exact pyramids which are cut right through the center during the image-capturing either in tilted-viewed or CS configuration. From our experience, the probability to have a proper cleavage through the central regions of pyramids is one out of several tens of cleaved pyramids. In a sense, this is difficult to do by SEM , not to mention by AFM.

Since this steeper faceting at the bottom recess was not reported in the past, we needed to prove that this was not a "special" case linked to certain "special" conditions. To confirm our findings, we prepared two batches of samples at the same growth temperature, 730 0C: for the first batch, samples #3C1, #3C2, and #3C3, the structures were composed of four 100-nm-thick Al0.3Ga0.7As layers with three GaAs marker layers inserted into

every two of them; for the second series, samples #3D1, #3D2, and #3D3, the nominal thicknesses of GaAs and Al0.3Ga0.7As layers were swapped. In both batches, number 1, 2, and 3 correspond to pitch lengths of 5, 7.5, and 10 μm, respectively. In all the tilted-view SEM images of these six samples, shown in Fig. 3.9, a steeper faceting at the centers of pyramidal recesses is consistently observed.

Unfortunately, apart from the obvious requirement to match with steep vicinal facets, the geometrical differences between the small (111)B base and the larger LQWRs profile, we cannot provide a more concrete modelling of this phenomenon. We have also no systematic values to describe the tendency of the angles between vicinal (111)A facets and basal (111)B facets as a function of material/thickness deposited or pitches used due to the limits of our experimental setups. Indeed, more TEM studies would be required to clarify the exact morphological faceting and possibly to link it with the observed optical properties.

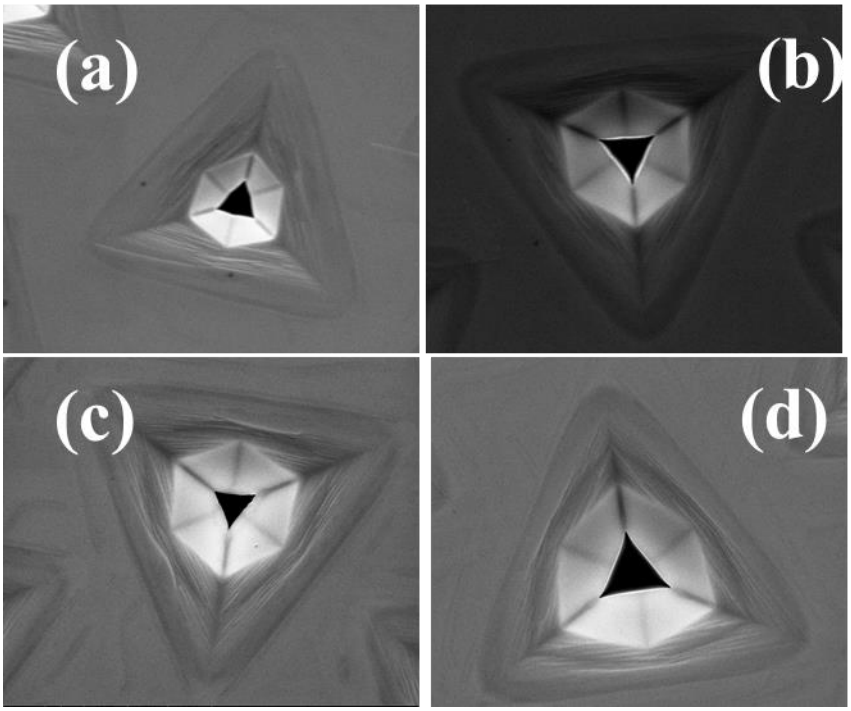

Fig. 3.8: Top-viewed SEM images of (a) sample #3A1 (730 ^{0}C), (b) #3A2 (700 ^{0}C), (c) #3A3 (670 ^{0}C), and (d) #3A4 (640 ^{0}C)

Nevertheless, these SEM images also provide us some useful information as we design new epitaxial structures. For instance, the steeper facets at the bottoms of the recesses (at the end of the growth) will be a potential risk of failure when depositing an

electrical contact layer, for an electrically-pumped device, due to the possibility of electrical discontinuity if trivial evaporation procedures are used. In this case, the guideline would be to adjust (diminish) the total (nominal) thickness of the growth so to obtain as large as possible opening of the pyramidal recesses, paying attention not to push towards a too thin structure which would risk to reduce QD emission intensity due to interactions with surface states, for example.

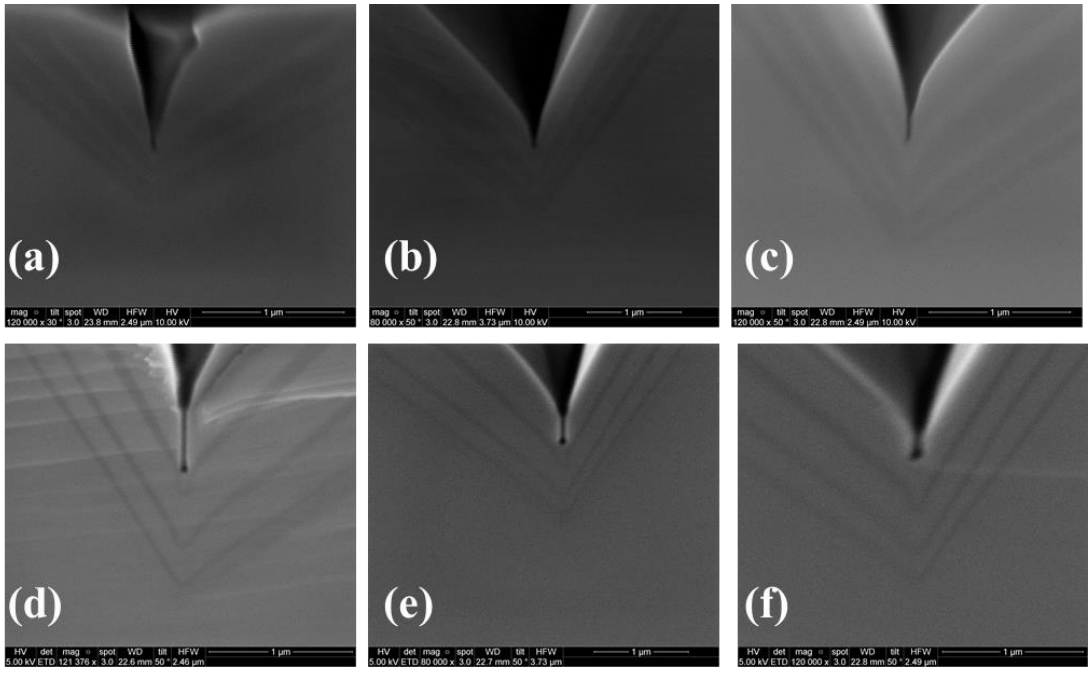

Fig. 3.9: Tilted-viewed SEM images of sample (a) #3C1, (b) #3C2, (c) #3C3, (d) #3D1, (e) #3D2, and (f) #3D3.

3.6 One last note on the role of capillarity effects

In the past, to interpret the morphology evolution of the growth on corrugated substrates, the concept of capillarity was often introduced, associated to a growth related minimization of surface energy [19,20]. Specifically, the so-called capillarity, generally referred as "chemical potential-induced capillarity," has always being modeled through adatom surface currents, raised by chemical potential difference over various facets. These currents would act as "flattening" elements. A reduced corrugation would correspond to a reduced surface energy; i.e. the dot formation would be induced by a process of surface energy minimization.

However, we would like to point out that in the model developed in our group capillarity is not considered, nor it is needed to achieve a correct simulation of the growth process. Indeed, in Ref. [18], the author investigated which effects were dominating in achieving a self-limited profile, reporting that, if capillarity was explicitly added in the calculations, there was no significant change in the output of the simulations, neither in vertical growth rates nor in lateral dimension of the basal facet when AlGaAs/GaAs V-grooves were considered, even though a spread of three orders of magnitude of the chemical potential was tested. A possible ascription is that the effects caused by the chemical potential have been comprised (concealed) by the kinetic parameters in the series of reaction-diffusion equations (especially the terms involving diffusion energy barriers). Alternatively, that capillarity is not a relevant ingredient in the formation process, and the dot formation and other segregation effects (e.g. higher vertical growth rate at the bottom facet) are simply a consequence of surface diffusion and facet dependent adatom sticking coefficients.

Our model has been applied with successful predictions for the (Al)GaAs/GaAs growth dynamics for both V-grooves and pyramidal recesses [4-7,18]. Summarizing for the InGaAs/GaAs V-grooves in this chapter [7], the reproducible predicted alloy segregation and GRA in the simulation results justify the consideration that a chemical potential-induced capillarity can likely be neglected during the simulation.

3.7 Summary

In summary, the segregating mechanism of indium elements on both $In_{0.25}Ga_{0.75}As$ V-grooved quantum wires and pyramidal quantum dots has been quantitatively justified by the previously-developed growth model [1-7]. From simulation results, the evolution of growth temperature-dependent emission energy, which is a quantum dot redshifting as well as a lateral quantum wires blueshifting, is consistent with the reported experimental results. Finally, a new faceting at the center of pyramidal recess was observed.

Bibliography

[1]: E. Kapon, E. Pelucchi, S. Watanabe, A. Malko, M. H. Baier, K. Leifer, B. Dwir, F. Michelini, and M. A. Dupertuis, Physica E (Amsterdam, Neth.), 25 (2004) 288

[2]: Q. Zhu , E. Pelucchi , S. Dalessi , K. Leifer , M.-A. Dupertuis , and E. Kapon, Nano Lett., 6 (2006) 1036

[3]: E. Pelucchi, V. Dimastrodonato, A. Rudra, K. Leifer, E. Kapon, L. Bethke, P. Zestanakis, and D. D. Vvedensky, Phys. Rev. B 83 (2011) 205409

[4]: V. Dimastrodonato, E. Pelucchi, and D. D. Vvedensky, Phys. Rev. Lett., 108 (2012) 256102

[5]: V. Dimastrodonato, E. Pelucchi, P. A. Zestanakis, and D. D. Vvedensky, Phys. Rev. B, 87 (2013) 205422

[6]: V. Dimastrodonato, E. Pelucchi, P. A. Zestanakis, and D. D. Vvedensky, Appl. Phys. Lett., 103 (2013) 042103

[7]: S. T. Moroni, V. Dimastrodonato, T-H Chung, G. Juska, A. Gocalinska, D. D. Vvedensky, and E. Pelucchi, J. Appl. Phys., 117 (2015) 164313

[8]: G. Biasiol, and E. Kapon, Phys. Rev. Lett., 81 (1998) 2962

[9]: G. Biasiol, A. Gustafsson, K. Leifer, and E. Kapon, Phys. Rev. B, 65 (2002) 205306

[10]: G. Juska, V. Dimastrodonato, L. O. Mereni, A. Gocalinska, and E. Pelucchi, Nat. Photon. 7 (2013) 527.

[11]: G. Juska, E. Murray V. Dimastrodonato, T-H Chung, S. T. Moroni, A. Gocalinska, and E. Pelucchi, J. Appl. Phys., 117 (2015) 134302

[12]: G. Juska, V. Dimastrodonato, L. O. Mereni, T-H Chung, A. Gocalinska, and E. Pelucchi, Phys. Rev. B, 89 (2014) 205430

[13]: F. Lelarge, C. Constantin, K. Leifer, A. Condo, V. Lakovlev, E. Martinet, A. Rudra, and E. Kapon, Appl. Phys. Lett., 75 (1999) 3300

[14]: E. Penev, P. Kratzer, and M. Scheffler, Phys. Rev. B, 64 (2001) 085401

[15]: J. G. LePage, A. Alouani, D. L. Dorsey, J. W. Wilkins, P. E. Blöchl, Phys. Rev. B, 58 (1998) 1499

[16]: S. B. Healy, R. J. Young, L. O. Mereni, V. Dimastrodonato, E. Pelucchi, and E. O'Reilly, Physica E, 42 (2010) 2761

[17]: A. Surrente, Ph.D. thesis, École polytechnique fédérale de Lausanne EPFL, 2013

[18]: V. V. Dimastrodonato, Ph.D. thesis, University College Cork UCC, 2012

[19]: E. Kapon, D. M. Huang, and R. Bhat, Phys. Rev. Lett., 63 (1989) 430

[20]: W. W. Mullins, J. Appl. Phys., 28 (1957) 333.

[21]: P. Hänggi, P. Talkner, and M. Borkovec, Rev. Mod. Phys., 62 (1990) 251.

Chapter 4:

Neutralization of negative trions

Introduction

Non-resonantly optically-driven, our group has demonstrated up to 15 % yield of polarization-entangled photon emitters among a selected area [1] in 2013. After carefully analyzing the reasons why some emitters failed to deliver photon pairs with good quantum correlations, they can ascribed into three principle causes: (a) existence of a large fine-structure splitting (FSS); (b) poor back-etching process; (c) dominant negative trion intensities among the excitonic transitions. The first issue mainly resulted from indium random segregation, and can be dealt by introducing external physical controls to restore it (see Chapter 1.5.2) or optimize growth parameters, such as QD layer thicknesses and others, e.g. discussion in Chapter 6. The second one has been already been drastically improved by ~ 3 times at least in the "good areas," i.e. pyramidal quantum dots (PQDs) within such areas remained intact after the back-etching step, see Chapter 2.3.2, and will be discussed further at the end of this chapter.

The last issue can be understood by a representative photoluminescence (PL) spectrum, shown in Fig. 4.1, from a GaAs/$In_{0.25}Ga_{0.75}As$/GaAs sample, showing spectra of a negatively charged single-QD and a positively charged one. The typical excitonic pattern includes exciton (X), binding biexciton (XX), negative trion (X-), and positive trion (X+) peaks, in which, typically, X+ appear at the high-energy side while X- is detected with lower energy relative to X [1,2]. Before taking effective polarization-dependent PL measurements, the pre-selection rule for good dots filters out those dots which are negative trion-dominating, as excitation power has to be increased substantially to allow correlation measurements, mainly due to an insufficient intensity of X with strong detriment to the quality of the final result.

Given the doping type of substrate, semi-insulating, and the back-etching of the samples, two possible origins for this excess electron density are speculated: excess

electron concentration from GaAs acceptor levels, due to background doping in metalorganic vapor phase epitaxy (MOVPE), which are excited by non-resonant pumping [4,5] or defect-induced hole trap states, resulting from back-etching. In this chapter, we describe separately three methods to address the charging issue: (a) charge neutralization by introduction of dual-wavelength excitation; (b) excess electron absorption by a non-coupled sacrificial QD layer(s) on the epitaxy side; (c) improvement of etching selectivity by insertion of AlAs etch-stop layer addressing the aspect of processing induced features.

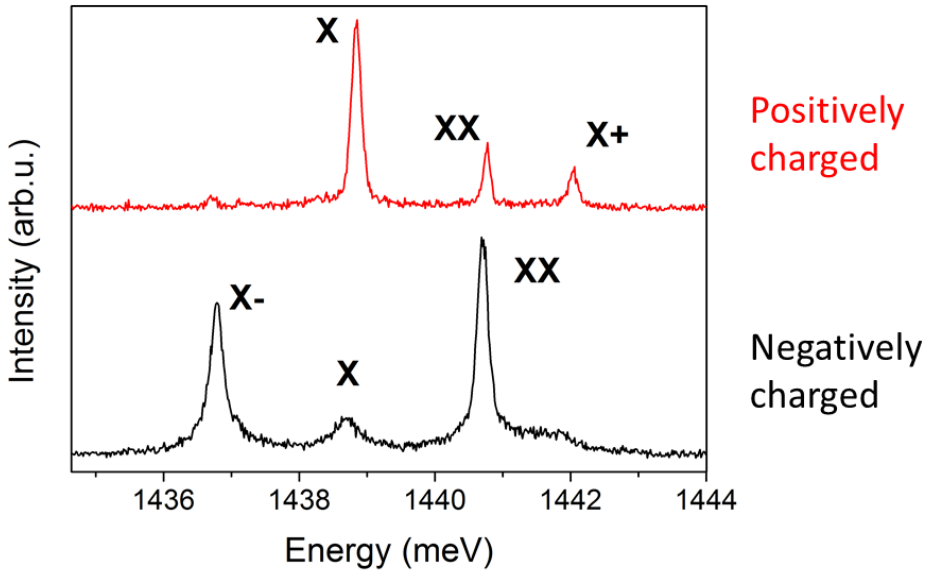

Fig. 4.1: Representative spectra of positively-charged (upper) and negatively-charged QDs (lower).

4.1 Dual-wavelength excitation

As mentioned previously, under non-resonant optical pumping, the ensemble of free carriers also includes the ones coming from the confining materials. From the literature [3], non-resonant pumping could excite electrons from GaAs acceptor levels to the conduction band, in which the created holes will tend to be trapped at the acceptor levels, while the generated electrons will be fed efficiently into a QD nearby, resulting in an excess electron density in the dot. In this sense, an idea to neutralize a QD is that of introducing a second pumping laser, whose energy is able to generate an excess hole concentration via transitions from the valence band to the GaAs deep levels, which would eventually neutralize or even

positively populate the dot. This technique is the so-called dual-wavelength excitation (QWE) scheme [3].

To test this idea in our PQD system, a "conventional" optical-pumping sample was grown, as introduced in Chapter 2.2.4, composed of 0.85 nm $In_{0.25}Ga_{0.75}As$:N QD layer sandwiched by GaAs layers. For micro-photoluminescence (μ-PL) measurements, the sample was cooled down to 8 K in a closed-cycle helium cryostat, and the emission was collected in confocal configuration, with a pump laser (1590 meV) and a charge-tuning laser (1180 meV).

In Fig. 4.2 (c), as the charge-tuning laser was switched off, power-dependent PL was conducted. One can see a typical excitonic pattern: X- is dominant at weak excitation levels, and, as the pump laser power is increased, the intensity of X is enhanced inefficiently and XX starts to dominate the spectrum. This power-dependent behavior indicates that before a neutral XX decays with an X emitted, it will be charged with an additional electron efficiently, resulting in XX and X- strongly dominating at high excitation level. This decay cascade events are practically useless for emitting entangled photon pairs, so, in general, a group of QDs with such behavior will be filtered out for that purpose. However, with pump laser power fixed, the intensities of X-, X, and X+ evolved with increasing power of the charge-tuning laser, in which X- started to be suppressed at the beginning, then X dominated at middle level, finally X+ took over at even higher excitation levels, see Fig. 4.2 (a). In addition, a reduced linewidth of X was obtained along with increasing power of the charge-tuning laser until the brightness of X- was fully suppressed. This resulted from the electric field in the vicinity of the QD as being "neutralized", leading to reduced spectral wandering [6]. In this case, the perturbation to the energy level distribution, caused by the existence of the charged point defects, was mitigated, which is also consistent with the around 0.1 meV redshift observed in the X peak as a function of dominating excitonic charged transition [7-9]. Hence, introducing such a charge-tuning laser provided an efficient "knob" to tune the charging type of our QDs.

Moreover, such a sample contains highly symmetric QDs, which is the same as for the one reported for emitting entangled photon pairs with high yield [1]. So, after tuning the

QD into nearly neutralization, second-order correlation spectra in linear, diagonal, and circular bases were conducted (see chapter 6 for details on the procedure), and the calculated fidelity (f) to the expected maximally entangled state was 0.6±0.025, qualified as polarization-entangled emitter, see in Fig. 4.2 (b).

To further test the power of DWE, 22 QDs were studied in a region of this sample, whose image is shown in Fig. 4.3 (b). The red crosses within the image indicate the emissions were too poor to conduct proper measurements, i.e. the QDs could have been damaged during growth or more likely after post-growth processing. The top (red) spectra are taken when QDs are excited only by a single wavelength excitation (1590 meV). The bottom (black) curves show the same QD spectra when the second excitation wavelength (1180 meV) is switched on. Considering the intensities of X and XX required for a correlation measurement, the QDs studied in this region were successfully tuned by DWE.

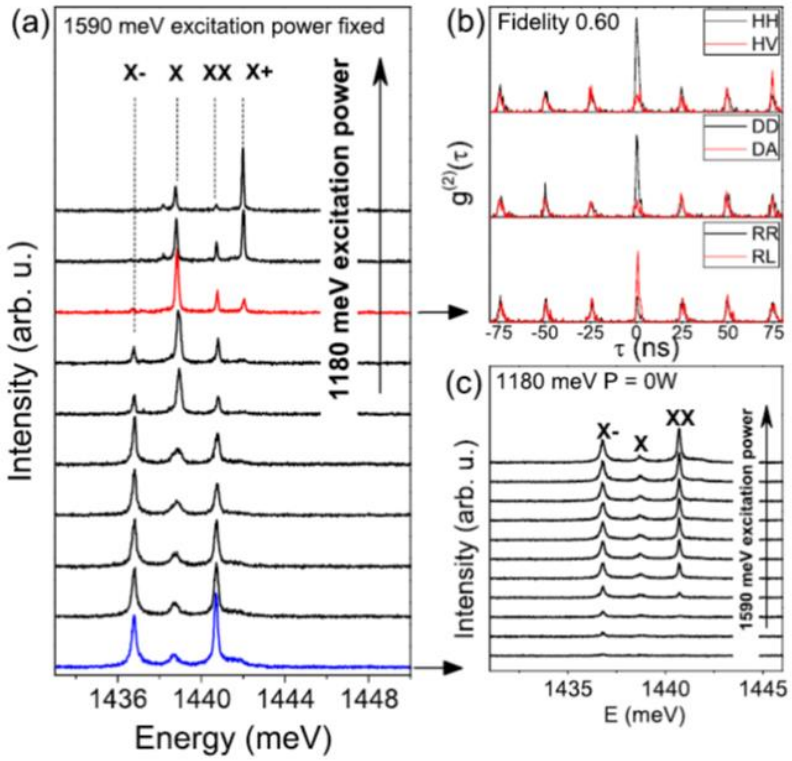

Fig. 4.2: (a) Power-dependent (charge-tuning laser) PL spectra of the studied QD as the power of the pumping laser is fixed; (b) Correlation spectra in linear, diagonal, and circular bases after neutralization; (c) Power-dependent (for pumping laser) PL spectra as the charge-tuning laser is switched off.

We would like to stress out that in some sample regions, probably due to higher negative charging or different states in the forbidden gap, DWE was ineffective. Therefore improvements in epitaxy and processing are needed in those cases. Or one can resort to resonant optical excitation to bypass the effects related to the feeding process [10-13].

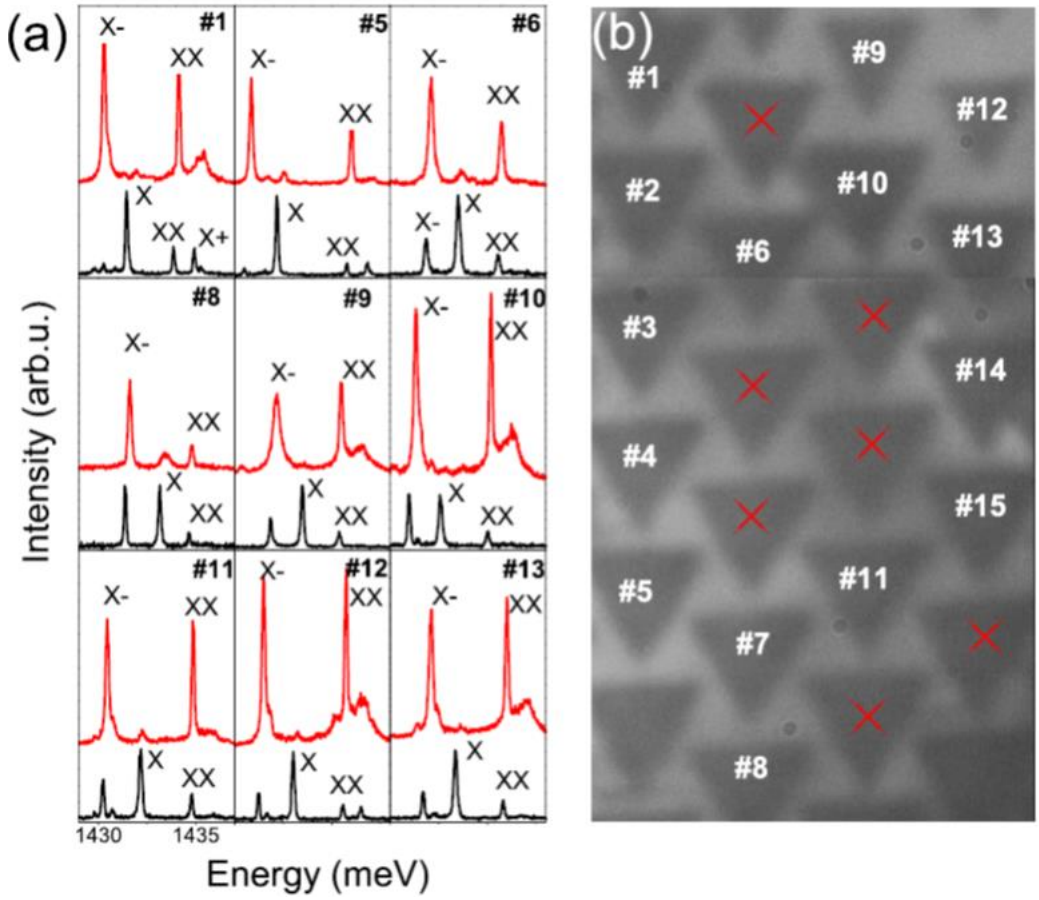

Fig. 4.3: (a) PL spectra of before (top) and after (bottom) charging-tuning for

4.2 Sacrificial QD layer(s)

When one considers self-assembled QDs (SAQDs), the positions of the first layer of QDs (within multi-stacked SAQD samples) would be the preferential sites for the growth of the following SAQD layers once the inter-QD-layer distances, generally referred to as spacers, are small enough (< 10/15 nm) [14,15]. This happens because the strain field of one dot layer influences the nucleation of the second one. In this sense, if one would like to study the boundary between coupled and non-coupled (e.g. electronically) in the broad sense of mutual interactions of vertically-aligned QD molecules (QDMs)/superlattices

[16,17], the range of spacer would be limited since the "memory effect" in nucleation sites for SAQDs disappears as the spacer is thicker than, let us say, 10 to 15 nm. However, in the PQD system, stacking QDs will vertically-align intrinsically, making it a promising template for preparing site-controlled QDMs/superlattices.

During the work we did to determine the boundary for actual electronic coupling in pyramidal QDMs (not discussed here), an unexpected but welcomed phenomenon was observed. Sample #421 structure was similar to the one discussed in the previous section but with an additional QD layer and a nominal 10-nm-thick spacer, with nominal thicknesses for both In0.25Ga0.75As QD layers being 0.5 nm. The μ-PL spectrum was measured and is shown in Fig. 4.4. The data are from the same spectrum and the different colors for different peaks are just for convenient depiction and were designated after cross-correlation measurements allowed proper peak identification. From the spectrum, the linewidths for the peaks corresponding to QD2 are narrower compared to the pair assigned to QD1. Moreover, QD1 and QD2 were grown from bottom to top in sequence and are nominally identical, while the exciton wavelength difference between the two QDs is approximately 1 nm, possibly due to the effect of change in the base self-limiting profile induced by the stacking. We set to test if the linewidths for the secondly-grown QD layer is narrower all the time (assuming one can tell which is which, not a straightforward assumption in a sample with two identical dots).

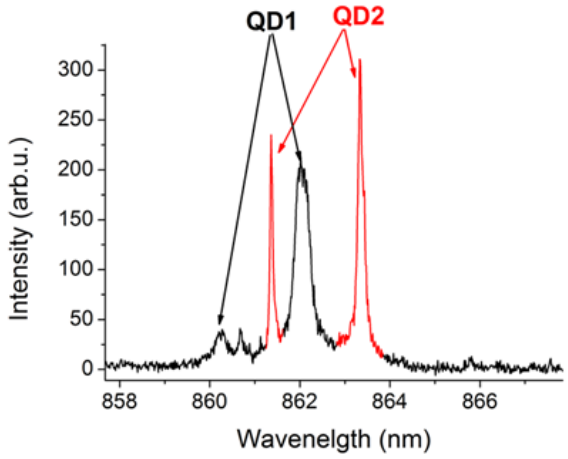

Fig. 4.4: A representative PL spectrum of sample #421 with a 10-nm-thick GaAs spacer.

To confirm our hypothesis, sample #422 was grown, sharing the same structure with sample #421 but with different nominal $In_{0.25}Ga_{0.75}As$:N QD layer thicknesses 0.7/0.85 (bottom/top). The discrepancy in layer thickness between the two QD layers separates more clearly the two pairs of excitonic transitions in emission energy, all being consistent with intuition, i.e. the thicker dot layer emits at relatively lower energy, as shown in Fig. 4.5 (a). Again, the linewidths corresponding to the top QD layer are narrower than those from the bottom QD layer. In addition, the intensity of the exciton from top QD layer was improved alongside, meanwhile, the negative trion wasn't dominant in the PL spectra, dissimilar to the situation for the bottom QD. These results suggested the exploitation of a firstly-grown QD layer as sacrificial layer to suppress the capture of excess electrons during the excitonic transitions of the second QD layer. So sample #423, with three $In_{0.25}Ga_{0.75}As$ QD layers and two 10-nm-thick spacers inserted between each QD layer was grown with nominal QD layer thickness, 0.45/0.6/0.45 nm (bottom/middle/top), and the narrowest peak linewidths and neutralized excitonic pattern was again obtained in the top QD layer, see in Fig. 4.5 (b), confirming our expectations.

Our samples are back-etched to increase the light extraction rate before optical measurements. In this case, the top QD layer was always separated from the etched surfaces by the other QD layers. In this sense, the lastly-grown QD layer is the most distant from surface trapped states. Our hypothesis is that the excess electrons, activated via non-resonant optical pumping, would affect the rest of the QDs first, resulting in relatively broad peaks and negative trion-dominating features [6]. As a consequence, the lastly-grown layer gets "screened" from the perturbation of the excess electrons, i.e. the first dots somehow act as "excess electron absorber/blockers." We observe that with the appropriate differences, this is somehow coherent with the function of the seed layer exploited to keep the nucleation site for the second SAQD layer growth as well as to improve the optical properties of the site-controlled single-SAQDs reported, e.g., in Ref. [18]. This explanation is, so far, merely a qualitative model. Indeed, a more systematic study is required to improve our understanding, requiring verification of a number of parameters such as spacer thickness, and so forth.

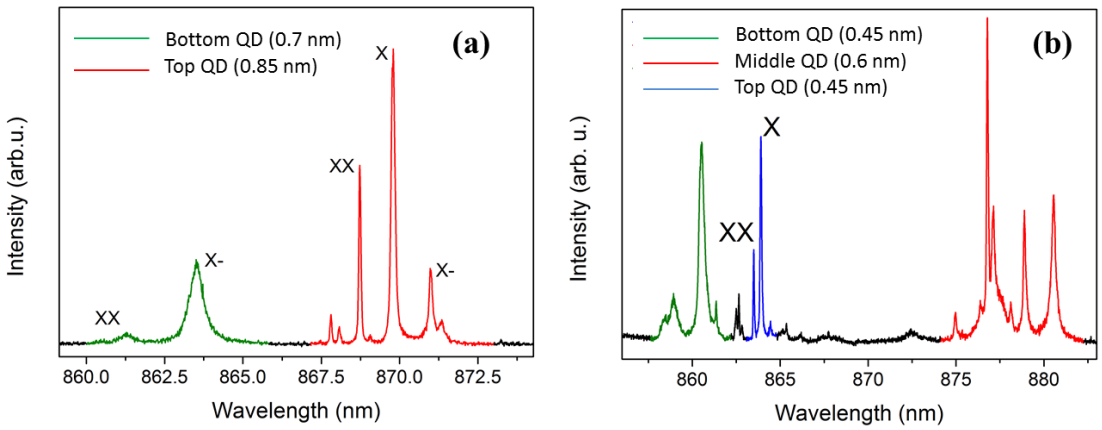

Fig. 4.5: Representative PL spectra of a pyramid from sample #422 and #423 (detail in the text).

4.3 AlAs etch-stop layer

As commented at the end of 4.1, a portion of the pyramids did not remain intact or were even fully destroyed after the back-etching step. Hence, it's worth to re-examine the epitaxial structures, especially in the design of etch-stop layers, to improve on this aspect.

In general, after the GaAs buffer layer, $Al_{0.45\rightarrow0.8}Ga_{0.55\rightarrow0.2}As$ and $Al_{0.8}Ga_{0.2}As$ layers would be grown before the growth of $Al_{0.55}Ga_{0.45}As$ cladding layers, GaAs barrier layers, and $In_{0.25}Ga_{0.75}As$ QD layers. The function of these two high-Al-content AlGaAs is to increase the etching selectivity over GaAs during the last wet chemical etching in NH_4OH:H_2O_2 solution for the back-etching procedure [19-21]. Since the etching selectivity between AlGaAs and GaAs would be enhanced with aluminum content increase, the intuitive idea is to insert an AlAs layer to improve the process. Meanwhile, as a pre-test for future p-i-n structures, the topmost layer (contact) better be a GaAs layer after back-etching. Then the sample #431 was grown with an additional AlAs etch-stop layer and a GaAs exposing layer, as depicted in Fig. 4.6.

The basic strategy is to keep more pyramids from being destroyed in the NH_4OH:H_2O_2 solution, as also judged by optical microscope (OM), by the inserted AlAs etch-stop layer, and then to etch away the three etch-stop layers by ~49 % HF or ~37 % HCl, allowing the GaAs "exposing" layer to appear.

Typically, with the assistance of the AlAs etch-stop layer, more than 75 % of apex-up pyramids in the processed piece appear undamaged. To test the GaAs termination, we processed two pieces of the same sample, which were terminated with etching in HF for 3 minutes and HCl for 10s, respectively. In Fig. 4.7, OM images were captured before and after HF or HCl, corresponding in (a) and (b). The random grey areas are due to the accumulation of oxidized Al(Ga)As layers formed during exposure in air after the NH_4OH solution etching, which have been also eliminated by the following either HF or HCl etching. Visually the quality is excellent.

Representative μ-PL curves, measured from PQDs in a very open region and partially open region (i.e. with pyramids more or less partially capped by residual substrate GaAs), are shown in Fig. 4.8 (a) and (b) correspondingly. Other than a slightly stronger background noise observed in the QDs from the very open regions, there is no significant difference between the two spectra. Noticeably, both spectra indicate the measured QDs are positively charged. In the general case (without an AlAs etch-stop layer), negative trions are dominant in the very open regions. This can possibly be ascribed to the fact that the surface states, which are originated in the back-etched surfaces, were changed, simply because the topmost material was HF/HCl-etched GaAs instead of NH_4OH-etched AlGaAs layer. Moreover, the percentage of emitting pyramids was increased, indicating the original protective function was also delivered.

To have a close look to the "new recipe" back-etched sample, a scanning electron microscope image was captured, see Fig. 4.9 (b). In the case of partially-open pyramids, we found a trench in the semi-insulating substrate matrix surrounding the structure. This can be understood by the schematics, depicted in Fig. 4.93.4 (a), in which the last etching (either by HF or HCl) would leave GaAs exposing layer coming out but also a trench is created by the AlGaAs removal.

In an optical pumping scheme, this isn't going to cause any issue, while the risk of electrical discontinuity will be posed for an electrical-driven device. Nevertheless, this potential risk could be removed by additional steps before deposition of a top contact metal (described in sequence) [22]: in short, coating a SiO_2 layer, spin-coating a layer of

photoresist (PR), open the PR aperture by oxygen plasma etching as the thickness of the PR layer is thinner at the pyramid summits, etching the part of SiO_2 at the tip with HF, removing the PR layer by acetone and isopropanol, finally deposition of contact metal.

Materials	Functions
GaAs	Buffer layer
AlAs	Etch-stop layer
$Al_{0.45\sim0.8}Ga_{0.55\sim0.2}As$	Etch-stop layer
$Al_{0.8}Ga_{0.2}As$	Etch-stop layer
GaAs	Exposing layer
$Al_{0.55}Ga_{0.45}As$	Cladding layer
GaAs	Barrier layer
$In_{0.25}Ga_{0.75}As$	QD layer
GaAs	Barrier layer
$Al_{0.55}Ga_{0.45}As$	Cladding layer
GaAs	Capping layer

Fig. 4.6: Epitaxial structure of sample #431 with inserted AlAs etch-stop layer.

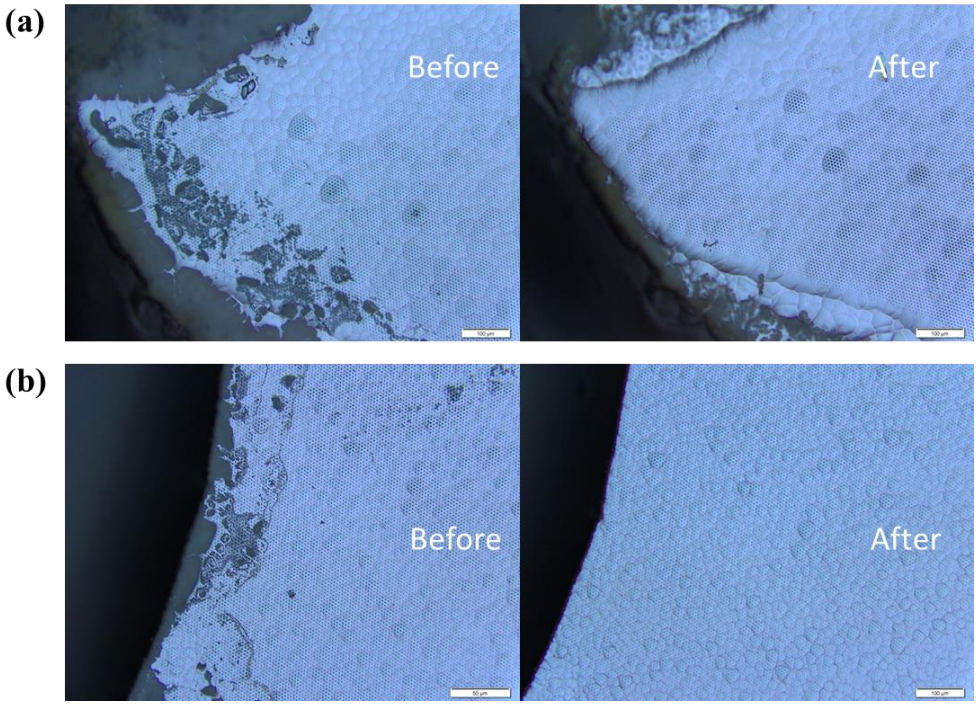

Fig. 4.7: OM images of samples #431 before (left) and after (right) etching (a) in HF for 30 s and (b) in HCl for 3 minutes.

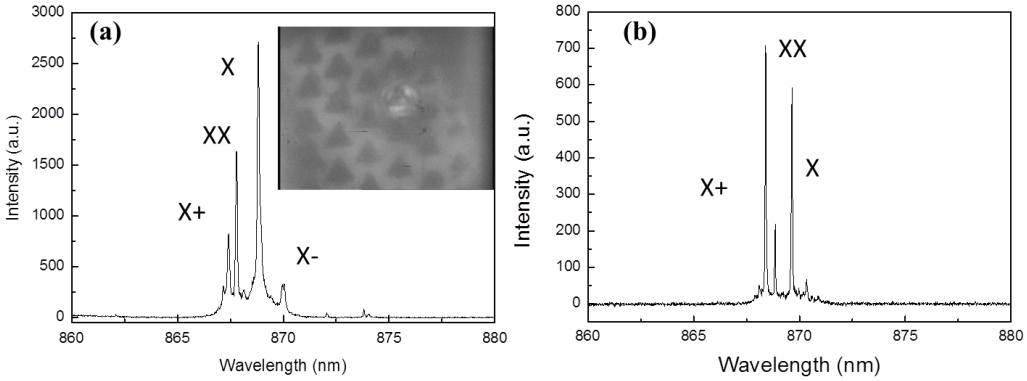

Fig. 4.8: PL spectra of a QD in (a) fully-open region and (b) partially-open area (insert: position of studied QD).

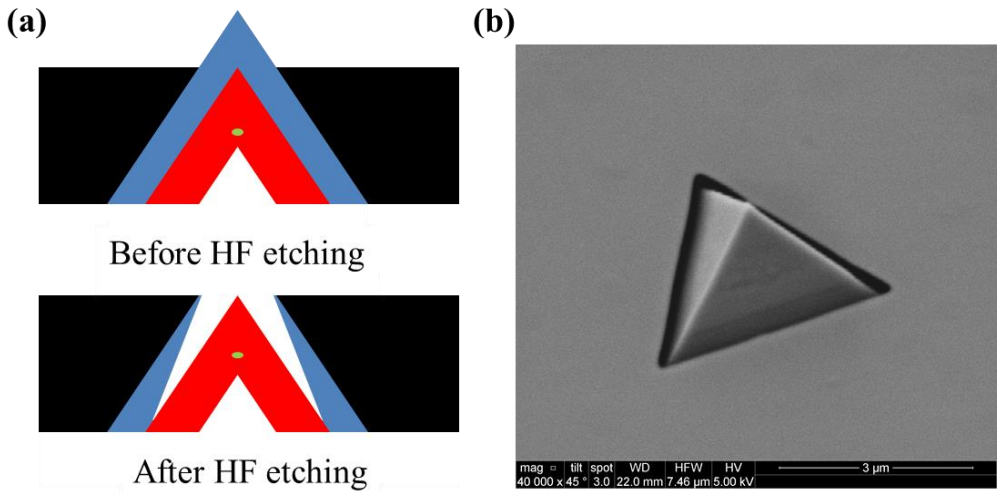

Fig. 4.9: (a) schematics of sample with AlAs etch-stop layer before (top) and after (bottom) HF etching; (b) a SEM pattern of an HF-etched PQD.

4.4 Summary

In this chapter, we have tested dual-wavelength excitation, sacrificial QD layer(s), and AlAs etch-stop layer to neutralize the environment of QDs. Based on dual-wavelength excitation, the excess electron density was neutralized by holes generated by a second pumping laser, which were trapped initially at defects of GaAs. On the other hand, sacrificial QD layer(s) play a role of excess electron absorber, resulting in not only dominating neutral excitonic transitions but narrower emission lines, compared to the

samples with only QD layer. Speaking of the insertion of AlAs etch-stop layer, the outcome from the studied samples indicates neutral-positive charging type. All these methods can be used to improve the probability of obtaining polarization-entangled photon pairs through biexciton-exciton-ground decay cascade.

Bibliography:

[1]: G. Juska, V. Dimastrodonato, L. O. Mereni, A. Gocalinska, and E. Pelucchi, Nat. Photon., 7 (2013) 527.

[2]: G. Juska, E. Murray V. Dimastrodonato, T-H Chung, S. T. Moroni, A. Gocalinska, and E. Pelucchi, J. Appl. Phys., 117 (2015) 134302.

[3]: E. S. Moskalenko, V. Donchev, K. F. Karlsson, P. O. Holtz, B. Monemar, W. V. Schoenfeld, J. M. Garcia, and P. M. Petroff, Phys. Rev. B, 68 (2003) 155317.

[4]: W-H Chang, H-S Chang, W-Y Chen, T. M. Hsu, T-P Hsieh, J-I Chyi, and N-T Yeh, Phys. Rev. B, 72 (2005) 233302.

[5]: M. K. Hudait, P. Modak, S. Hardikar, and S. B. Krupanidhi, J. Appl. Phys., 83 (1998) 4454.

[6]: A. V. Kuhlmann, J. Houel, A. Ludwig, L. Greuter, D. Reuter, A. D. Wieck, M. Poggio, and R. J. Warburton, Nat. Phys. 9 (2013) 570.

[7]: H. S. Nguyen, G. Sallen, M. Abbarchi, R. Ferreira, C. Voisin, P. Roussignol, G. Cassabois, and C. Diederichs, Phys. Rev. B, 87 (2013) 115305.

[8]: R. Singh and G. Bester, Phys. Rev. B, 85 (2012) 205405.

[9]: M. Abbarchi, F. Troiani, C. Mastrandrea, G. Goldoni, T. Kuroda, T. Mano, K. Sakoda, N. Koguchi, S. Sanguinetti, A. Vinattieri, and M. Gurioli, Appl. Phys. Lett., 93 (2008) 162101.

[10]: M. Muller, S. Bounouar, K. D. Jons, M. Glassl, and P. Michler, Nat. Photon., 8 (2014) 224.

[11]: S. Ates, S. M. Ulrich, S. Reitzenstein, A. Löffler, A. Forchel, and P. Michler, Phys. Rev. Lett., 103 (2009) 167402.

[12]: Y-M He, Y. He, Y-J Wei, D. Wu, M. Atatüre, C. Schneider, S. Höfling, M. Kamp, C-Y Lu, and J-W Pan, Nat. Nanotech., 8 (2013) 213.

[13]: X. Ding, Y. He, Z-C Duan, N. Gregersen, M-C Chen, S. Unsleber, S. Maier, C. Schneider, M. Kamp, S. Höfling, C-Y Lu, and J.-W Pan, Phys. Rev. Lett., 116 (2016) 020401.

[14]: S.Y. Shah, N. Halder, S. Sengupta, and S. Chakrabarti, Mater. Res. Bull., 47 (2012) 130.

[15]: Y. Sugiyama, Y. Nakata, T. Futatsugi, M. Sugawara, Y. Awano, and N. Yokoyama, Jpn., J. Appy. Phys., 36 (1997) L158.

[16]: M. Bayer, P. Hawrylak, K. Hinzer, S. Fafard, M. Korkusinski, Z. R. Wasilewski, O. Stern

, and A. Forchell, Science, 291 (2001) 451.

[17]: J. J. Palacios and P. Hawrylak, Phys. Rev. B, 51 (1995) 1769.

[18]: K. D. Jöns, P. Atkinson, M. Müller, M. Heldmainer, S. M. Ulrich, O. G. Schmidt, and P. Michler, Nano Lett., 13 (2013) 126.

[19]: A. R. Clawson, Mater. Sci. Eng.R-Rep., 31 (2001) 1.

[20]: Y. Uenishi, H. Tanaka, and H. Ukita, IEEE Trans. Electron Devices, 41 (1994) 1778.

[21]: K. Hjort, J. Micromech. Microeng., 6 (1996) 370.

[22]: M. H. Baier, Ph.D. Thesis, École Polytechnique Fédérale De Lausanne, 2005, P. 36.

Chapter 5:

Electrically-driven single-photon sources

Introduction

In most of our previous studies, the luminescence spectra of single quantum dots (QDs) were obtained through the recombination process of photo-excited excess carriers (photoluminescence, with a non-resonant excitation scheme), in which the properties of the light emitted from the QD essentially resulted from the feeding (a cascade process) from all the (excited) existing nanostructures into the lowest energy confined one, i.e. the QD [1-5].

Conversely, in electroluminescence (EL) spectra, the source of the recombining excess carriers is indeed current injection from doped regions. Hence, considering our pyramidal configuration, one has not only to contemplate the generic effect of the carrier feeding process as one would do in planar structures, but, as it will become clear in the following, stronger an attention should be paid on the design of the epitaxial structures to allow channel current paths mainly into QDs, without spreading to other nanostructures [6].

In this chapter, we will describe the development of an "effective" engineering of our epitaxial structures so to achieve selective injection channels compatible with the pyramidal system complexity, and discuss the EL spectra obtained under both continuous-wave (CW) and pulsed excitation. Finally, the demonstration of single-photon emission with trigger on-demand will be presented, the first such report for any site-controlled QD.

5.1 Identification of single-photon emission

It has now become a broadly exploited technology to utilize (intensity) photon correlation measurements of the emitted photons from quantum emitters to investigate their excitonic transitions. Moreover, one can rely on the results of second-order auto-

correlation curves to prove the existence of single-photon emission. The expression of second-order auto correlation functions is:

$$g_{i,i}^{(2)}(\tau) = \frac{<I_i(t)I_i(t+\tau)>}{<I_i(t)>^2}, \quad (5.1)$$

where $I_i(t)$ indicates the intensity of the excitonic transition *i* at time *t*. The $g_{i,i}^{(2)}(\tau)$ is the conditional probability of detecting the photons, coming from excitonic transition *i*, at time t as well as at a second one $t+\tau$. Ideally, if the emitting light is a series of single-photons, the value of $g_{i,i}^{(2)}(0)$ should be zero, which indicates a vanishing multiphoton event, commonly known as "antibunching". Therefore the result of $g_{i,i}^{(2)}(0)$ (how non-zero it is at zero delay) is commonly used as the main parameter to judge the quality of a single-photon emitter.

In practical experiment, a Hanbury Brown and Twiss (HBT) setup allows to measure second-order correlation functions [7] and is shown in Fig. 5.1.

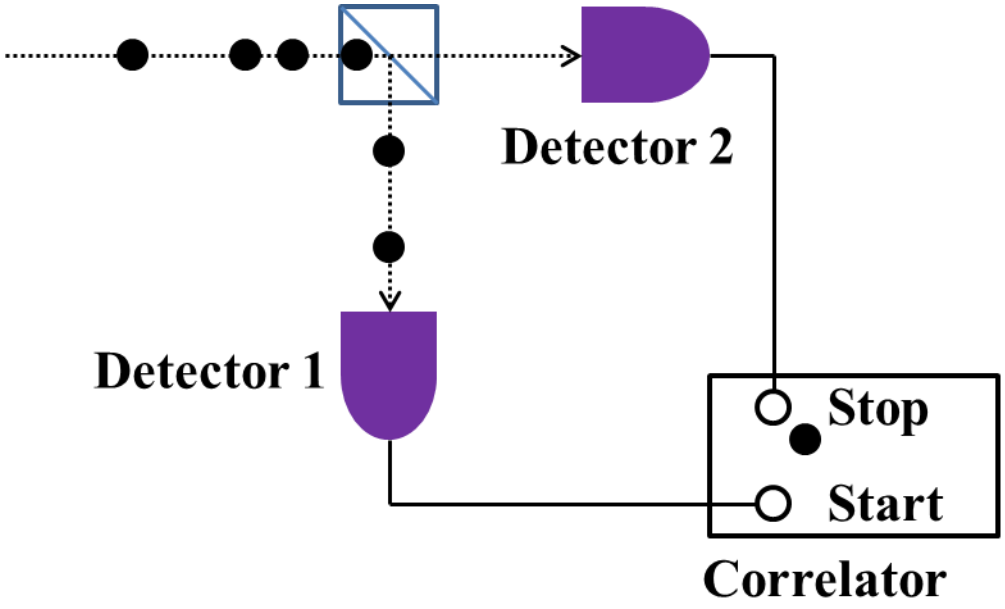

Fig. 5.1: Schematic HBT setup for second-order auto-correlation

All the QD measurement temperatures discussed in this chapter, if not differently specified, were set at 8 K with the sample sitting into our closed cycle cryostat. To measure an auto-correlation curve, the emitted photons from the excitonic transition of

choice will pass a monochromator so to filter out the rest of the emission. They are then split by a 50:50 beamsplitter without polarization preference into two arms with an avalanche photodiode (APD) each, operated as single-photon detectors. Finally, the detected signals are connected with a time-correlated single-photon counting (TCSPC) module. The first of the two APDs detecting a photon triggers a "start" button, while the second, the delayed detection, triggers a "stop" signal. The second-order correlation function is derived by the histogram constructed from the time interval between all the events of detected start and stop signals. It should be said that since the signal of single-photon detection is not generally a particularly intense one, the reconstruction of the correlation behavior relies on photon statistics obtained after a not-too-short integration time (tens of minutes, typically). In general, the threshold for being identified as (not necessarily a perfect one) single-photon emission is $\boldsymbol{g_{i,i}^{(2)}(0)}$ below 0.5 [8].

5.2 Engineering of epitaxial structures

In Chapter 2.2.4, we have briefly discussed the general design of epitaxial structures. Here, for the study of electrically-pumped devices we investigate three different structures, which are labeled as sample #51A, #51B, and #51C in sequence, depicted in Fig. 5.2. In sample #51A, the sequence of doping regions is n-i-p, while the order was swapped in the other two samples. Within the intrinsic region, the $In_{0.25}Ga_{0.75}As$ QD layer was sandwiched by GaAs barriers.

The initial idea of swapping doping sequence was to utilize p-doped AlGaAs etch-stop layers to attract, during back-etching process, more hydroxide ions, leading to improve etching selectivity of GaAs over AlGaAs. Even though it was fundamentally untested systematically, the doping sequence was subsequently kept this way. The modifications in #51B were a p-doped GaAs inserted between the doped etch-stop layer and the p-doped $Al_{0.55}Ga_{0.45}As$ layer, and two $In_{0.25}Ga_{0.75}As$:N QD layers, separated by 10 nm GaAs spacer, which were sandwiched by GaAs layers and cladded by two $Al_{0.75}Ga_{0.25}As$ layers. Two QD layers were employed to improve the emitting properties as discussed in Chapter 4.2, while the two $Al_{0.75}Ga_{0.25}As$ layers served as leakage-blocking function, which will be discussed later. As for sample #51C, the pitch

dimension was 10 μm, while the rest were 7.5 μm. Regarding to structure, in #51C the p-doped $Al_{0.55}Ga_{0.45}As$ layer was removed, and there was only one QD layer confined as in sample #51A.

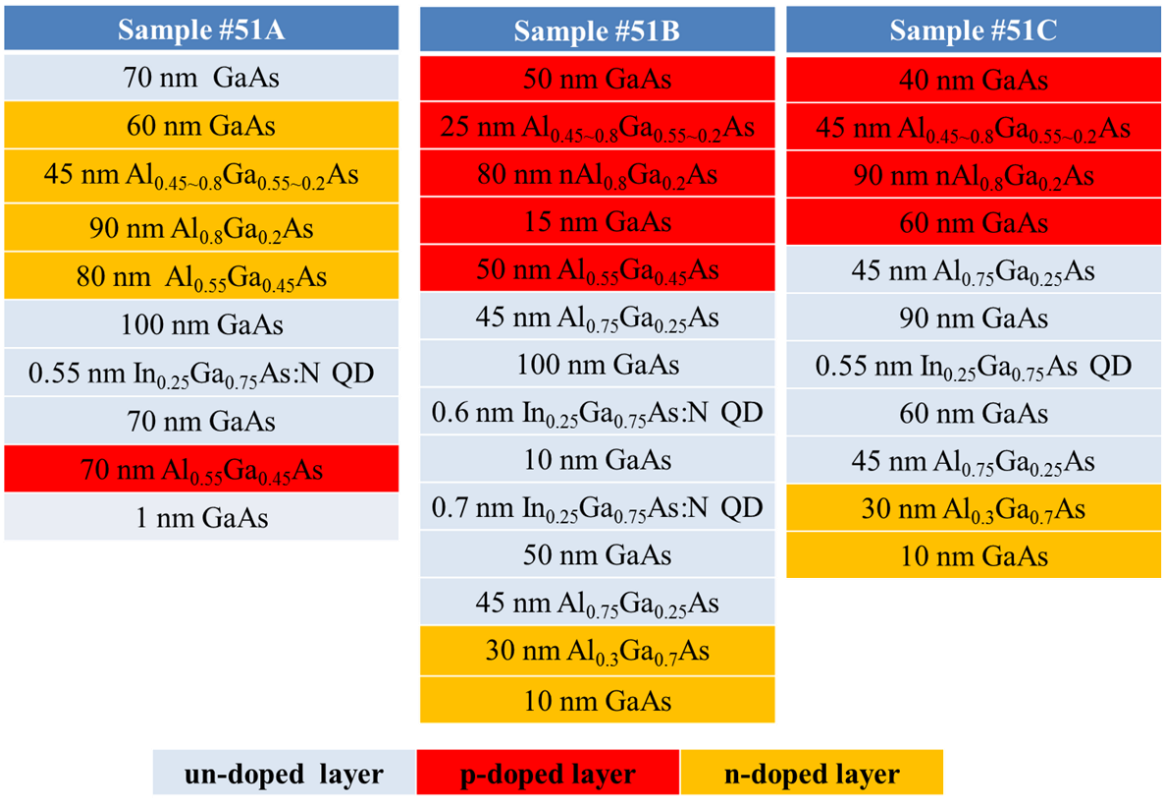

Fig. 5.2: Epitaxial structures of sample #51A, #51B, and #51C.

5.3 Simulations of device model

Sample #51A was the first fabricated device, which was designed as a simple light-emitting diode (LED) at the early stages of this project. Importantly, there was no emission detected (QD or other nanostructures related). This is true even if in the device was passing a significant current, which was high enough to raise up the local temperature as indicated by the cryostat thermal controller, and, after the voltage was raised significantly, ended up with an electrical short.

To explain this failure, we need to recall the previously-discussed non-planarity of pyramidal structures that produce a relatively short path between p-doped and n-doped regions on the side facets compared to the path through the QD, as can be observed in

the red arrow on the scanning electron microscope pattern shown in Fig. 5.3. Overall, this should lead to a low probability for current to flow through the central QD position, indicated by the blue arrow. Nevertheless there is a more serious issue as one can observe in Fig. 5.3. There is a significant facet development at the corners of the pyramidal recesses which develops into a rather thinner layer growth, compared to the thicknesses of layers grown along (111)A planes, for both n and p layers, indicated in circled region. It is then expected that the circled area is indeed a more favorable path for the current, easily causing an electrical short.

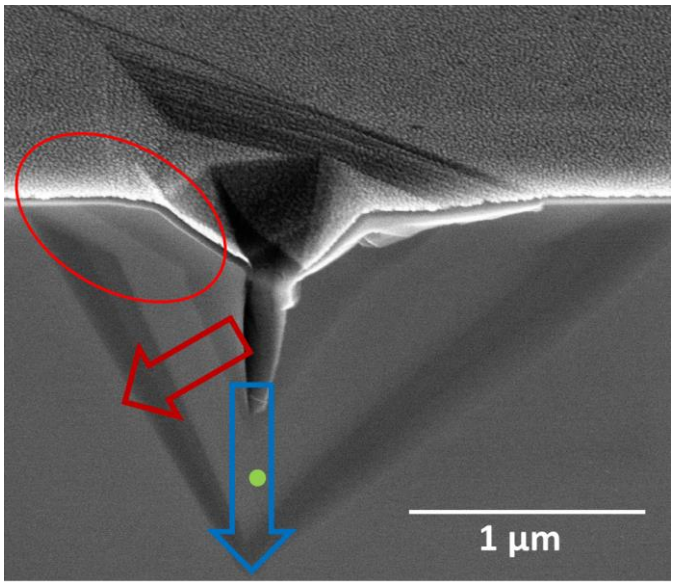

Fig. 5.3: A tilted SEM image of a cleaved pyramid, where the green spot indicates the position of a pyramidal quantum dot.

To bypass this issue, one possible solution is to restore the step of surface etching (SE) [1-3,6], despite the fact that we have eliminated its necessity in Chapter 2.3.1. However, even if the circled area may be suited to be etched away (this would be anyway risky and could destroy non-trivially part of the pyramids), this approach would still not solve the problem of the low probability for the current to flow through the central QD, compared to the path through the side facets.

Indeed, a more effective and stable solution would be preferred, and it would be even better if it could avoid an increase in number of steps in the fabrication process.

That is the reason why we modified the (engineering of the) structure with the insertion of two $Al_{0.75}Ga_{0.25}As$ layers in sample #51A and #51B. The first is grown after the growth of the p-region and the other one grown before the growth of the n-region. These two barrier layers have two functions: first, on the side facets as well as at the corner of pyramidal recesses, these would result in a high bandgap region, effectively reducing carrier transport through them, i.e., they partially act as insulators (or transport barriers) separating undoped region from doped ones. Second, we can benefit from a fundamental process: the formation of a vertical quantum wire (VQWR) with low aluminum content at the center of two $Al_{0.75}Ga_{0.25}As$ layers, thanks to the gallium segregation into center of pyramidal recess as discussed in Chapter 2 [9,10]. In Fig. 5.4 (a), it depicts a magnified region at the central part of a pyramid with one QD only, based on sample #51C.

For qualitatively testing of our initial intuition, finite elements simulations were performed, using COMSOL Multiphysics 5.0, in collaboration with Dr. A. Pescaglini. To calculate the voltage and carrier density (electrons and holes), the simulations solved Poisson's equation in parallel with continuity equations. We started the calculation in a 2D geometry at first, and a rotational symmetry along the vertical directions was later applied to confer a 3D structure to the simulated geometry to improve the approximation to a pyramidal structure. The 2D geometry consisted of a half cross section of a regular pyramidal structure with side length of **7 μ**m cut through the center. The vertical wire in the center of the 3D geometry was approximated to a cylinder with diameter of 100 nm. The structure used for simulation was composed of 7 layers, which are the same as the structure of sample #51C, starting from 60-nm-thick p-doped GaAs to the n-doped $Al_{0.3}Ga_{0.7}As$ layer, with only one change in InGaAs layer thickness, where for numerical reasons 1 nm was applied instead of 0.55 nm. Also, to take into consideration the alloy segregation [9] in the vertical quantum wires, the Al concentrations in the different layers were reduced in the center part: x = 0.3 was substituted with x = 0.05, and x = 0.75 was substituted with x = 0.26 following literature data [9]. The doping concentrations for both p-doped and n-doped layers were 1 x 10^{18} cm^{-3}, where the external surface for the top p-doped layer was set at a constant voltage of 1.5 V and the bottom n-doped layer was set to ground. The current density values, shown in Fig. 5.4

(b), are the values calculated from the electric field distribution E and the conductivity $\boldsymbol{\sigma}$ using the relation $\boldsymbol{J = \sigma E}$. From the simulation results (Fig. 5.4 (b)), one can see a preferential current path at the center. Even though, from data inspection, the VQWR does not impede the current flow to other quantum structures, most of the current is indeed channeled to the center region. Hence, these simulations supported our Ansatz that by the insertion of two $Al_{0.75}Ga_{0.25}As$ layers, a fundamentally selective injection channel is formed.

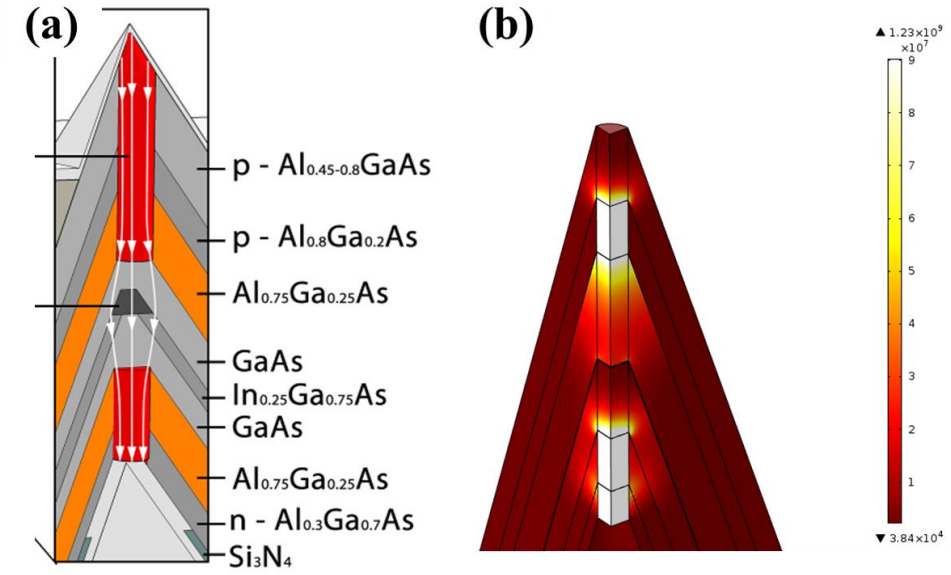

Fig. 5.4: (a) scheme of magnified central part of a pyramidal with a QD, and (b) current density simulation result with color-map.

5.4 emissions from site-controlled quantum structures

With the modified structure, emission from individual $\boldsymbol{\mu}$-LEDs started to be detected. In Fig. 5.5 (c), a representative array of $\boldsymbol{\mu}$-LEDs of sample #51B were gradually turned on. The bright spots of the spectrally unfiltered integrated electroluminescence (EL) match the initial pyramidal recess pattern, demonstrating that each individual pyramid turns on without significant leakage through the GaAs substrate. This is confirmed by a macro-EL spectrum in Fig. 5.5 (b), where the dominant luminescence features at high global injection current of 4 mA are InGaAs lateral quantum wire (LQWRs) and lateral quantum well (LQWs), clearly exceeding the single

QD luminescence and easily observable using a regular CCD imaging camera. The non-uniformity of the intensity regions reflects differences between individual ***μ***-LEDs, as the turn-on voltages between individual ***μ***-LEDs can be slightly different. Moreover, the current-voltage curve, shown in Fig. 5.5 (a), is rather the characteristic of the whole ensemble and not just of a single device. We stress that in the current fabrication process, once the driving current is beyond a threshold, it is not only one single ***μ***-LED which is turned on but a group of them. However, we stress that there is no sophisticated processing steps required to realize the control of a single device or a specific subset of them if required.

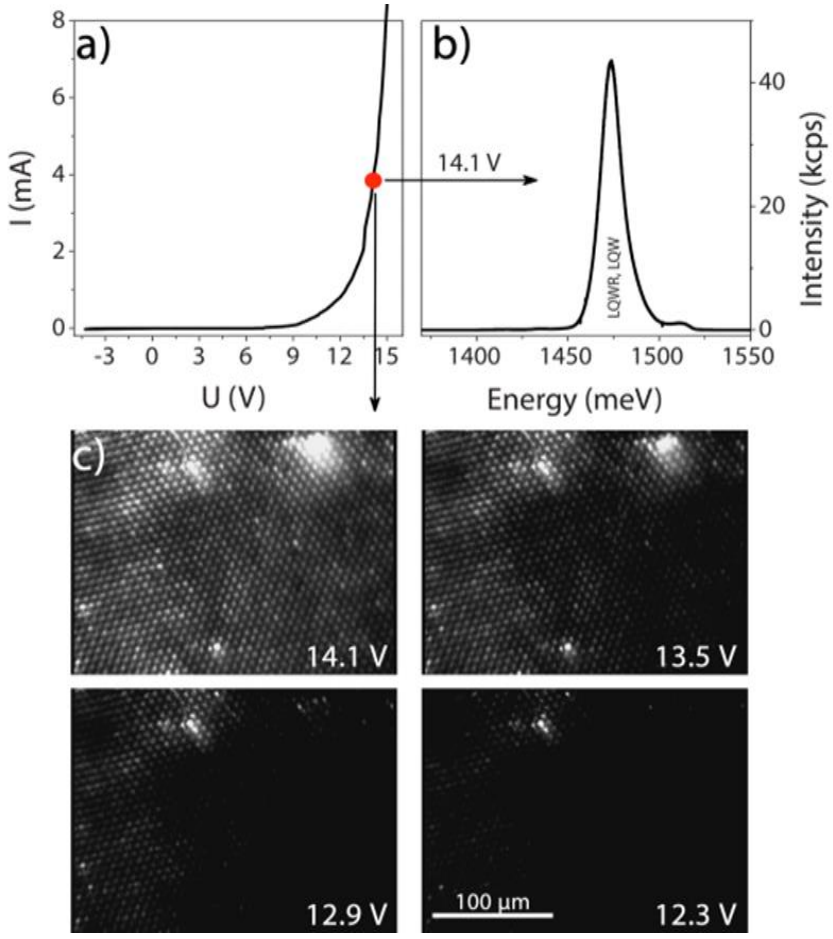

Fig. 5.5: (a) Current-voltage curve of the sample #51B, (b) Macro-EL spectrum taken under applied bias of 14.1 V, and (c) Optical images of switching-on **μ**-LEDs with increasing applied bias.

Several phenomena are possibly contributing to some inhomogeneity of the electrical injection properties: (1) an inhomogeneous etching profile during the back-etching step, (2) a complex non-planar surface profile of the back contact side due to slightly irregular MOVPE growth towards to the center of the pyramid, which tends to close the recess irregularly creating variables conditions for a back-contact formation, and (3) by the presence of resistance at the contact side (most probably the p-doped side). These issues also can (may be partially) explain why the turn-on voltage is unexpectedly high, around 7 V or more, which is larger than the case of "normal" LED with self-assembled QDs [11-13]. More work is ongoing to improve our knowledge on the source of this unexpected high turn on voltage.

5.5 μ-LEDs under CW excitation

By reducing the light-collecting area with a 50X objective, the micro-EL spectra from a representative single QD in sample #51B with increasing driving currents are shown in Fig. 5.6 (a). The identification of the excitonic structures was obtained by current-dependent EL and polarization-dependent EL, in parallel with correlation spectroscopy. It should also be said that the spectral feature of EL samples does not substantially differ from their optically pumped counterparts, helping in the excitonic identification. From the spectra, clear negatively-charged exciton (X^-), exciton (X), and biexciton (XX) peaks are observed, where the intensity of X^- is particularly intense. Hence, we measured the second-order autocorrelation spectrum of X^-, whose result is displayed in Fig. 5.6 (b). Obviously, the vanishing value at zero delay indicates that reduced multiphoton events were detected. The fitting value of $g^{(2)}(0)$ is 0.2, but it should be said that it is the result of a convolution of the real $g^{(2)}(0)$ function with the instrument-response function. The deconvolution process to extract the real $g^{(2)}(0)$ requires information on the instrument response function, lifetime of the transition, noise level, and/or carrier capture rate. Since these parameters are excitation power-dependent, we caution the reader that the estimation of $g^{(2)}(0)$ can have limited reliability.

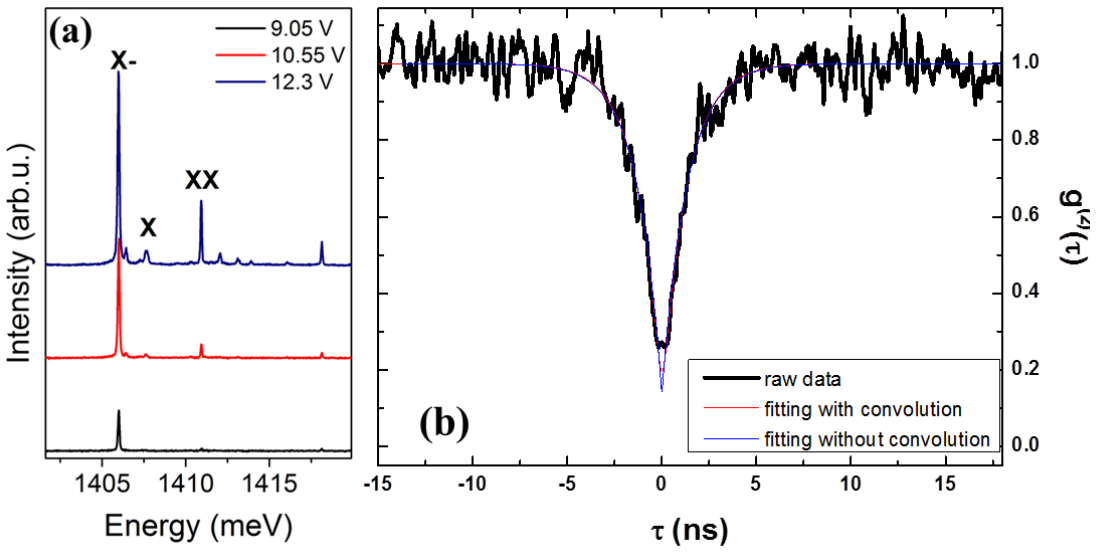

Fig. 5.6: (a) Voltage-dependent EL spectra, and (b) The second-order correlation function of X- taken under applied bias of 9.6 V.

A way to partially overcome this problem is measuring the $g^{(2)}(\tau)$ curve by a pulsed mode excitation, as will be discussed in the following section. This would also provide control of the triggering on demand, so to match requirements of quantum information technologies. We also performed the curve fitting of $g^{(2)}(\tau)$ after deconvolution, seen in Fig. 5.6 (b), and obtained a $g^{(2)}(0)$ of 0.16. Both values of $g^{(2)}(0)$ are below the threshold, 0.5, so to prove single-photon emission by electrical injection based on the site-controlled PQD system.

5.6 μ-LEDs under pulse excitation

To measure the properties under pulse excitation, we employed a mixture of DC and AC inputs. In which the DC voltage, 3.8 V, was set just below the limit which allows to observe the emission from a QD, and the AC pulse came with a 10.5 V amplitude, frequency of 66 MHz, and pulse width of 1.4 ns, seen in the insert of Fig. 5.7 along with the time-resolved EL spectrum of a representative QD. The emission under such pulsed excitation could only be obtained from sample #51C but not from #51B, thanks probably to a lower resistance and parasitic capacitance of the structure. In Fig. 5.7, transitions of X, XX, and X^- can be observed in the EL spectrum of a representative

QD, in which the negative trion still dominates in intensity. Second-order correlation curves of the negative trion are displayed in Fig. 5.8. The value of $g^{(2)}(0)$ without any time-gating is $0.185 \pm \mathbf{0.057}$, which confirms the demonstration of electrically-driven single-photon emission with trigger on demand. This result is obtained for the first time when compared to any site-controlled system [13,14], proving the versatility of the PQD system in meeting both control in spatial position and trigger on demand. Due to the limitation of our input pulse (limitations induced by the hardware availability), the pulse width is at the same timescale with the excitonic lifetime. Hence the probability of re-excitation is expected to be not-negligible, leading to an increase of $g^{(2)}(0)$.

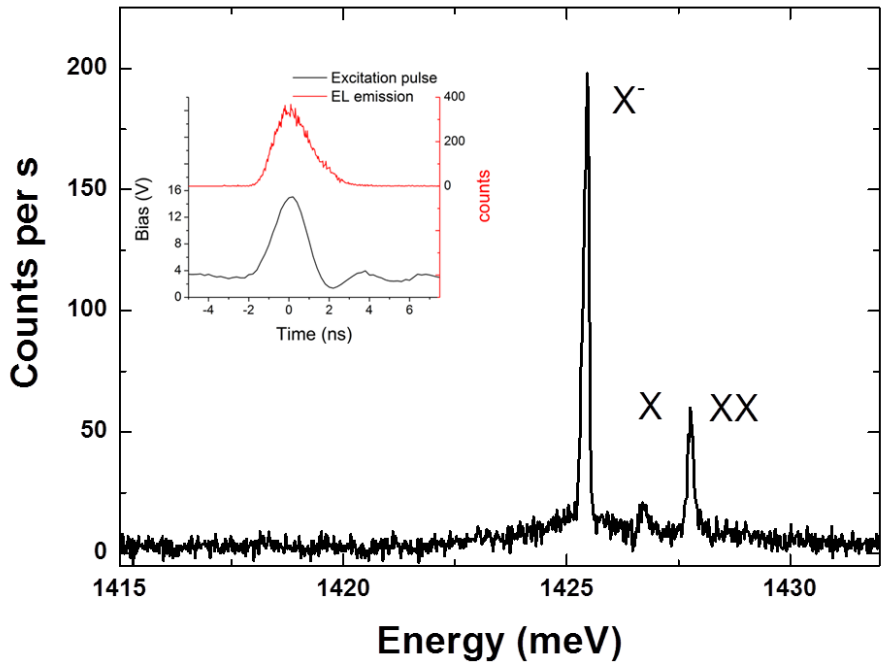

Fig. 5.7: integrated EL spectrum and input pulse shape and time-resolved EL spectrum (insert).

To address this issue, an optimization of either epitaxial design or device processing should be performed to minimize the total impedance, allowing the device to operate with smaller pulse amplitudes, and narrower pulse widths. Another way is to conduct a post-selection, i.e. time-gating filtering the "good" events. In Fig. 5.8 (a) and (c), the temporal gating width are 6.5 and 5.5 ns, respectively, which can further reduce the

$g^{(2)}(0)$ to $0.088 \pm \mathbf{0.059}$ and $0.078 \pm \mathbf{0.066}$, respectively. In these cases, only 5 % and 10 % of the intensity is discarded.

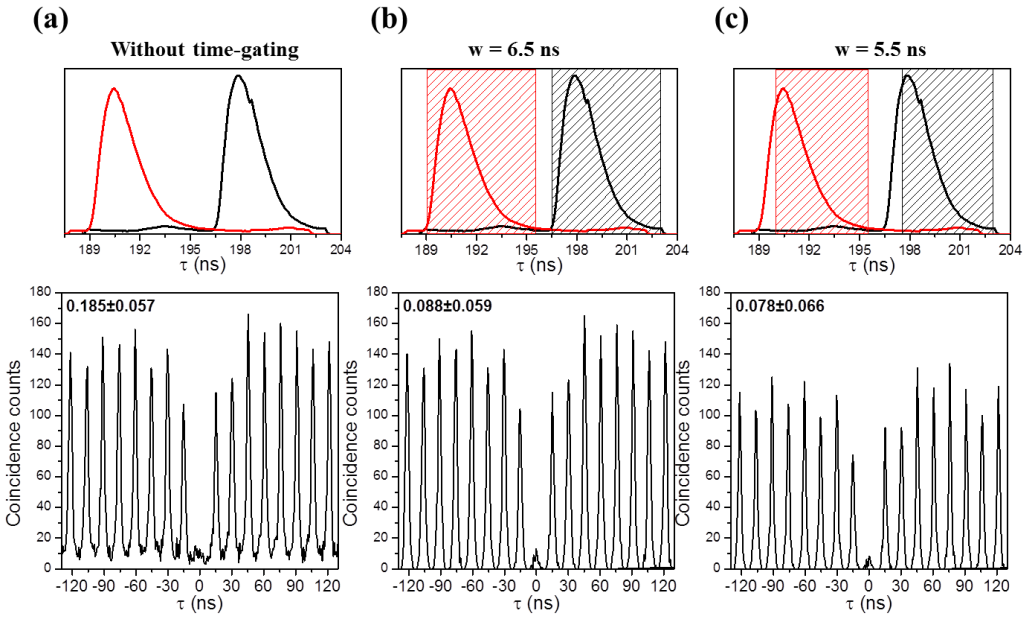

Fig. 5.8: second-order spectra (lower) and temporal gating windows (upper) for (a) without gating, (b) w = 6.5 ns, and (c) w = 5.5 s. Two successive pulses are shown in the upper panels, showing the regions of overlap and the gating window.

5.7 Summary

By engineering the epitaxial structure, a selective carrier injection channel is formed within pyramidal light-emitting diodes. Owing to this advantage, electrically-pumped single-photon sources have been realized under either continuous mode excitation or pulse mode excitation. It is worth to mention the latter achievement is observed for the first time over all epitaxial quantum dot systems (published) with a value of $g^{(2)}(0)$ down to 0.078±0.066 as combining with a time-gating technique.

Bibliography

[1]: L. O. Mereni, V. Dimastrodonato, R. J. Young, and E. Pelucchi, Appl. Phys. Lett. 94 (2009) 223121.

[2]: V. Dimastrodonato, L. O. Mereni, G. Juska, and E. Pelucchi, Appl. Phys. Lett. 97 (2010) 072115.

[3]: G. Juska, V. Dimastrodonato, L. O. Mereni, T. H. Chung, A. Gocalinska, and E. Pelucchi, B. Van Hattem, M. Ediger, and P. Corfdir, Phys. Rev. B 89 (2014) 205430.

[4]: G. Juska, V. Dimastrodonato, L. O. Mereni, A. Gocalinska, and E. Pelucchi, Nat. Photon. 7 (2013) 527.

[5]: G. Juska, E. Murray V. Dimastrodonato, T-H Chung, S. T. Moroni, A. Gocalinska, and E. Pelucchi, J. Appl. Phys., 117 (2015) 134302.

[6]: M. H. Baier, C. Constantin, E. Pelucchi, and E. Kapon, Appl. Phys. Lett. 84 (2004) 1967.

[7]: R. H. Brown, and R. Q. Twiss, Nature, 177 (1956) 27.

[8]: P. Michler, A. Kiraz, C. Becher, W. V. Schoenfeld, P. M. Petroff, L. Zhang, E. Hu, and A. Imamoglu, Science, 290 (2000) 2282

[9]: V. Dimastrodonato, E. Pelucchi, and D. D. Vvedensky, Phys. Rev. Lett., 108 (2012) 256102

[10]: S. T. Moroni, V. Dimastrodonato, T-H Chung, G. Juska, A. Gocalinska, D. D. Vvedensky, and E. Pelucchi, J. Appl. Phys., 117 (2015) 164313.

[11]: Z. Yuan, B. E. Kardynal, R. M. Stevenson, A. J. Shields, C. J. Lobo, K. Cooper, N. S. Beattie, D. A. Ritchie, and M. Pepper, Science, 295 (2002) 102

[12]: F. Hargart, C. A. Kessler, T. Schwarzbäck, E. Koroknay, S. Weidenfeld, M. Jetter, and P. Michler, Appl. Phys. Lett., 102 (2013) 011126.

[13]: T. Heinder, C. Schneider, M. Lermer, S. H. Kwon, T. Braun, S. Reitzenstein, S. Höfling, M. Kamp, and A. Forchel, Appl. Phys. Lett., 96 (2010) 011107.

[14]: W. Unrau, D. Quandt, J.-H. Schulze, T. Heidhel, T. D. Germann, O. Hiltzemann, A. Strittmatter, S. Reitzenstein, U. W. Pohl, and D. Bimberg, Appl. Phys. Lett., 101 (2012) 211119.

Chapter 6:

Electrically-driven polarization-entangled photon pairs

Introduction

In this chapter, based on the pre-patterned substrates and the fabrication process developed for light-emitting diodes as previously discussed, the highly-symmetric properties of pyramidal quantum dots (PQDs) are further expanded upon and exploited. Symmetry is essential for the reduction of the fine-structure splitting (FSS) in excitonic transitions. Taking advantage of this characteristic, polarization-entangled-light-emitting diodes were demonstrated on our site-controlled platform for the first time. Moreover, the fidelity to highly entangled states obtained from the characterized devices was shown to be sufficiently high to violate Bell's inequalities by using time-gating techniques. This is a clear demonstration that the PQD system is a very promising entangled light source for further on-chip quantum applications due to its both position-controlled growth and triggering on demand capabilities.

6.1 Working principle

In 2000, O. Benson et al., have proposed the exploitation of a single quantum dot (QD) as a template to generate polarization-entanglement photon pairs due to its atomic-like level structure [1]. Following their proposal a single QD is populated with two electron-hole pairs and entanglement will reside in the superposition of the biexciton (XX) and exciton (X) polarization emission states after the XX-X-ground (G) excitonic decay cascade. In Fig. 6.1 (a), the scheme of XX-X-G decay cascade from an ideally symmetry QD is sketched. Here, the intermediate state is degenerate: i.e. it must have a zero-value of FSS (an FSS is present by definition if the intermediate excitonic state is split into two sublevels). Under such circumstance, the expected maximally entangled state of such a photon pair is expressed as $|\boldsymbol{\psi}\rangle = \frac{\mathbf{1}}{\sqrt{\mathbf{2}}}(|\boldsymbol{R_{XX}}\otimes\boldsymbol{L_X}\rangle + |\boldsymbol{L_{XX}}\otimes\boldsymbol{R_X}\rangle)$, where L and R correspond

to left-handed and right-handed circular polarizations, respectively. According to the Jones vector system, the polarization may be expressed as: $|\boldsymbol{R}\rangle = \frac{\mathbf{1}}{\sqrt{\mathbf{2}}}(|\boldsymbol{H}\rangle + \boldsymbol{i}|\boldsymbol{V}\rangle)$, $|\boldsymbol{L}\rangle = \frac{\mathbf{1}}{\sqrt{\mathbf{2}}}(|\boldsymbol{H}\rangle - \boldsymbol{i}|\boldsymbol{V}\rangle), |\boldsymbol{D}\rangle = \frac{\mathbf{1}}{\sqrt{\mathbf{2}}}(|\boldsymbol{H}\rangle + |\boldsymbol{V}\rangle)$, and , $|\boldsymbol{A}\rangle = \frac{\mathbf{1}}{\sqrt{\mathbf{2}}}(|\boldsymbol{H}\rangle - |\boldsymbol{V}\rangle)$, where V, H, D, A, denote vertical, horizontal, diagonal, and anti-diagonal states. Thus the maximally entangled state can be transformed to Eq. 6.1 and 6.2, in linear and diagonal bases, correspondingly:

$$|\boldsymbol{\psi}\rangle = \frac{\mathbf{1}}{\sqrt{\mathbf{2}}}(|\boldsymbol{H_{XX}}\otimes\boldsymbol{H_X}\rangle + |\boldsymbol{V_{XX}}\otimes\boldsymbol{V_X}\rangle), \tag{6.1}$$

$$|\boldsymbol{\psi}\rangle = \frac{\mathbf{1}}{\sqrt{\mathbf{2}}}(|\boldsymbol{D_{XX}}\otimes\boldsymbol{D_X}\rangle + |\boldsymbol{A_{XX}}\otimes\boldsymbol{A_X}\rangle), \tag{6.2}$$

However, in most of the reported QD systems as summarized in Fig. 6.1 (b), the intermediate states are non-degenerate, resulting in an intrinsic non-zero FSS. This, unfortunately, impedes/reduces the experimental determination/reconstruction of the entangled states. Indeed, in this scenario, the two-photon state is modified to:

$$|\boldsymbol{\psi}\rangle = \frac{\mathbf{1}}{\sqrt{\mathbf{2}}}(|\boldsymbol{H_{XX}}\otimes\boldsymbol{H_X}\rangle + \mathbf{exp}(\boldsymbol{iSt})|\boldsymbol{V_{XX}}\otimes\boldsymbol{V_X}\rangle), \tag{6.3}$$

where S represents the value of the FSS and t is the time delay between first XX and second X emitting events [21,22]. The non-zero FSS will cause quantum beating [31], which will also lead to "experimental" photon polarizations that are classically correlated instead of entangled as seen when polarization projective measurements are (statistically) performed [32], as we also discussed in ref [15].

Indeed, it is worth to caution the reader that, even in the presence of non-zero FSS, entanglement is still preserved. However, since the current method utilized to reconstruct the entanglement is based on time-averaging a collection of events assumed to be identical. When such assumption is not correct (as the case in the presence of a randomly varying phase term given by the product *St*, with *t* being, in each individual event, the exponentially distributed exciton decay time), experimental results become indistinguishable from a classically distributed statistics. Hence there is an upper threshold for FSS, ~ 4 $\boldsymbol{\mu}$eV,

required to maintain "measurable" the quantum correlation between the two decay paths (this value is valid only if the carrier lifetime is of the order of 1 ns) [21].

To eliminate the FSS limitation, researchers have resorted to external physical quantities which can bear a broader flexibility compared to the simple tuning of growth parameters [14,15], such as post-growth annealing [14,20], external vertical electrical fields [17], in-plan electrical fields [33], magnetic fields [2,3,16], piezoelectric fields [12,18,19], etc. Nevertheless, one of the very important advantages for the PQD system compared to conventional self-assembled QD system on (001)-oriented substrates, is a higher symmetry, ideally C_{3v} [34]. Therefore in this chapter, without additional parameters to adjust, we concentrate on values of the FSS for our samples which are sufficiently close to zero and perform further correlation tests.

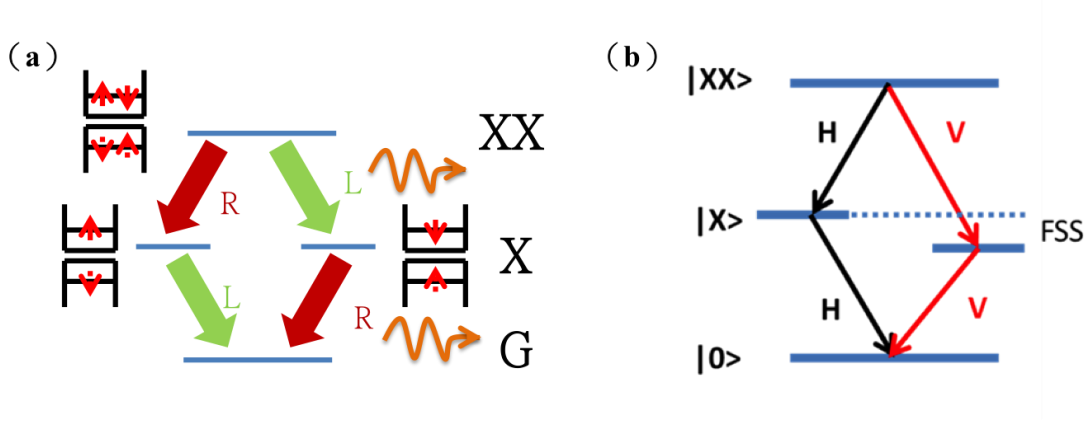

Fig. 6.1: Schematics of XX-X-G decay cascade with (a) zero FSS and (b) with finite FSS.

6.2 Experimental procedures

To extract the electroluminescence (EL) data from individual PQDs, the emissions were, as for the discussion presented in previous chapters, taken in a conventional micro-photoluminescence set-up [5,13,15] using 100X magnification, 0.80 NA long-working distance objective sketched in Fig. 6.2. With a closed-cycle cryostat, the measurement temperature was cooled down to 10 K. PQDs were pumped by DC currents or electrical pulses mixed with DC currents for continuous wave (CW) or pulsed mode operation. For correlation measurements, the collected emissions, corresponding to X and XX were

filtered by two monochromators equipped with 950 grooves/mm gratings (TE/TM diffracted intensity ratio ~1 at 877 nm). A polarizing beamsplitter (PBS) was used to separate each transition and silicon avalanche photodiodes (APDs) were applied as detectors. Precise polarization projections can be selected by placing a half-wave-plate (HWP) and quarter-wave-plate (QWP) in each arm of the optical paths. APD signals were sent into photon counting modules and analyzed to form the second-order correlation curves.

The epitaxial structure for the study in this chapter was the same as sample #51C with pitch size of 10-μm. To perform the correlation measurements, the less negatively-charged dots were chosen.

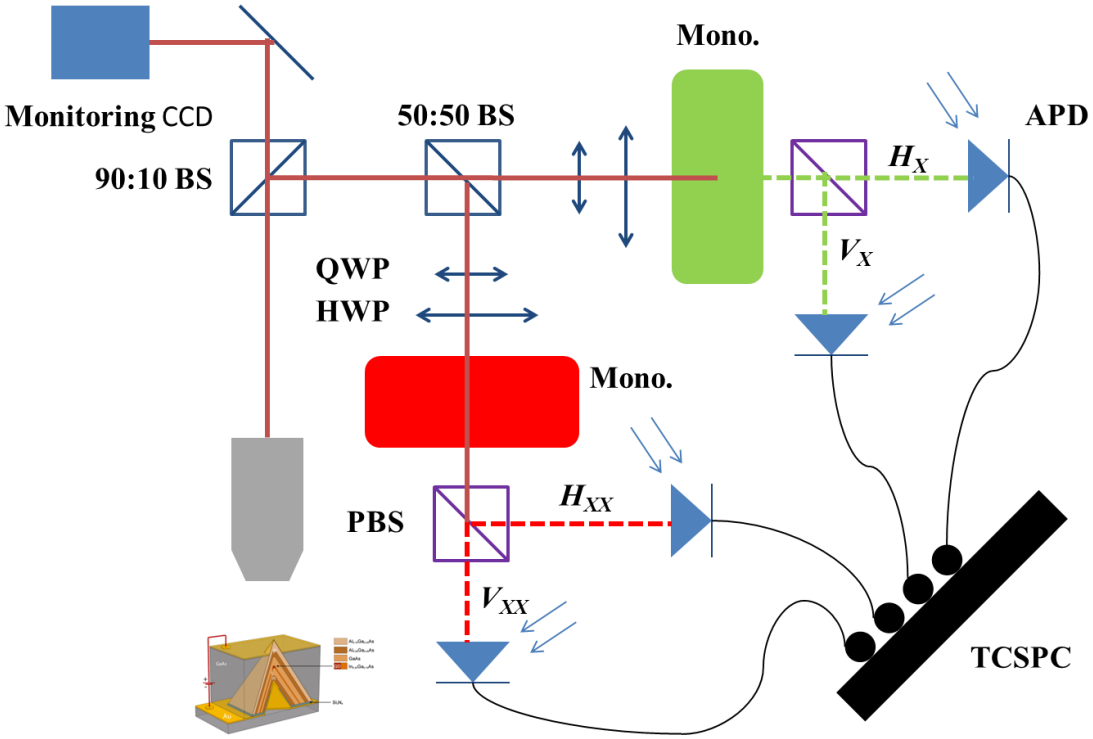

Fig. 6.2: Measurement setup for second-order correlation spectra.

6.3 Distribution of FSS

In Fig. 6.3, a representative electroluminescence (EL) spectrum from a single PQD LED is presented. Three main peaks, corresponding to negative trion (X-), X, and XX can be observed. Even though the X- dominates in intensity, the counts for both X and XX are

still bright enough to preform meaningful correlation measurements for reconstructing entanglement. Polarization-dependent EL measurements were conducted to extract the FSS, which can be seen in the insert of Fig. 6.3. For this very dot, the value of FSS is 0.2±0.2 μeV, which is below both the lifetime limited spontaneous emission exciton linewidth, i.e., a very promising candidate for the realization of polarization-entanglement. For clarity, the distribution of FSS over 94 devices is also shown in Fig. 6.4, showing an average value of 2.9±0.18 μeV.

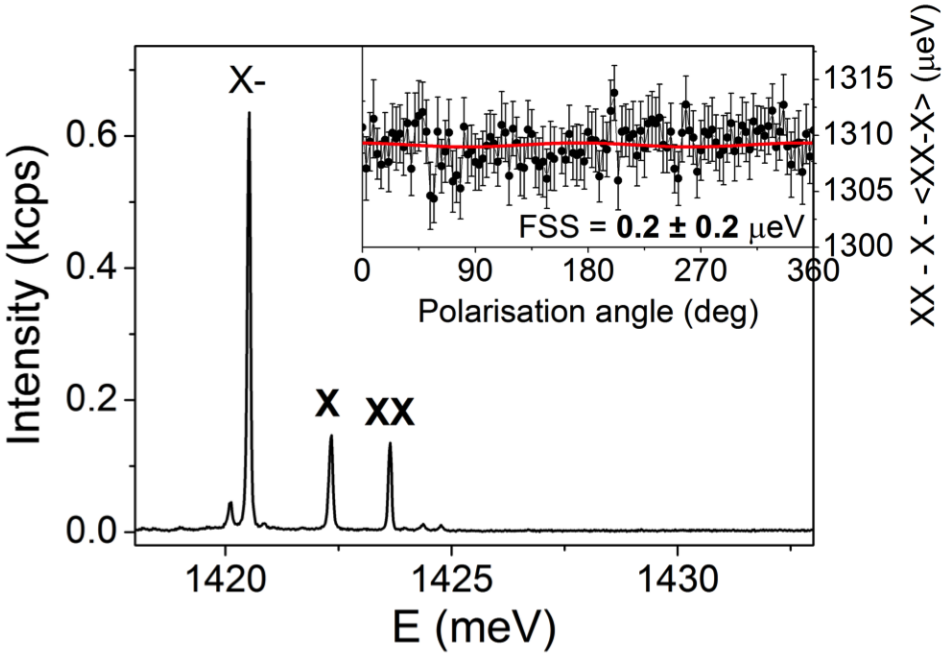

Fig. 6.3: EL spectra from a representative single PQD LED and FSS of 0.2±0.2 eV (inset).

It is worth to mention here that the values of FSS can be related to the QD emitting energy. An observation which was reported for both specifically processed self-assembled QDs (SA-QDs) [14], but also in PQDs even for very different physical reasons [15]. In the mentioned case of SA-QDs, the QD with X transition at 1.4 eV would have close to zero FSS [14]. In our PQD system, based on In0.25Ga0.75As QDs, a window of operation is 1.42 to 1.44 eV [15] see Fig. 6.4. The window can be varied by modifying the thickness of QD layers once the content of indium is fixed. Here, the QD layer thickness is 0.55 nm.

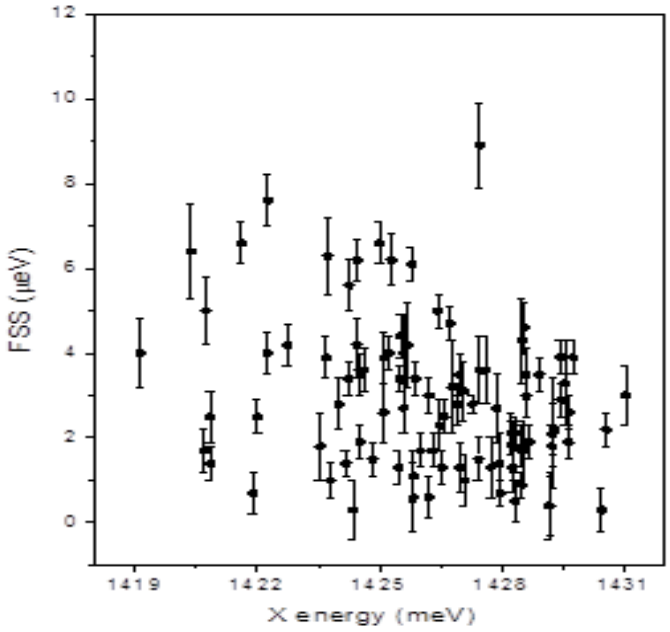

Fig. 6.4: Distribution of FSS over the measured 94 dots. The average value is 2.9±0.18 μeV.

6.4 Intensity correlation functions

From all the studied PQD LEDs, two devices with 0.2 and 0.4 **μ**eV FSS (and without strong background noises coming from adjacent electrically-driven devices) were selected to test polarization entanglement. In Fig. 6.5 (a), six XX-X intensity correlation curves, measured in rectilinear, diagonal, and circular bases from the device with $0.4 \pm \mathbf{0.8}$ **μ**eV FSS obtained with an applied voltage of 8.7 V (DC) with CW current injection are shown. While the results from a device with $0.2 \pm \mathbf{0.2}$ **μ**eV FSS, which was pumped by electric pulses, with a 3 V DC offset (slightly lower than the threshold for observing emissions) combined with pulses with width, 1.4 ns, height, 14 V, and repetition rate, 63 MHz, are presented in Fig. 6.5(b). According to Eq. 6.1 and 6.2, correlations between co-polarized X and XX photons in rectilinear and diagonal, and anti-correlation in circular bases are to be observed around zero delay [2-13], consistent with what is shown in Fig. 6.5.

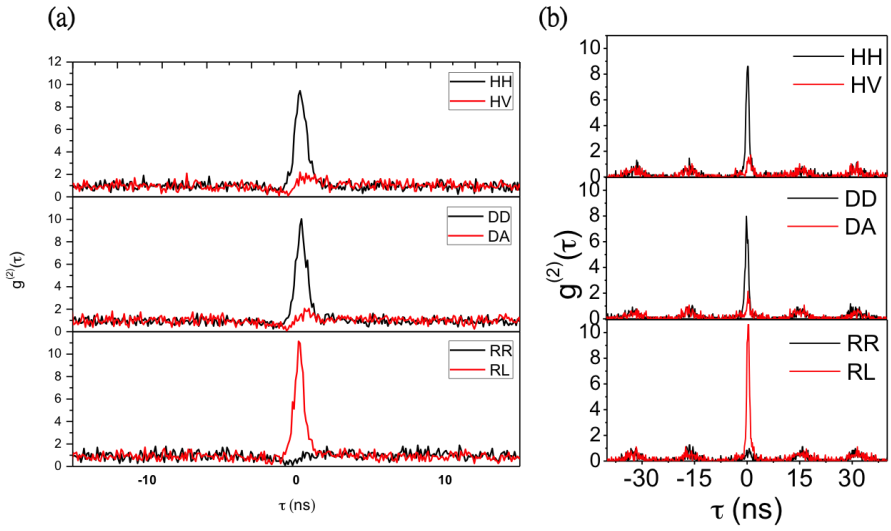

Fig. 6.5: Second-order correlation curves taken in rectilinear, diagonal, and circular bases from the devices pumped (a) by CW voltage and (b) by pulses.

6.5 Fidelity to polarization entanglement

In general, a quantum tomography procedure, which is the process of reconstructing the density matrix **ρ** from a set of 16 intensity measurement, is required to estimate two-photon polarization state [23]. After conducting such a procedure, parameters such as Peres [25], concurrence [23], Tango [24], and so forth, can be derived to judge the purity of entanglement. However, since the expected maximally entangled state is known, the number of measurements can be reduced to the density matrix elements necessary to calculate the fidelity $\mathbf{f} = \langle\boldsymbol{\psi}|\boldsymbol{\rho}|\boldsymbol{\psi}\rangle$ to the entangled state $|\boldsymbol{\psi}\rangle$ and the value of f can be acquired [26]:

$$\boldsymbol{f = (1 + C_R + C_D - C_C)/4}, \tag{6.4}$$

where C_R, C_D, and C_C are degrees of correlation measured in rectilinear, diagonal, and circular bases. These degrees of correlations are defined as:

$$\boldsymbol{C_{basis} = \frac{g^{(2)}_{xx,x} - g^{(2)}_{xx,\bar{x}}}{g^{(2)}_{xx,x} + g^{(2)}_{xx,\bar{x}}}} \tag{6.5}$$

where $\boldsymbol{g}^{(2)}_{xx,x}$ and $\boldsymbol{g}^{(2)}_{xx,\bar{x}}$ are the simultaneously measured, normalized coincidences of the *XX* photon with the co-polarized *X* and orthogonally polarized *X* photons respectively. Hence the f value ranges from 0 to 1 with one being the perfect entangled state value, and 0.5 the lowest value for being considered "non-classical" for a given system. This approach is broadly accepted as an accurate simplified methodology and is used across the "QD entanglement" community [2-13].

The fidelity for the device shown in Fig. 6.5(a) was conducted by selecting correlation events about zero time delay from a time window of 0.5 ns, designed to collect ~ "all" correlation events. The value of fidelity is $\mathbf{0.73 \pm 0.06}$ (> 0.5), i.e. is qualified as an entangled light source. Since the entangled light sources are valuable specifically for the capability of being triggered on demand, more attention will here be paid on the performance as a device pumped by pulse mode. Indeed, the calculated fidelity from the device discussed in Fig. 6.5 (b) is $\mathbf{0.678 \pm 0.023}$, i.e. over 7 standard deviations from the non-classical lower limit.

Even though the FSS of the studied device is close to zero, such small value still causes a substantial deterioration of entanglement. Among many other possible issues, two between of them are especially pronounced and intuitive: (1) the finite pulse-width of the driving current (1.4 ns), which is broad enough to cause repopulation of a QD; (2) background noise from emissions of QDs nearby. These effects can be alleviated by a post-measurement time-gating techniques [10,30]. Instead of collecting the events in the whole time window, only events within a specific narrower time window are considered. This selecting mechanism effectively boosts the fidelity, as observed in Fig. 6.6, where fidelities increase along with the reduced gate widths. Nevertheless the price of applying such technique is to discard detection events. However, in this device, the fidelity can be tuned up to $\mathbf{0.823 \pm 0.019}$ by selecting a 1.5 ns gate window while retaining 75 % of the detection events were preserved, indicating a promising potential for such entangled-light sources.

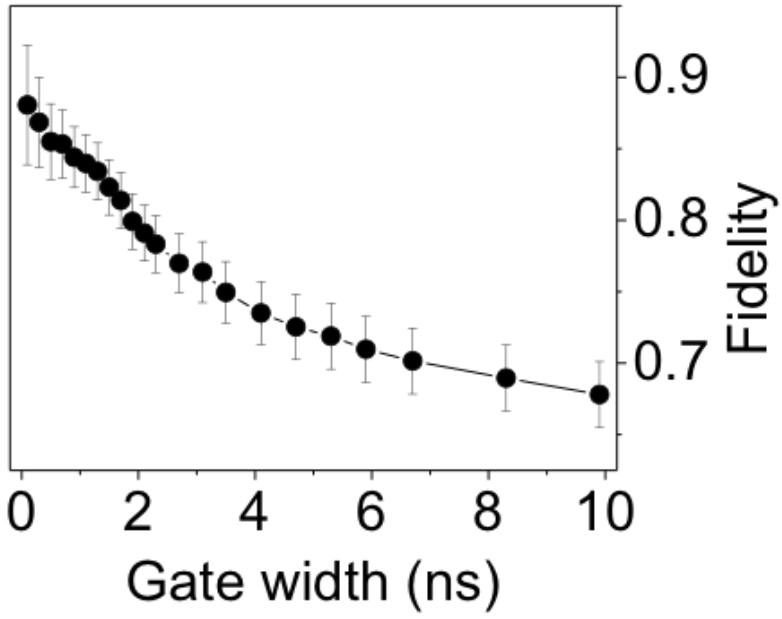

Fig. 6.6: Fidelities resulted from various time gate widths.

In Fig. 6.7, the statistical results of all the reported fidelities to polarization-entanglements, based on SA-QDs, [2-8,10-12] PQDs [5,13], and nanowire QDs [9] are listed, with the red dot-lines marking the electrically-driven devices, while the black dot-lines show the results from optical pumping. After the first optically-driven polarization sources were demonstrated [2,3], there were subsequently many groups which continued to improve their "source" quality either by shifting the excitation energies from non-resonant to resonant pumping [7], or by raising up the light extraction efficiency through the combination with double micro-cavities [8], or by changing the crystal orientation of growth substrate to [111]A [4]. As for the works on electrical pumping, before our study, there are only two groups reporting the convincing data so far [10-12], however without site-control.

From the comparison, the performance of our device is competitive to previous reports. Moreover this also strongly indicates that, based on PQD LEDs, polarization-entanglement sources can be delivered, satisfying both position-controlled and electrically-triggering on demand, without degradation of entanglement.

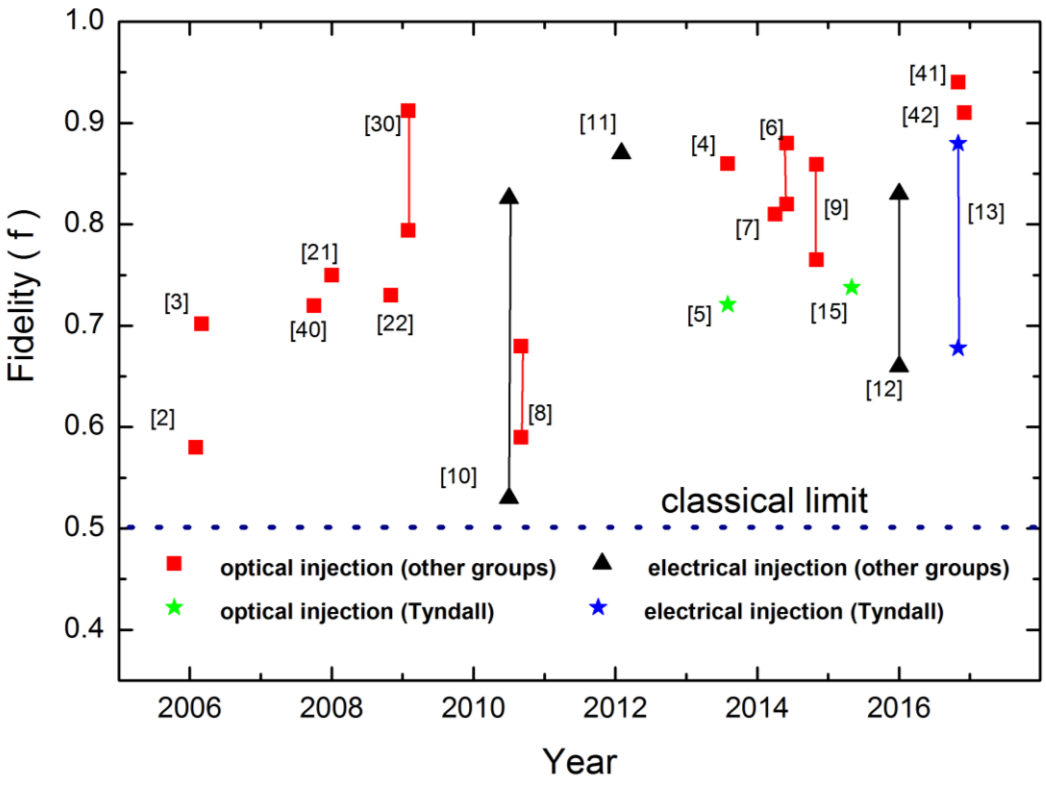

Fig. 6.7: Fidelities to polarization-entanglement reported to date. The line represents the range of fidelities changed along with gate widths.

6.6 Violation of Bell's inequality

In 1964, John S. Bell [28] analyzed critically the objection posted by Einstein, Podolsky, and Rosen of the completeness of quantum mechanics (QM) [27]. He derived an inequality that any classically correlated event needs to fulfill. He showed that quantum systems do not respect such equation, i.e. they violate Bell's inequality. By showing this he proved that quantum correlations within an entangled system cannot be described by any classical "local" mechanics (i.e. the correlation is not predetermined at the source). This has been verified experimentally in various entangled systems and remains a topic of intense research [36-38]. For a detail report regarding the fundamental role of Bell's theorem in QM, we encourage the reader to a recent review [39]. To be noted, one can construct a number of equivalent Bell's inequalities, and that experimentally it is more convenient to rely on what is normally known as CHSH form, named after the authors J. F. Clauser, M.A. Horne, A. Shimony, and R. A. Holt [29].

In this thesis, however, we will simply use the violation of Bell's inequality (VBI) with a specific purpose, i.e. as a stringent test for entanglement. Taking polarization-entanglement as an example, not only non-classical correlations, but also high fidelity to the maximally entangled state is needed to achieve VBI [30], which can be viewed as a crucial threshold for many practical applications in quantum communication; see for example [35].

According to previous works [10,12,29,30], some of the "traditional" CHSH inequalities can be expressed as:

$$\boldsymbol{S_{RD} = \sqrt{2}(C_R + C_D) \leq 2}, \tag{6.5}$$

$$\boldsymbol{S_{DC} = \sqrt{2}(C_D - C_C) \leq 2}, \tag{6.6}$$

$$\boldsymbol{S_{RC} = \sqrt{2}(C_R - C_C) \leq 2}, \tag{6.7}$$

where S_{RD}, S_{DC}, and S_{RC} are three Bell's parameters, effectively corresponding to different measurements in orthogonal planes intersecting the Poincare sphere.

According to an estimation in [30], an upper limit for the FSS within XX-X-G decay cascade is <0.5 μeV to demonstrate VBI. Hence the device with 0.2±0.2 μeV was tested, and the calculated Bell's parameters along with various gate widths are depicted in Fig. 6.8. As the selected window was 1.5 ns, the measured Bell's parameters were, $\boldsymbol{S_{RD} = 2.053 \pm 0.07, S_{DC} = 2.191 \pm 0.075}$, and $\boldsymbol{S_{RC} = 2.239 \pm 0.074}$, achieving VBI.

In conclusion we showed that our PQD devices, not only provide high fidelity entanglement, but also violate Bell's inequalities. An achievement which is unique for site-controlled QDs, and there are few comparable results in the QD community.

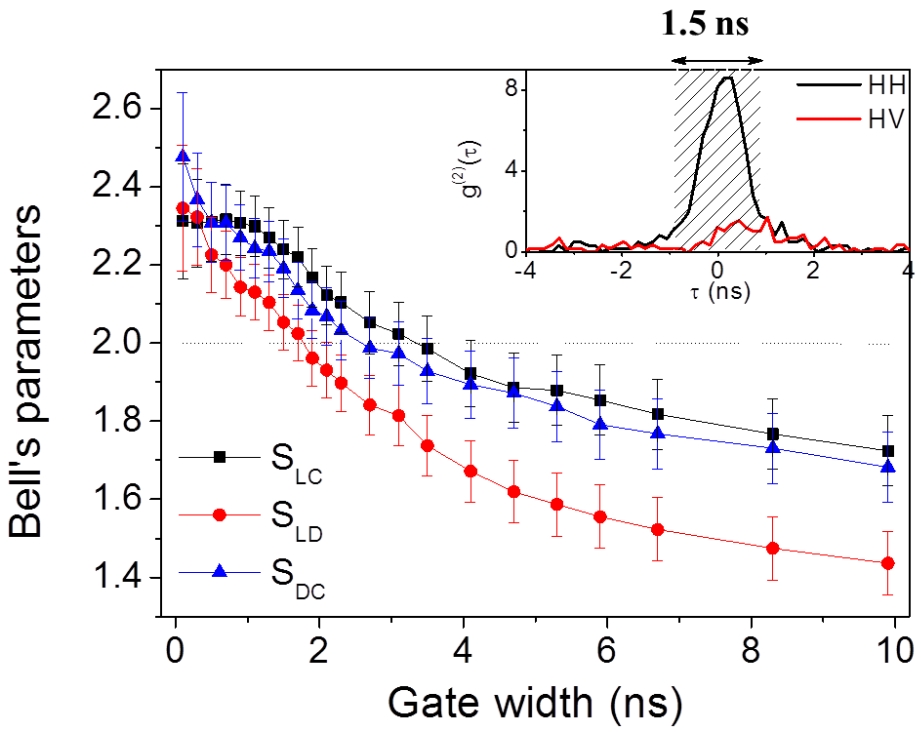

Fig. 6.8: Three Bell's parameters along with different gate widths.

6.7 Summary

In this chapter, electrically-driven polarization-entangled photon sources have been successfully demonstrated for the first time among all site-controlled quantum dot systems. The fidelities to the entanglement were 0.85±0.01 under continuous excitation and 0.823±0.019 under pulse excitation with 75 % photon intensity maintained by 1.5 ns time-gating window. Moreover, pure entanglement has been proven by the violation of Bell's inequalities.

Bibliography

[1]: O. Benson, C. Santori, M. Pelton, and Y. Yamamoto, Phys. Rev. Lett., 84 (2000) 2513.

[2]: R. M. Stevenson, R. J. Young, P. Atkinson, K. Cooper, D. A. Ritchie, and A. J. Shields, Nature, 439 (2006) 179.

[3]: R. J. Young, R. M. Stevenson, P. Atkinson, K. Cooper, D. A. Ritchie, and A. J. Shields, New J. Phys., 8 (2006) 29.

[4]: T. Kuroda, T. Mano, N. Ha, H. Nakajima, H. Kumano, B. Urbaszek, M. Jo, M. Abbarchi, Y. Sakuma, K. Sakoda, I. Suemune, X. Marie, and T. Amand, Phys. Rev. B, 88 (2013) 041306 (R).

[5]: G. Juska, V. Dimastrodonato, L. O. Mereni, A. Gocalinska, and E. Pelucchi, Nat. Photon., 7 (2013) 527.

[6]: R. Trotta, J. S. Wildmann, E. Zallo, O. G. Schmidt, and A. Rastelli, Nano Lett., 14 (2014) 3439.

[7]: M. Müller, S. Bounouar, K. D. Jöns, M. Glässl, and P. Michler, Nat. Photon., 8 (2014) 224.

[8]: A. Dousse, J. Suffczyński, A. Beveratos, O. Krebs, A. Lemaître , I. Sagnes, J. Bloch , P. Voisin, and P. Senellart, Nature 466 (2010) 217.

[9]: M. A. M. Versteegh, M. E. Reimer, K. D. Jöns, D. Dalacu, P. J. Poole, A. Gulinatti, A. Giudice, and V. Zwiller, Nat. Comm., 5 (2014) 5298.

[10]: C. L. Salter, R. M. Stevenson, I. Farrer, C. A. Nicoll, D. A. Ritchie, and A. J. Shields, Nature, 465 (2010) 594.

[11]: R. M. Stevenson, C. L. Salter, J. Nilsson, A. J. Bennett, M. B. Ward, I. Farrer, D. A. Ritchie, and A. J. Shields, Phys. Rev. Lett., 108 (2012) 040503.

[12]: J. Zhang, J. S. Wildmann, F. Ding, R. Trotta, Y. Huo, E. Zallo, D. Huber, A. Rastelli, and O. G. Schmidt, Nat. Comm., 6 (2015) 10067.

[13]: T. H. Chung, G. Juska, S. T. Moroni, A. Pescaglini, A. Gocalinska, and E. Pelucchi, Nat. Photon., Nat. Photon., 10 (2016) 782.

[14]: R. J. Young, R. M. Stevenson, A. J. Shields, P. Atkinson, K. Cooper, D. A. Ritchie, K. M. Groom, A. I. Tartakovskii, and M. S. Skolnick, Phys. Rev. B, 72 (2005) 113305.

[15]: G. Juska, E. Murray V. Dimastrodonato, T-H Chung, S. T. Moroni, A. Gocalinska, and E. Pelucchi, J. Appl. Phys., 117 (2015) 134302.

[16]: R. M. Stevenson, R. J. Young, P. See, D. G. Gevaux, K. Cooper, P. Atkinson, I. Farrer, D. A. Ritchie, and A. J. Shields, Phys. Rev. B, 73 (2006) 033306.

[17]: M. Ghali, K. Ohtani, Y. Ohno, and H. Ohno, Nat. Comm., 3 (2012) 661.

[18]: R. Trotta, E. Zallo, C. Ortix, P. Atkinson, J. D. Plumhof, J. van den Brink, A. Rastelli, and O. G. Schmidt, Phys. Rev. Lett., 109 (2012) 147401.

[19]: R. Trotta, J. Martín-Sánchez, I. Daruka, C. Ortix, and A. Rastelli, Phys. Rev. Lett., 114 (2015) 150502.

[20]: A. I. Tartakovskii, M. N. Makhonin, I. R. Sellers, J. Cahill, A. D. Andreev, D. M. Whittaker, J-P. R. Wells, A. M. Fox, D. J. Mowbray, M. S. Skolnick, K. M. Groom, M. J. Steer, H. Y. Liu, and M. Hopkinson, Phys. Rev. B, 70 (2004) 193303.

[21]: A. J. Hudson, R. M. Stevenson, A. J. Bennett, R. J. Young, C. A. Nicoll, P. Atkinson, K. Cooper, D. A. Ritchie, and A. J. Shields, Phys. Rev. Lett., 99 (2007) 266802.

[22]: R. M. Stevenson, A. J. Hudson, A. J. Bennett, R. J. Young, C. A. Nicoll, D. A. Ritchie, and A. J. Shields, Phys. Rev. Lett., 101 (2008) 170501.

[23]: D. F. V. James, P. G. Kwiat, W. J. Munro, and A. G. White, Phys. Rev. A, 64 (2001) 052312.

[24]: V. Coffman, J. Kundu, and W. K. Wootters, Phys. Rev. A, 61 (2000) 052306.

[25]: A. Peres, Phys. Rev. Lett., 77 (1996) 1413.

[26]: A. J. Hudson, Ph.D. thesis, University of Cambridge, 2008, P. 101.

[27]: A. Einstein, B. Podolsky, and N. Rosen, Phys. Rev., 47 (1935) 777.

[28]: J. S. Bell, Physics (Long Island City, N.Y.), 1 (1965) 195.

[29]: J. F. Clauser, M.A. Horne, A. Shimony, and R. A. Holt, Phys. Rev. Lett., 23 (1969) 880.

[30]: R. J. Young, R. M. Stevenson, A. J. Hudson, C. A. Nicoll, D. A. Ritchie, and A. J. Shields, Phys. Rev. Lett., 102 (2009) 030406.

[31]: T. Flissikowski, A. Hundt, M. Lowisch, M. Rabe, and F. Henneberger, Phys. Rev. Lett., 86 (2001) 3172.

[32]: C. Santori, D. Fattal, M. Pelton, G. S. Solomon, and Y. Yamamoto, Phys. Rev. B, 66 (2002) 045308.

[33]: B. D. Gerardot, S. Seidl, P. A. Dalgarno, R. J. Warburton, D. Granados, J. M. Garcia, K. Kowalik, O. Krebs, K. Karrai, A. Badolato, and P. M. Petroff, Appl. Phys. Lett., 90 (2007) 041101.

[34]: K. F. Karlsson, M. A. Dupertuis, D. Y. Oberli, E. Pelucchi, A. Rudra, P. O. Holtz, and E. Kapon, Phys. Rev. B, 81 (2010) 161307(R).

[35]: A. K. Ekert, Phys. Rev. Lett., 65 (1991) 661.

[36]: M. A. Rowe, D. Kielpinski, V. Meyer, C. A. Sackett, W. M. Itano, C. Monroe, and D. J. Wineland, Nature, 409 (2001) 791.

[37]: M. Ansmann, H. Wang, R. C. Bialczak, M. Hofheinz, E. Lucero, M. Neeley, A. D. O'Connell1, D. Sank, M. Weides, J. Wenner, A. N. Cleland, and J. M. Martinis, Nature, 461 (2009) 504.

[38]: A. Aspect, P. Grangier, and G. Roger, Phys. Rev. Lett., 49 (1982) 91.

[39]: N. Brunner, D. Cavalcanti, S. Pironio, V. Scarani, and S. Wehner, Rev. Mod. Phys., 86 (2014) 839.

[40]: R Hafenbrak, S M Ulrich, P Michler, L Wang, A Rastelli, and O G Schmidt, New J. Phys., 9 (2007) 315.

[41]: D. Huber, M. Reindl, Y. Huo, H. Huang, J. S. Wildmann, O. G. Schmidt, A. Rastelli, and R. Trotta, arXiv:1610.06889v1 (2016).

[42]: R. Keil, M. Zopf, Y. Chen, B. Hoefer, J. Zhang, F. Ding, and O. G. Schmidt, arXiv:1611.03717v1 (2016).

Chapter 7

Conclusions and future directions

7.1 Conclusions

The main motivation for this thesis was to develop a reproducible fabrication process for making light-emitting diodes with pyramidal quantum dots (PQDs). This is to deliver a quantum light source for single-photons and polarization-entangled photon pairs with control on spatial positioning and with trigger on demand at the same time. As detailed in our text, a number of challenges, mainly coming from an inherent three-dimensional configuration, were overcome, and the electrically driven quantum light sources were demonstrated showing high quality. Our results are competitive with those obtained from conventional epitaxial semiconductor quantum dot systems with randomly-distributed features.

For the single-photon source, we have successfully established an electrically pumped device with trigger on demand for the very first time with a PQD decisively verified by second-order correlation spectra under pulsed mode excitation. The clear anti-bunching behavior was shown from a measurement on a representative negative trion, indicating a vanishing probability of multiphoton process. Combining with a post-measurement time-gating technique, a very small value of $g^{(2)}(0) = 0.078 \pm 0.066$ was obtained.

In terms of polarization-entangled photon pairs, the generation by electrically pumping was demonstrated for the first time considering any site-controlled system reported so far. It resulted from a strongly reduced fine-structure splitting (FSS, ~ 0.2±0.2 μeV) thanks to an inherent higher C_{3V} crystal symmetry. Record high fidelities to the expected Bell's state were achieved (0.85±0.04) under continuous mode excitation, paralleled with 0.823±0.019 under pulsed mode excitation with a time gating widow of 1.5 ns, in which 75 % of the original intensity was preserved. Moreover, such entangled optical

states were able to achieve the violation of Bell's inequality, which is a more rigorous threshold qualifying an entangled light source for quantum protocols.

We also analyzed growth mechanisms and a growth model, based on stationary solutions of a series of reaction-diffusion equations among different facets This result was utilized to simulate the true indium content and self-limiting base widths at the center of pyramidal recesses in the QD structure. The positive correlation found between In contents and base widths as a function of growth temperatures in the model (during growth inside pyramidal recesses) justify the redshift observed in the emission energies from PQDs with increasing growth temperatures as reported in previous experiments (G. Juska et al., J. Appl. Lett., 117, 134302, 2015). In addition, abrupt faceting at the bottom of pyramidal recesses were also revealed for the first time.

We also worked on details in the PDQ structure to improve our sources. Trials to suppress the intensity of trions, which mainly dominate in negative form and are detrimental to the biexciton-exciton correlation cascade, have been conducted by the introduction of an AlAs etchstop layer, a non-coupled sacrificial QD layer, and a dual-laser excitation scheme. With addition of an AlAs layer as first layer in the etchstop region, which were previously mainly composed of $Al_{0.45\sim0.8}Ga_{0.55\sim0.2}As$ and $Al_{0.8}Ga_{0.2}As$, the dominant excitonic transition changed, statistically i.e. in most pyramidal structures, from negative trions to neutral excitons after the sample back-etching. This indicates a contribution from excess electrons possibly originating from the etched surface. Another strategy for improvement employed additional QD layers as "*absorbers*" of excess carriers, leading to an improvement in optical properties of the last-grown QD layer, such as narrower linewidth and again more neutral excitons presence. From the measurement technique side, a secondary pump laser of ~ 1180 meV, was introduced and trialed to activate transitions from valence band to GaAs deep levels, so as to obtain excess holes which would change the excitonic charging type in the QDs. Therefore the deteriorated (by negative trions) biexciton decay cascade could also be restored for the polarization-entanglement in the case of PQDs with close-to-zero FSS. These techniques all showed good success depending on the specific dot and dot structures in which they were trialed.

7.2 Future works

A number of issues for the optimization of our structures remain.

Reduction of turn-on voltage: In general, the turn-on voltages and operation conditions of conventional GaAs-based p-i-n LED are smaller than 2 V, i.e. far smaller than our case: more than 8 V in DC mode and 14 V pulse with a 3 V DC offset in AC mode. Since sources of electrical pulses with such high voltage and still with narrow pulse width (sub-nanosecond) are not easily available at present, the narrowest pulse width, 1.4 ns, used for this thesis raises up the probability of double excitation during a single pulse. In this scenario, multiphoton process cannot be avoided from pulse mode operation, reflected in the finite $g^{(2)}(0)$ value of the second-order auto-correlation spectra measured for single-photon sources as well as the reduced fidelities to the canonical polarization entangled state. Two possible solutions are proposed: first, creating a better interface between contact metal and p-doped GaAs by means of hydrofluoric (HF) acid or buffered HF removing all p-doped AlGaAs layers fully; second, employment of alloy-graded $Al_{0.75}Ga_{0.25}As$ layers located at n-i and p-i interfaces to reduce the suppression of current flow induced by large band offsets.

Tuning of FSS: Even though the values of FSS from the studied PQDs are relatively small (2.9±1.8 μeV), it is necessary to have an additional knob to further control the FSS value "individually" to retrieve polarization entanglement of all emitters at wafer scale. Among all the candidates, the employment of piezoelectric actuator is very promising since it also empowers electrical injection. Well-developed both in theory and experiments this approach, as combination of Stranski-Krastanov mode QDs and piezoelectric materials, can be referred to R. Trotta et al. (Nat. Commun., 7, 10375, 2016 and Phys. Rev. Lett., 114, 150502, 2015). Considering our current fabrication process, the only difference required is to bond a PQD sample on six-legged piezoelectric actuator instead of a supportive GaAs substrate. Hence it is highly compatible to our fabrication routine, and a collaboration with Prof. A. Rastelli in University Linz is ongoing and promising.

Increment of light extraction rate: In quantum communication, high light extraction rates of either single-photons or entangled photon pairs are desirable, since they will

directly affect how much information can be carried for example. Even though our scheme of light collection in changing from apex-down to apex-up has increased the extracted light intensity of ~ three orders of magnitude, so far, counts for our quantum light-emitting diodes in our system are tens of thousands per second for single-photon emission and around 1000 "good" pairs per hour for entangled photon pairs. Considering our device configuration, a most suitable method for increasing light extraction could be to combine PQDs with hemisphere micro-lenses. This idea is inspired by e.g. M. Gschrey et al. (Nat. Commun., 6, 7662, 2015), which exploited a concentric dose-dependent electron-beam lithography and selective dry etching between dome-like photoresist and GaAs. The basic concept is to mechanically thin down the original substrate to ~20 μm, and align pyramids with an array of circular patterns, using the firstly appearing pyramids due to inhomogeneous etching as alignment markers. Since cylinder-like mesas will turn to dome-like shape if the right hard backing temperature is applied, the so-called photoresist reflow, dome-like GaAs micro-lenses upon apex-up pyramids can be realized by final inductively coupled-plasma reactive-ion etching. Thus the portion of dissipated light, due to refraction, can be reduced, leading to a reasonable anticipation of increasing light extraction.

Resonant pumping: Obviously these are short term solutions to improve our sources. On the other hand, for fully empowered quantum computation tasks nearly 100% fidelities are needed, and so indistinguishable photons in general. Future work will have to deal with addressing these issues, which will also involve developing new excitation schemes such as a two-photon resonant pumping for example (M. Müller et al., Nat. Photon. 8, 224, 2014).